SAPIENZA
UNIVERSITÀ DI ROMA

DIPARTIMENTO DI
INGEGNERIA DELL'INFORMAZIONE
ELETTRONICA E TELECOMUNICAZIONI

THz band communications: next frontier for impulse radio Ultra Wide Band

By

Alireza Mohammadpour

A thesis submitted
in partial fulfillment of the requirements for the degree of
Doctor of Philosophy in Information and Communication Engineering

Sapienza University of Rome

Department of Information Engineering, Electronics and Telecommunications

Supervisor

Prof. Maria-Gabriella Di Benedetto

January 2021
XXXIII

Thesis defended on "Defence Date"
in front of a Board of Examiners composed by:

Prof. Nome Cognome (chairman)

Prof. Nome Cognome

Dr. Nome Cognome

THz band communications: next frontier for impulse radio Ultra Wide Band
Ph.D. thesis. Sapienza – University of Rome
ISBN: 000000000-0

This thesis has been typeset by LaTeX and the Sapthesis class.

Version: March 1, 2021

Author's email: Alireza.mohammadpour@uniroma1.it

Contents

List of Tables

List of Figures

Chapter 1

Introduction

In recent years the demand for high data rate transmission is growing for indoor wireless communication systems. One of the most promising candidates that can fulfill the necessity for higher data rates in wireless communications is the TeraHertz (THz) band (0.1-10 THz). However, THz frequencies have peculiar propagation characteristics such as high free space loss, high molecular absorption, and high diffuse scattering attenuation. Therefore, it is necessary to consider all possible sources of attenuation and distortion in order to propose a propagation model for the THz range of frequencies.
Presently, there exist numerous statistically based channel models, which are generally considered adequate for outdoor environment planning. For indoor wireless services, though, these statistically based models do not provide sufficient information because of the complexities and variations of the propagation environments, which are usually rich in reflections and scattering.
A feasible propagation model, based on geometrical ray tracing, can be used to predict details about an indoor environment with known parameters such as geometry and building materials. A suitable model for almost any indoor situation can be generated by adjusting these specific parameters. Moreover, the model needs to be sufficiently general to accommodate signal properties such as polarization and channel parameters such as geometry, dielectric constants of the surfaces, and the like. This research proposes a multipath channel model to predict the propagation of wireless signals in indoor environments more accurately. Although a plethora of works has been done on different aspects of THz channel modeling, a detailed tutorial from the physical nature to the implementation of THz channel modeling has been missed so far to the best of the author's knowledge. The aim of this work is to give a well description of different type of attenuation at THz frequencies and explore the fundamental concepts behind developing a unified channel model which accurately characterizes the Terahertz spectrum peculiarities. Besides, a self-implemented ray tracer is also proposed to analyze the THz range channel model, taking into account the impact of most characterizing factors, including free-space path loss, molecular absorption, and scattering. Numerical results will be verified along with the theory and measurements.

In this thesis, an introduction to THz characteristics such as free space attenuation, molecular attenuation, and diffuse scattering is given in Chapter 2, along with a complete picture of diffuse scattering and Kirchhoff theory, which will be covered later in the study.
Chapter 3 presents the statistical description of the most commonly used surfaces in indoor environments. Also, we discuss different methods for generating randomly rough surfaces often used in indoor environments. Then a multi ray propagation model is proposed, which includes THz band characteristics.
In chapter 4, a homemade ray-tracing simulator is proposed. This chapter covers a description of the image-based ray tracing method besides a full description of the indoor environment, including obstacles. Moreover, the way of applying the Kirchhoff theory in the ray-tracing simulator is introduced. To model the THz channel model, the surface profile, which is generally unknown, is required first. Thus the generation of a random surface model followed by a description of computing scattered power from the generated random rough surface is presented.
In chapter 5, the results obtained by using the proposed ray-tracing tool are presented. The results focus on comparing the measured reflection coefficient in the specular direction and the theory, showing the impact of specific parameters affecting the received power, and discussing the power delay profile and the frequency-dependent channel impulse response (CIR) at each center frequency.
Finally, in chapter 6, we provide a summary of the research and some conclusions. We also provide possible directions for future work in this research area.

Chapter 2

TeraHertz communications

2.1 TeraHertz waves characterization

A remarkable increase in the use of mobile devices and wireless networks has been witnessed in recent years. A research carried out by the Japanese government on an estimation of the annual growth rate of mobile traffic in Japan [5], shows a 71% of the annual growth rate of mobile traffic from 2007 to 2017. Thus, there is a necessity to increase the capacity of wireless networks. Solutions were proposed to increase channel capacities such as advanced modulation methods and increased operating frequencies such as TeraHertz (THz) frequencies. TeraHertz communications are an attractive solution because of the availability of frequency band and communication bandwidth since frequencies above 300 GHz are unallocated by the Federal Communication Committee(FCC). Figure 2.1 [6] shows wireless spectrum used by the commercial systems in the USA. Each row represents a decade in frequency, and it can be seen that frequencies over 300 GHz are unallocated by FCC. Figure 2.1 shows the frequency allocation from 30 kHz to 300 GHz by the FCC in the USA. Other countries have very similar frequency allocations. Figure 2.1 shows that as well known lower frequencies are already allocated to many different uses such as AM Radio and TV broadcasting. Current cellphone and wireless devices operate at carrier frequencies between 700 MHz and 6 GHz. The mmWave frequencies are in the range between 30 to 300 GHz and are used by military, radar, and backhaul, but utilization the much lower. As a matter of fact, most countries have not allocated frequencies above 100 GHz [6]. It is worth mentioning that the unallocated frequencies around 60 GHz provide a more available spectrum than what is used by altogether the satellite, cellular, WIFi, AM Radio, FM radio, and TV stations in the world. At 300 GHz, there is even more available bandwidth than at 60 GHz. THz communications are in the earlier stage of development and provide, therefore, a lot of room for future development.

Frequency range between 100 GHz and 10 THz, i.e., wavelengths between 3 mm and $3\mu m$, is considered as "TeraHertz frequencies" that is also known as far-infrared or sub-millimeter waves, due to the fact that part of this range

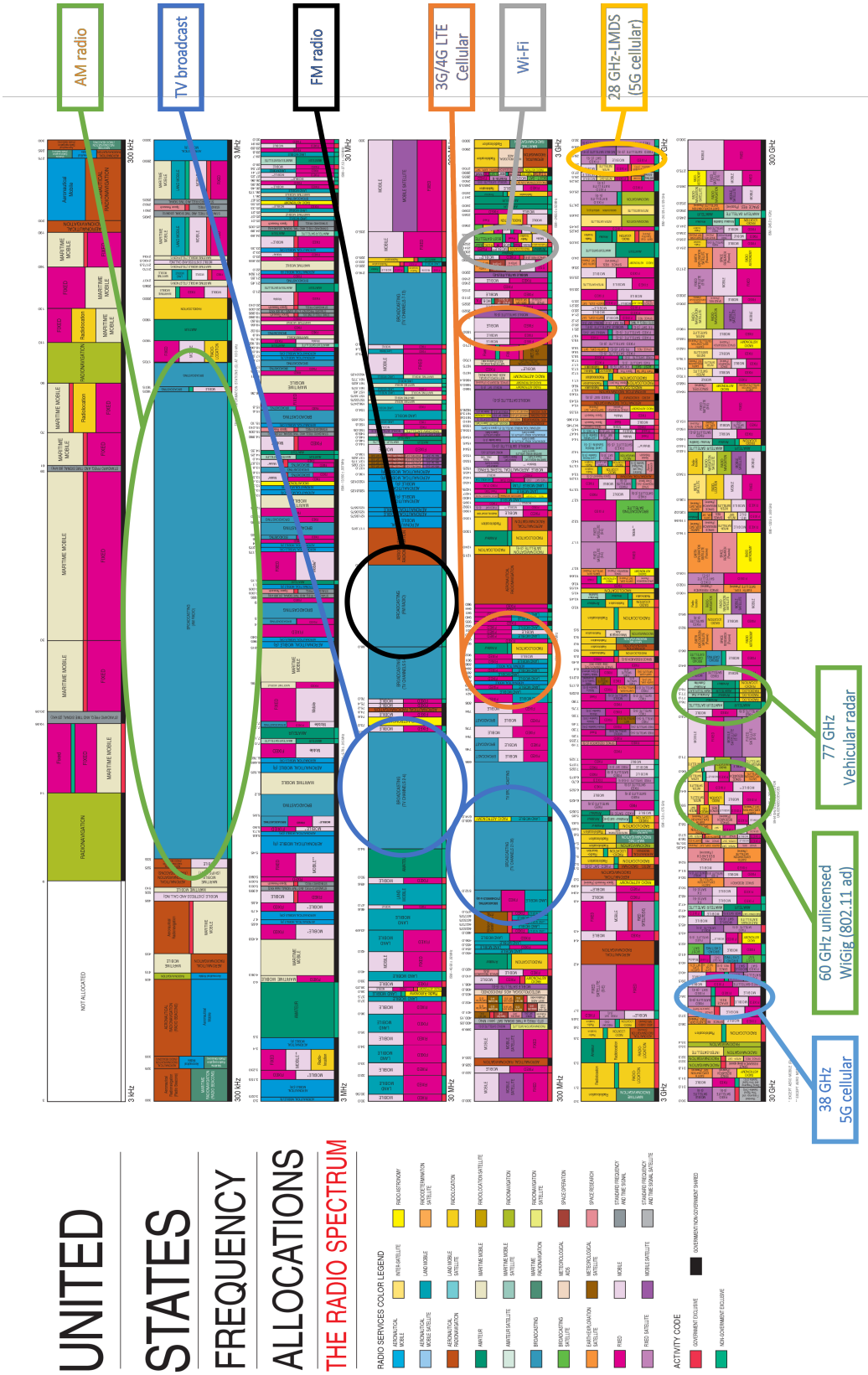

Figure 2.1. Frequency allocations in the USA by the FCC for commercial allocations.

includes the far-IR range and also part of this range includes the millimeter range (see Fig. 2.2). TeraHertz frequencies have peculiar characteristics, such

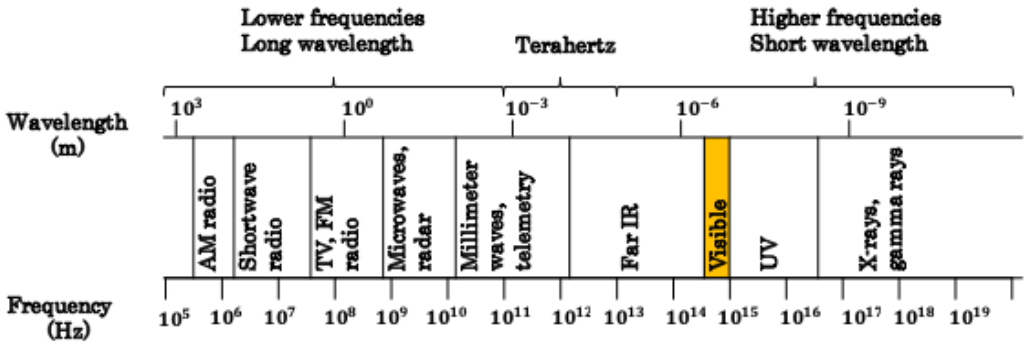

Figure 2.2. Frequency and wavelength regions of the electromagnetic spectrum.

as high free space loss, high molecular absorption, mainly due to water vapor molecules [7], and high diffuse scattering attenuation. Regarding these characteristics, there are several kinds of research on analyzing the atmosphere absorption [8], scattering of building materials [9, 4, 2, 10], link budget[11], body nanonetworks [12], MIMO [13], and so forth [14, 15].
This chapter is organized as follows. Section 2.1 served as an introduction to THz characteristics and provided a general view of THz waves. Section 2.2 focuses on the characteristics of wireless propagation at THz operating frequencies. This section covers several propagation properties at THz range, such as free space attenuation 2.2.1, molecular attenuation 2.2.2, and diffuse scattering 2.2.3 followed by a complete picture of diffuse scattering and Kirchhoff theory 2.2.4, 2.2.5. Note that Kirchhoff theory is used to describe the reflection of the electromagnetic plane waves from smooth and rough surfaces.

2.2 Propagation properties

TeraHertz frequencies have peculiar propagation characteristics such as high free space loss, high molecular absorption, mainly due to water vapor molecules [7], and high diffuse scattering attenuation. Moreover, due to the presence of obstacles or multiple signal reflections, waves are also affected by the material characterizing the surfaces they interact with. In particular, the interaction with rough surfaces gives rise to diffuse scattering. As a matter of fact, the definition of the roughness of a surface is not only related to the morphology of the considered surface, but it also depends on the frequency. The surface roughness increases with the frequency of the incoming waves. Thus, surfaces that can be considered smooth at lower frequencies cease to be so at THz frequencies, making diffuse scattering an important characterizing factor for THz wave propagation. This section will address the above typical phenomena.

2.2.1 Free space attenuation

An EM wave that travels between a transmitter (TX) and a receiver (RX) is typically affected by the free space attenuation, as described by Friis [16]. In other words, when the EM wave is propagating, the area of the transmitted power will increase by the rate of square of the distance between two points, but at the receiver, the area is fixed so, the received power at the receiver will decrease by the factor of quadratic distance and usually is described in dB. The free space path loss A_{FS} that is the attenuation experienced by the transmitted power is given by the well-known Friis equation, i.e.:

$$A_{FS} = \frac{(4\pi d)^2}{\lambda^2 G_T G_R}, \tag{2.1}$$

where λ is the wavelength, d is the distance between the Tx and Rx, and G_T, G_R denote the gains of the antenna at TX and RX, respectively. Note that d and λ have the same unit, while G_T and G_R are adimensional. At THz frequencies, free space attenuation can be relatively high due to quadratic increase with the frequency; Consider, for example a typical indoor environment, such as office space of 4 m $\times$ 4 m $\times$ 3 m, and a 4 m distance between TX and RX, then, for isotropic antennas, one would have $A_{FS} = 84.48$ [dB] at 100 GHz, and $A_{FS} = 104.48$ [dB] at 1 THz: for a distance of just 4 meters!. Figure 2.3 shows the dependence of free space path loss to the frequency, i.e., higher frequencies higher A_{FS}, and also shows the quadratic impact of distance d on A_{FS} in dB. By increasing traveling distance from 2 meters to 8 meters, one faces with higher A_{FS}.

2.2.2 Atmosphere attenuation (Molecular absorption)

When an EM wave is traveling in a medium, the molecules are excited by the EM waves at specific frequencies within the THz band, which leads to internal vibrations of molecules. This vibration is because of converting the energy of propagating wave into the kinetic energy, which in the field of communication is named as lost [7]. Several studies are done to collect the required [17, 18, 19] parameters to characterize the different resonance for different molecules, and these databases are based on real measurements. It is worth mentioning that for the THz frequencies or the frequencies between 0.1 to 10 THz, all the required data to compute the attenuation due to molecular absorption can be found in these databases. Therefore, computing molecular absorption in a given medium relies on HIgh-resolution TRANsmission (HITRAN) molecular absorption line catalog or database [7].
The information provided by the HITRAN databases is used to compute the experienced attenuation of a wave traveling distances up to a few meters due to molecular absorption. Therefore, it is required to compute the fraction of incident EM waves at a specific frequency that can pass through the medium, namely as the transmittance of a medium τ, which is obtainable by using the

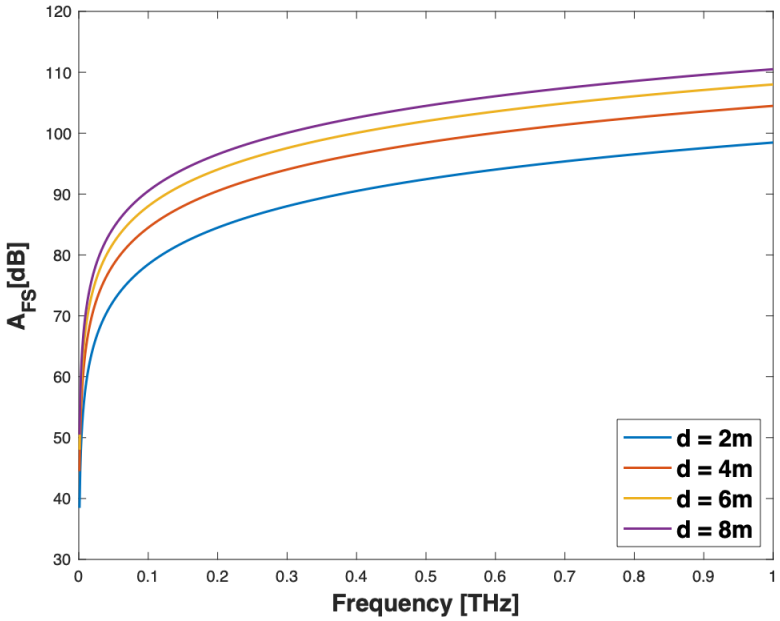

Figure 2.3. Free space pathloss as a function of frequency and distance d.

Beer-Lambert Law. i.e. [7, 20]:

$$\tau(f,d) = \frac{P_0}{P_{in}} = e^{-\kappa(f)d}, \tag{2.2}$$

where f refers to the frequency of the EM wave, d stands for the total path length, P_{in} and P_0 are the powers of the incident and radiated waves, respectively, and κ is the medium absorption coefficient in m^{-1} which depends on the composition of the medium. It shows the specific mixtures of molecules found along with the medium. In [7, 20], the way of computing κ is explained in detail. In the following tried to shortly explain how to compute κ. κ can be computed as [7]:

$$\kappa(f) = \sum_{i,\mathfrak{g}} \kappa^{i,\mathfrak{g}}(f), \tag{2.3}$$

where $\kappa^{i,\mathfrak{g}}$ is related to the individual absorption coefficient for isotopologue i of gas $\mathfrak{g}$. In order to compute the absorption coefficient of the medium, it is required to sum all the absorption coefficient related to the different isotopologues of the gases presented in the medium.
The absorption coefficient of the isotopologue i of gas $\mathfrak{g}$ $\kappa^{i,\mathfrak{g}}$, in m^{-1}, for a molecular volumetric density (i.e. the number of molecules per volume unit) $Q^{i,\mathfrak{g}}$, in $molecules/m^3$, at pressure p and temperature T can be computed as:

$$\kappa^{i,\mathfrak{g}}(f) = \frac{p}{p_0}\frac{T_{STP}}{T} Q^{i,\mathfrak{g}} \varsigma^{i,\mathfrak{g}}(f), \tag{2.4}$$

where $Q^{\mathfrak{g}}$ is the molecular volumetric density of gas $\mathfrak{g}$, that is, the number of molecules per volume unit in $molecules/m^3$ at pressure p and temperature T.

p_0 and T_0 denote Standard-Pressure-Temperature (STP) values, $T_0 = 273.15°K$ and $p_0 = 1\ atm$. $\varsigma^{i,\mathfrak{g}}$ is the absorption cross-section of gas $\mathfrak{g}$ in $m^2/molecule$, used to describe the absorption properties of a single molecule measured in the area [21]. It is obvious that the absorption coefficient of the isotopologue i of gas $\mathfrak{g}$, $\kappa^{i,\mathfrak{g}}$, depends on the total number of the molecules per volume unit $Q^{i,\mathfrak{g}}$. In other words, the total absorption depends on the number of molecules of a given gas that are found along the path and can be obtained from utilizing Ideal Gas Law as:

$$Q^{i,\mathfrak{g}} = \frac{n}{v} q^{i,\mathfrak{g}} N_A = \frac{p}{\mathbb{R}T} q^{i,\mathfrak{g}} N_A, \tag{2.5}$$

where n is the total number of moles of the gas mixture that is being considered, v stands for the volume, $q^{i,\mathfrak{g}}$ is the mixing ratio for the isotopologue i of gas $\mathfrak{g}$, mixing ratio usually refers to the mole ratio which is defined as the amount of a constituent divided by the total amount of all other constituents in a mixture, N_A stands for the Avogadro constant and $\mathbb{R}$ is the gas constant and all of these parameters can be found in HITRAN database. Note that in the HITRAN database, the mixing ratio of the specific gas, $q^{\mathfrak{g}}$, should be used for all of the isotopologues, instead of the individual mixing ratios $q^{i,\mathfrak{g}}$ [7].
Moreover, $\kappa^{i,\mathfrak{g}}$ also depends on the absorption cross section $\varsigma^{i,\mathfrak{g}}$, that can be further decomposed in terms of the line intensity $S^{i,\mathfrak{g}}$ for the absorption of the isotopologue i of gas $\mathfrak{g}$ and the spectral line shape $G^{i,\mathfrak{g}}$ as:

$$\varsigma^{i,\mathfrak{g}}(f) = S^{i,\mathfrak{g}} G^{i,\mathfrak{g}}(f), \tag{2.6}$$

in which $S^{i,\mathfrak{g}}$ refers to the strength or the absorption peak amplitude of a specific type of molecules, isotopologue i of gas $\mathfrak{g}$, and is directly obtained from the HITRAN database. Therefore, the only variable that is needed to define the absorption cross section is line shape $G^{i,\mathfrak{g}}$. In order to obtain $S^{i,\mathfrak{g}}$, it is necessary to determine the position of the resonant frequency, $f_c^{i,\mathfrak{g}}$, for the isotopologue i of gas $\mathfrak{g}$ that increases linearly with the pressure p from its zero-pressure position p_0 as [7]:

$$f_c^{i,\mathfrak{g}} = f_{c_0}^{i,\mathfrak{g}} + \varsigma^{i,\mathfrak{g}} p/p_0, \tag{2.7}$$

where $f_{c_0}^{i,\mathfrak{g}}$ is the zero-pressure position of the resonance and $\varsigma^{i,\mathfrak{g}}$ is the linear pressure shift which all of these values can be taken from HITRAN database directly.
The absorption from a particular molecule is not confined to a single frequency but spread over a range of frequencies that this spreading is shown by the collision between the molecules of the same gas. The absorbing gas is often a trace gas mixed in with the air; in this case, the trace gas's molecule shall nearly always collide with a Nitrogen or an Oxygen molecule. Hence, there are two different line broadening, namely as foreign broadening(air), line broadening due to trace gas molecules colliding with air molecules, and "self broadening" that is line broadening due to collisions with like trace gas molecules. The amount of this broadening depends on the molecules involved in the collisions, and it is usually referred to as the Lorentz half-width coefficient $\alpha_L^{i,\mathfrak{g}}$ that can

be obtained as a function of the air and self-broadened half-widths, α_0^{air} and $\alpha_0^{i,\mathfrak{g}}$ respectively, as:

$$\alpha_L^{i,\mathfrak{g}} = \left[\left(1 - q^{i,\mathfrak{g}}\right)\alpha_0^{air} + q^{i,\mathfrak{g}}\alpha_0^{air}\right]\left(\frac{p}{p_0}\right)\left(\frac{T_0}{T}\right)^{\iota}, \tag{2.8}$$

where $q^{i,\mathfrak{g}}$ is the mixing ratio for the isotopologue i of gas $\mathfrak{g}$, p is the system pressure, p_0 refers to the reference pressure, T_0 is the reference temperature, T refers to the system temperature, and ι is the temperature broadening coefficient. The values of ι, α_0^{air} and $\alpha_0^{i,\mathfrak{g}}$ can be obtained directly from the HITRAN database. It can be seen that the number of molecules either increases the amplitude of the peak of the absorption, equation (2.6), and change the shape of the absorption peak and make it wider [7]. In the THz frequencies, Van Vleck-Weisskopf asymmetric line shape [7] is applied as:

$$F^{i,\mathfrak{g}}(f) = 100c\frac{\alpha_L^{i,\mathfrak{g}}}{\pi}\frac{f}{f_c^{i,\mathfrak{g}}}\left[\frac{1}{\left(f - f_c^{i,\mathfrak{g}}\right)^2 + \left(\alpha_L^{i,\mathfrak{g}}\right)^2} + \frac{1}{\left(f + f_c^{i,\mathfrak{g}}\right)^2 + \left(\alpha_L^{i,\mathfrak{g}}\right)^2}\right], \tag{2.9}$$

where f stands for the frequency of the EM wave, c is the speed of light in the vacuum, $\alpha_L^{i,\mathfrak{g}}$ is the Lorentz half-width coefficient for the isotopologue i of gas $\mathfrak{g}$ and $f_c^{i,\mathfrak{g}}$ is the resonant frequency for the isotopologue i of gas $\mathfrak{g}$. Moreover another adjustments is done to account the continuum absorption in [7] is proposed as:

$$G^{i,\mathfrak{g}}(f) = \frac{f}{f_c^{i,\mathfrak{g}}}\frac{tanh\left(\frac{\text{þ}cf}{2k_BT}\right)}{tanh\left(\frac{\text{þ}cf_c^{i,\mathfrak{g}}}{2k_BT}\right)}F^{i,\mathfrak{g}}(f), \tag{2.10}$$

þ is the Planck constant, k_B is the Boltzmann constant, T is the system temperature and c is the speed of light.
Now all the parameters required to compute the total molecular absorption for each isotopologue i of gas $\mathfrak{g}$ presented in the medium are provided. The total attenuation due to molecular absorption for an EM waves that is traveling a distance d can be obtained from the transmittance of a medium which is given by equation (2.2), through:

$$A_M(f,d) = \frac{1}{\tau(f,d)} = e^{\kappa(f)d}, \tag{2.11}$$

which can be written in dB as:

$$A_M(f,d)[dB] = \kappa(f)d10log_{10}e. \tag{2.12}$$

At THz frequencies, the major contribution to molecular absorption is given by water vapor molecules [7]. Several studies, for example [5, 11], have investigated the influence of molecular absorption in different environmental conditions.

Results show that an increase in the number of water vapor molecules leads to an increase in attenuation caused by molecular absorption. Figure 2.4 shows molecular absorption as a function of frequency per unit of distance in dB, A_M [dB/m], that is evaluated with am model [20] for an indoor office with an air pressure $p = 1$ atm, a temperature $T = 298.55$ °K, and Relative Humidity (RH), that is used as a measure of water vapor content in the air, of 30 % vs. 70 %. Figure 2.4 shows that when the number of water vapor molecules increases, that is with a larger RH, A_M increases. It also shows that higher values of A_M are obtained at higher frequencies. Figure 2.5 shows molecular absorption A_M [dB/m], by oxygen (O_2) (Fig. 2.5a) and water (H_2O) (Fig. 2.5b) as a function of frequency under the condition $p = 1$ atm, $T = 298.55$ °K and $d = 1$ m. Note that the contribution of oxygen is negligible compared to water vapor at THz frequencies, as can be easily seen from the different scales of A_M in Fig. 2.5a vs. Fig. 2.5b; for instance, $A_M \approx 6.8619 \times 10^{-5}$ [dB/m] for O_2 at 1 THz, while $A_M \approx 0.7349$ [dB/m] for H_2O at the same frequency.
In summary, the total attenuation experienced by an EM wave at THz frequencies is the sum in dB of the free space attenuation A_{FS}, and the attenuation due to the molecular absorption attenuation, A_M:

$$A[dB] = A_M[dB] + A_{FS}[dB], \tag{2.13}$$

where A_{FS} can be written in dB as:

$$A_{FS}[dB] = 20\log_{10}(d) + 20\log_{10}(f) - 147.5582. \tag{2.14}$$

For instance, the total attenuation experienced when $d = 4$ m, $p = 1$ atm, $T = 298.55$ °K and $RH = 70$ % at $f = 1$ THz is $A \approx 110.62$ [dB]. Since $A_{FS} \approx 104.48$ [dB] and $A_M \approx 6.14$ [dB].

2.2.3 Diffuse scattering

One of the THz waves' characteristics is that the surfaces that consider smooth in lower frequencies do not consider smooth in higher frequencies. Therefore, one face with diffuse scattering phenomenon from rough surfaces. Rayleigh [22] suggested a way to understand that under which circumstances a surface is considered smooth or rough. Rayleigh found this answer based on three measurable parameters, such as the maximum height of the surface irregularities h, grazing angle of the incident wave ϕ, and the wavelength of the wave λ. These conditions lead to the so-called Rayleigh criterion. Consider incident and reflected waves at height 0 (wave 1) and at height h (wave 2), as shown in Fig. 2.6. The path difference Δr, and phase difference $\Delta\varphi$ of the incident and reflected waves at the two elevations of the surface are given by:

$$\Delta r = 2h sin\phi \tag{2.15}$$

and

$$\Delta\varphi = \frac{2\pi}{\lambda}\Delta r = \frac{4\pi h}{\lambda} sin\phi. \tag{2.16}$$

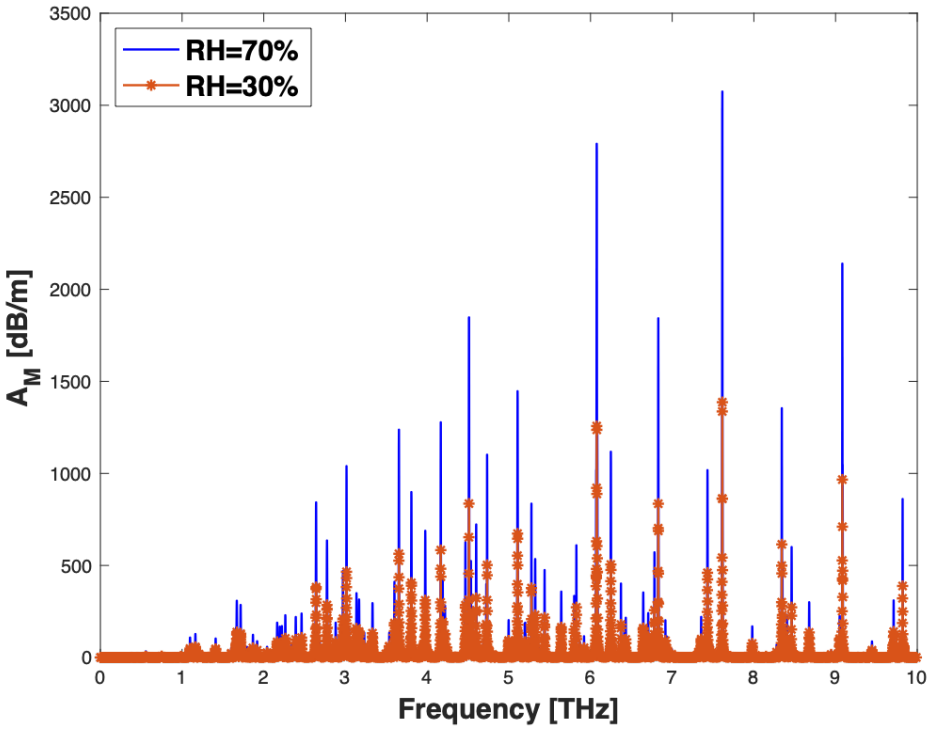

Figure 2.4. Molecular absorption per unit of the distance in dB, A_M [dB/m], as a function of frequency, evaluated for two different Relative Humidity values (30% and 70%), room temperature $T = 298.55$ °K, air pressure $p = 1$ atm, $d = 1$ m and $p_0 = 1$ atm, $T_0 = 273.15$ °K.

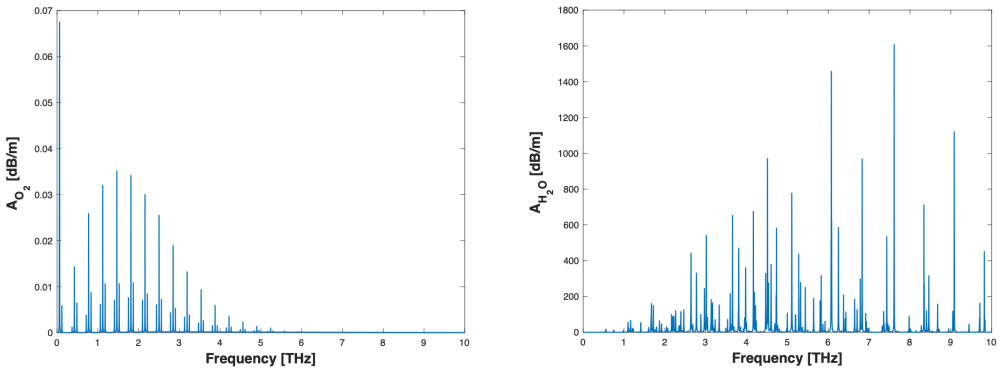

(a) O_2 molecules **(b)** H_2O molecules

Figure 2.5. Molecular absorption per unit of the distance in dB, A_M [dB/m], as a function of frequency for two specific molecules (a) O_2 and (b) H_2O, considering $d = 1$ m, pressure $p = 1$ atm and temperature $T = 298.55$ °K.

If the phase difference is small, the two rays will be almost in phase as they

are in the case of a perfectly smooth surface. If the phase difference increases, the two rays will interfere until $\Delta\varphi = \pi$ they will be in phase opposition and canceled. Thus, the surface scatters and is rough. Rayleigh chose the value between two cases, $\Delta\varphi = \frac{\pi}{2}$, and put this value in equation (2.15) to find the relation known as Rayleigh criterion. The Rayleigh criterion states that a surface is smooth if $\Delta\varphi < \frac{\pi}{2}$, that is:

$$h < \frac{\lambda}{8sin\phi} \tag{2.17}$$

Note that $\Delta\varphi \to 0$ if $\frac{h}{\lambda} \to 0$ or $sin(\phi) \to 0$. Therefore, the degree of roughness

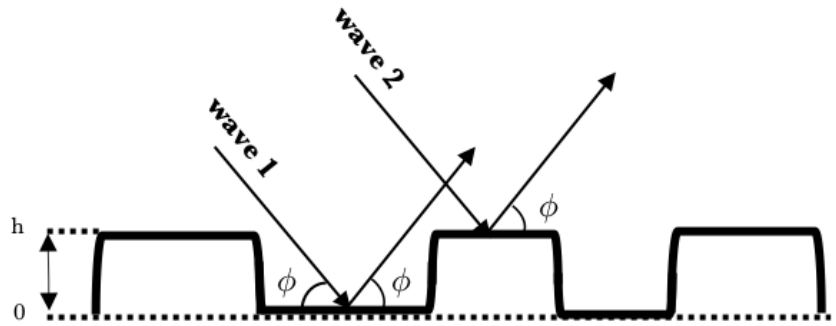

Figure 2.6. Profile of a surface characterized by irregularities of elevation h.

of a surface depends on the angle of incidence ϕ and the frequency of the incoming wave.
In Fig. 2.7, the Rayleigh criterion for different frequencies and different grazing angles is examined. Note that regarding Rayleigh criterion for $h < \frac{\lambda}{8sin\phi}$ the surface consider smooth, so as long as the value of h becomes bigger, reaching this criterion is more accessible, but on the other hand, if the value of h becomes smaller, achieving this value becomes more difficult, and the surface for smaller height consider rough. As it is shown in the equation (2.17), the value of h is directly related to the wavelength and the result shown in Fig. 2.7 depict this fact. Moreover, table 2.1 shows the results of applying the Rayleigh criterion to THz frequencies, in particular, 100 GHz, 1 THz, 10 THz, and at three grazing angles, $\pi/12$, $\pi/6$, $\pi/3$. At lower frequencies, the maximum value of h is higher for a surface to be considered as smooth. Table 2.1 also shows the impact of grazing angle ϕ, on the surface roughness, i.e., the smaller ϕ, the smoother the surface.

Although the Rayleigh criterion has been used for many years due to its simplicity, it is not very precise [23]. In order to better describe the roughness of a surface, statistical parameters are needed. Therefore, not only the variation of the surface height but also another parameter indicating whether the hills and valleys of the surface are close or far from each other must be considered. The surface pattern can be described by the standard deviation of its height σ from the average value of height h. Also, the correlation length T_{corr}, computed

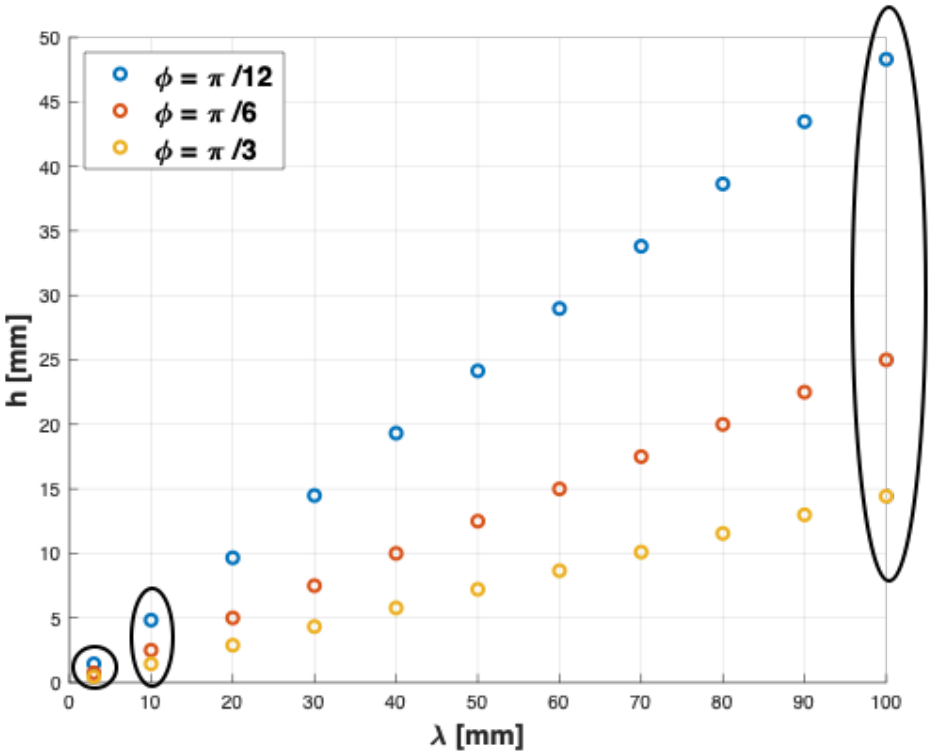

Figure 2.7. The different values of grazing angle ϕ for the same wavelength show the impact of ϕ on the surface roughness when $\phi \to 0$ the surface becomes smoother

with respect to the surface profile, can be used to describe the surface in statistical terms. Moreover, another parameter g, called 'roughness factor' [4, 2, 23], can be used as a parameter to grade the roughness of the specific random surfaces with Gaussian height distribution for a given frequency. This roughness parameter will be introduced in more detail in section 2.2.4.
Note that when an EM wave hits a smooth surface, it is reflected according to Fresnel law of reflection, ruling that the incoming ray is specularly reflected in one single direction. In contrast, when the surface is rough, the reflected ray scatters in various directions. Figure 2.8a shows the geometry of the reflection where $\overrightarrow{E_1}$ is an incident wave, $\overrightarrow{r}$ is the position vector of the hit point on the surface, $\overrightarrow{k_1}$ indicates the direction of the incident wave, $\overrightarrow{k_2}$ indicates the direction of the reflected wave, and θ_1 and θ_2 are the angles of the incident vs. reflected wave with respect to the normal to the surface. In the case of a smooth surface, most of the energy is reflected in the specular direction, i.e., $\theta_1 = \theta_2$, and both incident and reflected waves are in the same plane as the normal vector to the surface, called the plane of incidence. In the case of a rough surface, however, the reflected wave may be out of the plane of incidence, and it does not follow the laws of reflections. Depending upon the surface's roughness, the amount of energy in the specular direction decreases, and part of the energy reflects in other directions. Figure 2.8b shows the geometry of

Table 2.1. Maximum height for a surface to be considered as smooth according to the Rayleigh criterion for EM waves at 100 GHz, 1 THz, 10 THz and for three values of the grazing angle ϕ: $\frac{\pi}{12}$, $\frac{\pi}{6}$, $\frac{\pi}{3}$.

	f = 100 GHz (λ = **3 mm**)	**f = 1 THz** (λ = **0.3 mm**)	**f = 10 THz** (λ = **0.03 mm**)
$\phi = \frac{\pi}{12}$	$h < 1.4\ mm$	$h < 0.14\ mm$	$h < 14\ \mu m$
$\phi = \frac{\pi}{6}$	$h < 0.75\ mm$	$h < 0.075\ mm$	$h < 7.5\ \mu m$
$\phi = \frac{\pi}{3}$	$h < 0.433\ mm$	$h < 0.0433\ mm$	$h < 4.3\ \mu m$

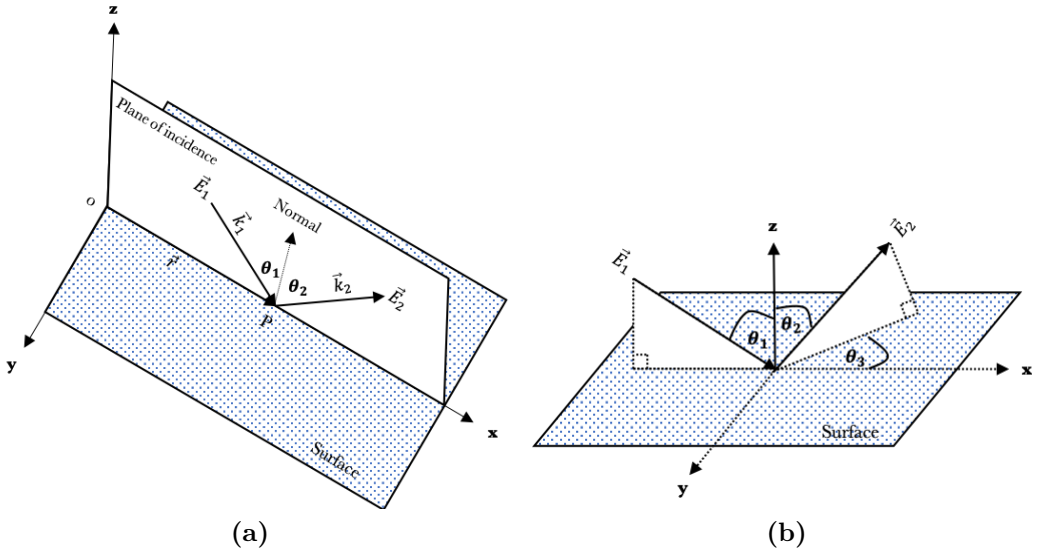

(a) **(b)**

Figure 2.8. Geometry of reflection from a surface. (a) incident wave $\overrightarrow{E_1}$ and reflected wave $\overrightarrow{E_2}$ are in the same plane with normal vector to the surface, i.e. the plane of incidence. (b) $\overrightarrow{E_2}$ is reflected out of plane of incidence with a deviation angle θ_3. $\overrightarrow{r}$ is the position vector of the hit point on the surface, $\overrightarrow{k_1}$ indicates the direction of $\overrightarrow{E_1}$, $\overrightarrow{k_2}$ indicates the direction of $\overrightarrow{E_2}$, θ_1 and θ_2 are the angle of incident vs. reflection wave respectively.

the reflection on a rough surface in which θ_3 is the deviation angle of the plane of the scattered wave $\overrightarrow{E_2}$, from the plane of the incidence wave $\overrightarrow{E_1}$.

In the presence of obstacles or reflections, besides molecular and free space attenuation, scattering attenuation must, therefore, be considered. Hence, the total attenuation becomes:

$$A_{tot}[dB] = A_M[dB] + A_{FS}[dB] + A_{sca}[dB], \tag{2.18}$$

where A_{sca} is scattering attenuation.

Analytical theories such as the small perturbation method proposed by Rice [24] and the Kirchhoff theory [23], approximate the energy of reflected rays from a rough surface. The condition for the validity of perturbation theory is that the root mean square (RMS) height of the random rough surface h_r, should be much smaller than the incident wavelength, which is usually expressed as $kh_r \ll 1$, with $k = \frac{2\pi}{\lambda}$ the wavenumber. This method, hence, is

not relevant for surfaces with large RMS height and also can not adequately address many of the surfaces at THz frequencies [4, 25, 26]. On the other hand, the Kirchhoff theory was shown to be applicable for surfaces with large RMS height [23] and is well suited for simulating THz scattering from rough surfaces [4]. Moreover, in order to analyze the effects of reflected and scattered rays at THz frequencies, Kirchhoff theory can be implemented straightforwardly by applying a ray-tracing algorithm with a reasonable computational efficiency [4] as explained in detail in the next section.

2.2.4 Kirchhoff scattering theory

Kirchhoff's physical reflectance model describes the reflection of the electromagnetic plane waves from smooth and rough surfaces. A detailed derivation of this model can be found in [23]. This model is derived from the EM waves reflection theory [23]. This section briefly introduces the Kirchhoff physical reflectance model and highlights the key steps involved in the model's derivation. Moreover, we tried to clarify the assumptions required in the model.
EM waves are made up of electric and magnetic fields. EM waves propagating in free space can be considered as Transverse-Electro-Magnetic (TEM), meaning that TEM waves have their electric(E)-field and magnetic(M)-field in directions, which are perpendicular to the propagation direction. Moreover, EM waves in free space are spherical. Suppose that a source radiates an EM wave. When the EM wave travels far enough and strikes a point on a surface, the spherical waves radiated by the source may be assumed to be plane waves at that point, i.e., at the region near to that point, it locally looks like a plane wave since the radius of curvature becomes so large. In other words, when the distance from the radiating antenna becomes larger than the Fraunhofer distance, we can consider locally, the EM wave as a plane wave. The Fraunhofer distance is defined as:

$$d_F = \frac{2D^2}{\lambda}, \tag{2.19}$$

where D is the largest dimension (or diameter) of the radiator, and λ is the wavelength of the considered wave. d_F provides the limit between far and near field; therefore, for a distance d greater than d_F we can consider locally the EM wave as a plane wave. In Fig. 2.9, a plane wave at an instant time t_0 is depicted, with $\hat{e}$ being the unit vector that indicates the direction of the E-field, which is perpendicular to the direction of M-field. $\hat{e}$ is orthogonal to the propagation direction. Note that at time t_0, all the points on the plane PW, with position vector $\overrightarrow{r}$, experience the same E and M-field. A plane wave in free space can be expressed only by its E-field vector. As a matter of fact, from Maxwell equations we have

$$\overrightarrow{H} = -\eta_0 \overrightarrow{r} \times \overrightarrow{E}, \tag{2.20}$$

where $\overrightarrow{H}$ is the M-field vector and $\eta_0 = 376.73\Omega$ is the impedance of free space. Let $\overrightarrow{E}$ be the E-field vector of a plane wave. At an observation point with

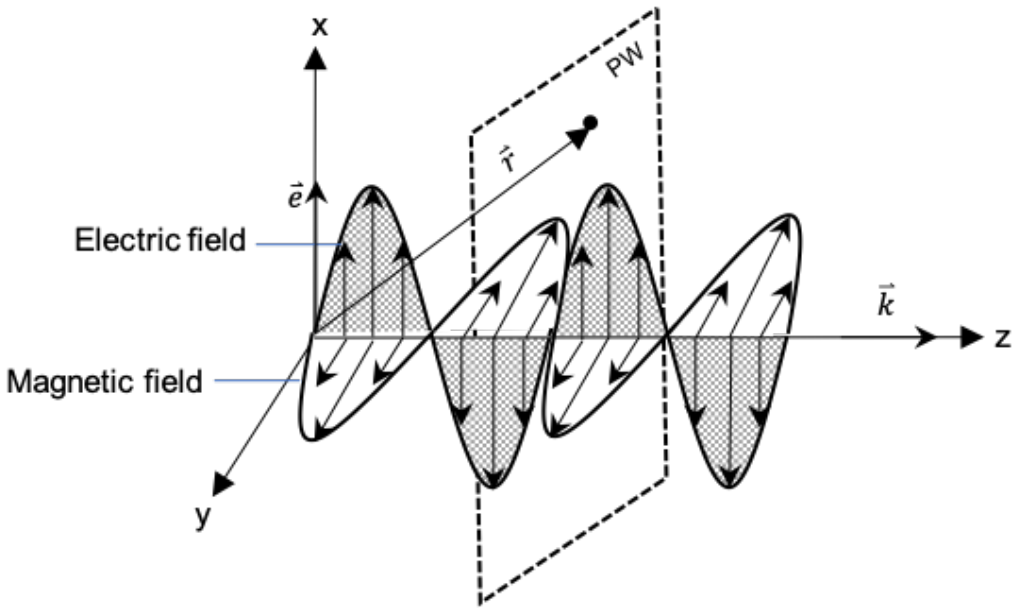

11

Figure 2.9. An EM plane wave at a particular instant of time. $\hat{e}$ indicates the direction of E-field, $\overrightarrow{r}$ is the position vector of a point, $\overrightarrow{k}$ stands for the propagation vector.

position vector $\overrightarrow{r} = x\hat{x} + y\hat{y} + z\hat{z}$ (see Fig. 2.8a and Fig 2.9), $\overrightarrow{E}$ can be expressed as:

$$\overrightarrow{E} = E_0\hat{e}\ \exp\left[j(-\overrightarrow{k}\cdot\overrightarrow{r} + \omega t)\right], \tag{2.21}$$

where E_0 is the amplitude of the E-field and $\overrightarrow{k} = k\hat{k}$ is the wave vector, its unit vector $\hat{k}$ points in the direction of propagation and its magnitude $k = \frac{2\pi}{\lambda}$ is called wave number or propagation constant. ω is the radian frequency of the field oscillation, and t is the time. Note that ωt can be dropped because, in Kirchhoff theory, only the instantaneous scattering of the incident wave is addressed [23].

The notation used in this section will be used for all the thesis. We shall use the Cartesian coordinate x,y,z with the origin O = (0,0,0) and unit vectors $\hat{x}$, $\hat{y}$, $\hat{z}$. The height of a rough surface is determined by the function $h = h(x, y)$, and the mean level of the surface height is the plane $z = 0$. All parameters related to the incident field shown by subscript 1, and those related to the scattered field shown by subscript 2. The incident wave's polarization is determined by the direction of the electric field shown by unit vector $\hat{e_1}$. For parallel polarization, $\hat{e_1}$ lies in the plane of incidence, while for perpendicular polarization, $\hat{e_1}$ is normal to the plane of incidence. The incident field is denoted by the scalar E_1, with:

$$E_1 = \overrightarrow{E_1}\cdot\hat{e_1}. \tag{2.22}$$

When an incident plane wave hits a surface point P, the electrons on the surface experience forces by the electromagnetic field carried by the incident wave. These forces lead to electrons movements and generate surface currents.

Consequently, the newly generated surface currents generate an EM field E_s that interacts with the incoming wave field. The resulting field E_s must satisfy the wave equation [23]:

$$\nabla^2 E_s + k^2 E_s = 0. \tag{2.23}$$

The scattered field can be found, in any direction, from the field on the surface. Consider that the height of a rough surface is determined by the function $h = h(x, y)$, and the mean level of the surface height is the plane $z = 0$. Let B be the point of observation and let R' be the distance from B to a point, $x, y, h(x, y)$ on the surface. In order to deal with plane scattered waves rather than spherical ones (i.e., with the direction of θ_2 rather than point B), R' is assumed to be larger than the Fraunhofer distance. However, this assumption is withdrawn by admitting a small error or sacrificing the simplicity of computation, as shown in Fig. 2.10.

In order to find the scattered field E_2 at point B, let consider volume V

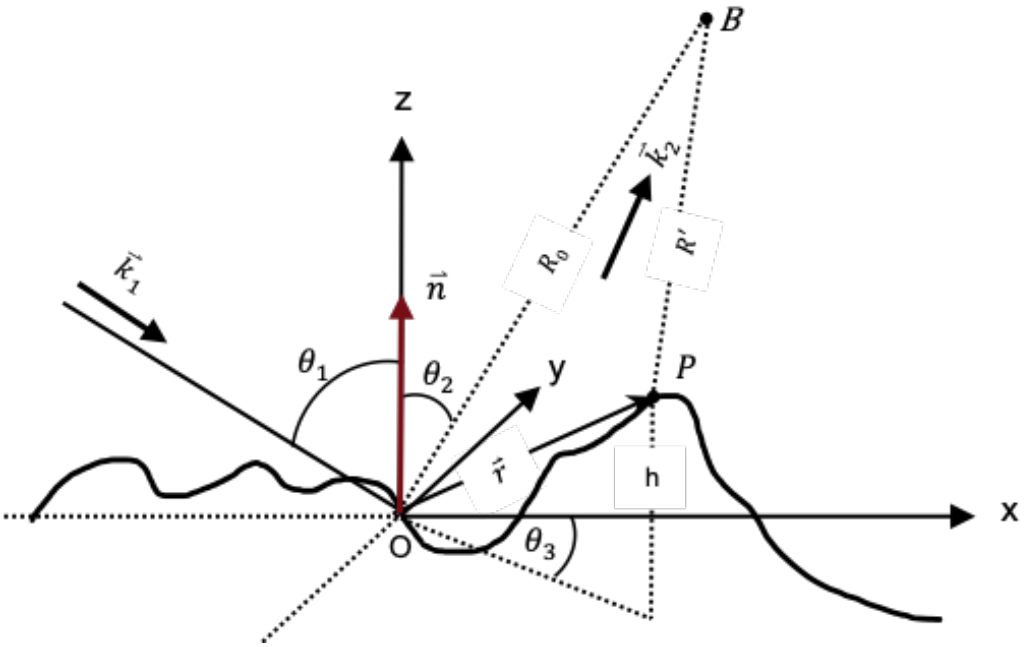

Figure 2.10. Plane wave incident on a rough surface. The height of the surface is a function of $h = h(x, y)$, $\overrightarrow{r}$ is the position vector of an point on the surface P, B is the observation point, $\overrightarrow{n}$ is normal vector, $\overrightarrow{k_1}$ and $\overrightarrow{k_2}$ are the incident and reflected plane wave propagation vector, R_0 and R' are the distance between B and the origin and P respectively. θ_1, θ_2 and θ_3 are the angles of incidence, reflected and deviated, respectively.

bounded by the surface S. Assume that the point B is outside V. The field E_s is continuous, equation (2.23) must, therefore, be satisfied everywhere inside V. Moreover, assume that the nearest point to B experiences almost the same field as B. Regarding these assumptions, the scattered field E_2 at point B can

be obtained [23] from equation (2.23) as:

$$E_2(B) = \frac{1}{4\pi} \iint_S \left((E)_S \frac{\partial \psi}{\partial n} - \psi \left(\frac{\partial E}{\partial n} \right)_S \right) dS, \tag{2.24}$$

where

$$\psi = \frac{e^{jk_2R'}}{R'}, \tag{2.25}$$

where, $k_2R' = k_2R_0 - \overrightarrow{k_2} \cdot \overrightarrow{r}$. R_0 is the distance between the point B and O, $R_0 = OB$ (see Fig. 2.10). Equation (2.24) is the Helmholtz integral and gives the solution of the wave equation, equation (2.23), at an interior point of region V, in terms of the surface field, E_S, and the normal derivative of the field E_S on the surface S ($^{\partial E}/_{\partial n}$). More details about Helmholtz integral is provided by [23]. E and $^{\partial E}/_{\partial n}$ are the field, and its normal derivative on the surface S. These two quantities are in general unknown, and Kirchhoff theory, therefore, is used to approximate the value of the field and its normal derivative at each point on the surface.
The Kirchhoff theory's basic assumption is that the field at any point on the surface E_s is approximated by the field that would be present on the tangent plane of the considered point. Based on this assumption, the field at any point on the surface can be expressed as the sum of the incident field E_1 and the reflected field $E_2 = \gamma E_1$ as:

$$E_S = E_1 + \gamma E_1. \tag{2.26}$$

where γ is the Fresnel reflection coefficient, which determines the fraction of the incident field reflected by the smooth surface of the tangential plane at the considered point. In addition, the normal derivative of the field can be found by differentiating this equation as:

$$\left(\frac{\partial E}{\partial n} \right)_S = (1 - \gamma) E_1 \overrightarrow{k_1} \cdot \overrightarrow{n}, \tag{2.27}$$

where $\overrightarrow{n}$ is the normal vector to the surface at the considered point. Although the considered surface might be rough, Kirchhoff approximation implies that the surface is locally smooth, and therefore the Fresnel coefficient is applicable. Hence, the validity of the Kirchhoff theory's approximation holds when the radius of curvature of the irregularities of the surface is larger than the wavelength, i.e., does not contain any sharp edges, as shown in Fig. 2.11a, but ceases to hold if the surface includes sharp edges, (see Fig. 2.11b). The limitation value related to the radius of curvature of the surface can be defined as [23]:

$$4\pi r_c cos\vartheta \gg \lambda, \tag{2.28}$$

where r_c is the radius of curvature of the surface at the point of reflection, ϑ is the local angle of incident, i.e., the angle of incidence with respect to the normal at the considered point. Table 2.2 depicts the values of r_c for three

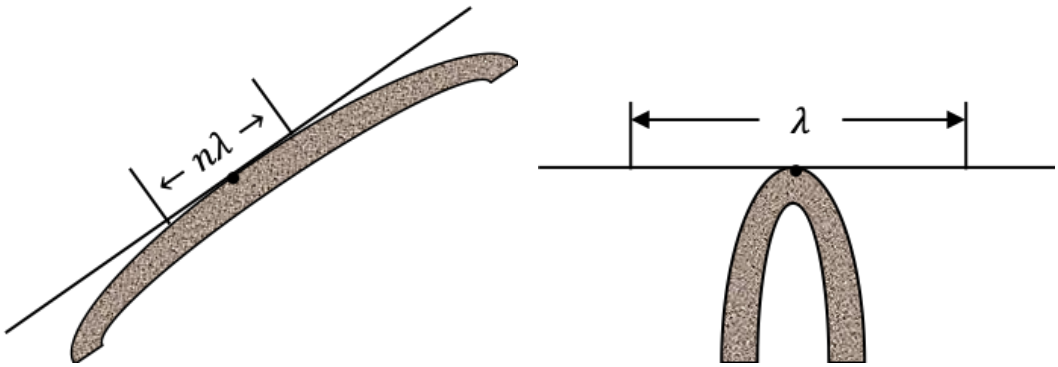

Figure 2.11. The tangent plane at a general point on the rough surface. The radius of curvature is (a) large, (b) small in relation to the wavelength λ.

different frequencies $f = 100$ GHz, $f = 1$ THz, $f = 10$ THz. It is shown that for lower wavelength, i.e., higher frequencies, such as 0.03 mm, a smaller r_c is required to be able to apply the theory. However, when one moves to higher wavelengths, i.e., lower frequencies, such as 3 mm, larger r_c are required, meaning that the Kirchhoff theory is well suited for high frequencies such as THz frequencies. Table 2.2 also demonstrates the impact of the angle of incident, ϑ; for larger ϑ, larger r_c are required.

Table 2.2. The required value of r_c for the three given λ and three values of $\vartheta = \pi/6$, ϑ to be able to apply Kirchhoff theory

	f = 100 GHz ($\lambda =$ **3 mm**)	**f = 1 THz** ($\lambda =$ **0.3 mm**)	**f = 10 THz** ($\lambda =$ **0.03 mm**)
$\vartheta = \frac{\pi}{6}$	$r_c >> 275.6\ \mu m$	$r_c >> 27.56\ \mu m$	$r_c >> 2.756\ \mu m$
$\vartheta = \frac{\pi}{4}$	$r_c >> 337.6\ \mu m$	$r_c >> 33.76\ \mu m$	$r_c >> 3.376\ \mu m$
$\vartheta = \frac{\pi}{3}$	$r_c >> 477.4\ \mu m$	$r_c >> 47.74\ \mu m$	$r_c >> 4.774\ \mu m$

For an infinite conductive surface, the Fresnel reflection coefficient is $\gamma = 1$, meaning that in the case of a perfectly smooth surface, the reflected wave has the same amplitude as the incident wave.
In order to find the scattered field E_2 by evaluating integral equation (2.24), we assume a rectangular surface area $A = 4XY$, i.e., with the dimension of $2X$ in x and $2Y$ in y directions. Moreover, assuming the observation point B at a distance far from the surface compared to the dimensions of the considered area and as a result, $\overrightarrow{k_2}$ is constant over the entire surface. Hence, the distance R' in Fig. 2.10 can be computed as:

$$k_2 R' = k_2 R_0 - \overrightarrow{k_2} \cdot \overrightarrow{r}. \tag{2.29}$$

where R_0 is the distance of B from origin. By substituting equations (2.26), (2.27) and (2.29), in equation (2.24), the scattered field E_2 can be found as:

$$E_2 = \frac{E_{01} ike^{ikR_0}}{4\pi R_0} \int_{-X}^{X} \int_{-Y}^{Y} (ah'_x + ch'_y - b) e^{i\overrightarrow{v}\cdot\overrightarrow{r}} dxdy \tag{2.30}$$

where $\overrightarrow{v} = \overrightarrow{k_1} - \overrightarrow{k_2}$ and

$$\begin{aligned} \overrightarrow{v} &= (v_x, v_y, v_z) = k[(sin\theta_1 - sin\theta_2 cos\theta_3)\hat{x} - sin\theta_2 sin\theta_3 \hat{y} - (cos\theta_1 + cos\theta_2)\hat{z}] \\ a &= (1-\gamma)sin\theta_1 + (1+\gamma)sin\theta_2 cos\theta_3 \\ b &= (1+\gamma)cos\theta_2 - (1-\gamma)cos\theta_1 \\ c &= (1+\gamma)sin\theta_2 sin\theta_3 \end{aligned} \tag{2.31}$$

in which, h'_x and h'_y are the derivatives of the surface height in x and y directions, respectively, considering that the rough surface is introduced by the function $h = h(x, y)$ where the mean level of the surface height is the plane $z = 0$. By assuming a perfectly conducting surface, $\gamma_{TE} = 1$ and $\gamma_{TM} = -1$, where TE refers to transverse electric modes of propagation of the incident waves, TM refers to transverse magnetic modes of propagation, and then a, b, c in equation (2.30) becomes independent of x and y. Moreover, in [23], a scattering coefficient is introduced as:

$$\rho = \frac{E_2}{E_{20}} \tag{2.32}$$

where E_2 is the scattered field and E_{20} is the field reflected in the direction of specular reflection by a smooth, infinitively conductive plane with the same area and under the same angle of incidence θ_1 ($\theta_1 = \theta_2$ and $\theta_3 = 0$) at the same distance. Notice that, for the direction of specular reflection $v_x = 0$ regarding to the fact that for a smooth surface $h = h' = 0$, hence E_{20} can be found from equations (2.31) and (2.30) as:

$$E_{20} = \frac{ikA\cos\theta_1}{\pi} \frac{e^{ikR_0}}{R_0}, \tag{2.33}$$

where $A = l_x \cdot l_y$ is the illuminated area and l_x and l_y are the side length of area A. Moreover, from equations (2.30), (2.32) and (2.33) [23]:

$$\rho = \frac{F(\theta_1, \theta_2, \theta_3)}{A} \int\int_A e^{i\overrightarrow{v}\cdot\overrightarrow{r}} dA, \tag{2.34}$$

where $F(\theta_1, \theta_2, \theta_3)$ is the geometrical factor, which equation, given by Beckmann and Spizzichino in [23] is

$$F(\theta_1, \theta_2, \theta_3) = \frac{1 + \cos\theta_1 \cos\theta_2 - \sin\theta_1 \sin\theta_2 \cos\theta_3}{\cos\theta_1 (\cos\theta_1 + \cos\theta_2)}. \tag{2.35}$$

In order to derive quantitative results from eq. (2.34), a statistical description of the random surface is needed, i.e., the height function $h(x, y)$ should be defined. Generally, the exact surface profile is not available. Note that even if the surface profile is available, by using some methods, equation (2.30) is valid only for that specific profile.
When the exact surface is not available, statistical models of surfaces are typically adopted. Considering surfaces randomly rough with a Gaussian height distribution may cover many surfaces in indoor environments [4]. Although details on models will be given in chapter 3, it can be anticipated here that a surface can be characterized using two parameters: σ and T_{corr}. The standard deviation of the heights distribution σ and correlation length T_{corr}. Note that the mean height of a random surface is assumed to be $\langle h \rangle = 0$. The parameter T_{corr} is related to the auto-correlation function of the considered random surface. We can consider as a sufficiently general auto-correlation coefficient by the function:

$$C(r) = \frac{\langle h_1 h_2 \rangle}{\langle h_1 \rangle^2} = e^{-r^2/T_{corr}^2} \tag{2.36}$$

where h_1 and h_2 are the heights at two points on the surface p_1 and p_2 and r refers to the separation distance bewtween those. The parameter T_{corr} represents the distance at which the auto-correlation function coefficient $C(r)$ drops to e^{-1} [23]. T_{corr} controls the density of irregularities on the surfaces, small values of T_{corr} are related to very irregular surfaces, while larger values of T_{corr} are related to more regular surfaces. Surfaces with given profiles, i.e. periodic surfaces, can be considered as realization of the adopted statistical model and, therefore, their parameters σ and T_{corr} can be estimated.
It is obvious from equation (2.30) that E_2 and h are related and in [23] a fully description of finding mean field $< E_2 >$ and mean scattered power $< E_2 E_2^* > = < |E_2|^2 >$ in any direction at a given angle of incidence has been proposed. The mean power scattered in the direction of (θ_2, θ_3) with a given angle of incident θ_1 from an infinitely conductive rough surface with normally distributed height h, mean value of $< h >= 0$, and standard deviation of σ, and correlation length of T_{corr}, is:

$$\langle E_2 E_2^* \rangle_\infty = \frac{E_{01}^2 A^2 \cos^2\theta_1}{\lambda^2 R_0^2} e^{-g} \cdot \left(\rho_0^2 + \frac{\pi T_{corr}^2 F^2}{A} \sum_{m=1}^{\infty} \frac{g^m}{m!m} e^{-\frac{\left(v_x^2 + v_y^2\right) T_{corr}^2}{4m}} \right) \tag{2.37}$$

and regarding to equation (2.34) the mean scattered power coefficient $\langle \rho \rho^* \rangle_\infty$ is defined as [23]:

$$\langle \rho \rho^* \rangle_\infty = e^{-g} \cdot \left(\rho_0^2 + \frac{\pi T_{corr}^2 F^2}{A} \sum_{m=1}^{\infty} \frac{g^m}{m!m} e^{-\frac{\left(v_x^2 + v_y^2\right) T_{corr}^2}{4m}} \right) \tag{2.38}$$

where

$$\rho_0 = sinc(v_x l_x) \cdot sinc(v_y l_y), \tag{2.39}$$

and we introduce the Rayleigh roughness factor, g which is defined as

$$g = (v_z\sigma)^2 = k^2\sigma^2(\cos\theta_1 + \cos\theta_2)^2. \tag{2.40}$$

The Rayleigh roughness factor g is an indicator for the relative surface roughness at a given wavelength: while a Rayleigh factor $g \ll 1$ indicates a smooth surface, $g \approx 1$ indicates a moderately rough surface and $g \gg 1$ refers to a very irregular surface with noticeably diffuse scattering contribution. It is important to notice that g depends only on θ_1, θ_2 and σ while it is independent from T_{corr}. Table 2.3 shows the variation of g for different frequency and σ values. For the same values of σ, higher frequencies lead to higher Rayleigh's roughness factor. Moreover, by increasing σ at the same frequency, roughness increases.

Table 2.3. The variation of g for $\theta_1 = \theta_2 = \pi/4$ and three different values of $\sigma = 0.05$ mm, $\sigma = 0.15$ mm and $\sigma = 0.25$ mm

	f = 100 GHz (λ = **3 mm**)	**f = 1 THz** (λ = **0.3 mm**)	**f = 10 THz** (λ = **0.03 mm**)
σ = **0.05 mm**	$g = 0.0219$	$g = 2.193$	$g = 219.3$
σ = **0.15 mm**	$g = 0.1973$	$g = 19.739$	$g = 1973.9$
σ = **0.25 mm**	$g = 0.5483$	$g = 54.831$	$g = 5483.1$

Remind that the main limitation of applying the Kirchhoff theory is due to the fact that the radius of curvature of the surface must be much greater than the wavelength; that is, the illuminated area of the surface must be greater than the wavelength, $l_x \gg \lambda$, $l_y \gg \lambda$, $A \gg \lambda^2$ and obviously $T_{corr} \gg \lambda$. As shown in equation (2.38), the scattering coefficient of a surface contains can be roughly divided into two parts: $e^{-g}\rho_0^2$ is the coefficient related to the specular reflection. As a matter of fact, the specular reflection component is approximately zero except for a narrow θ_2 range around $\theta_2 = \theta_1$. The second part of equation (2.38) is the diffuse scattering coefficient, which is zero for a perfectly smooth surface, for which $g = 0$, and becomes larger when the surface is rough.
Note that, for smooth ($g \ll 1$) and very rough ($g \gg 1$) surfaces, the exponential series of in equation (2.38) can be approximated and therefore, for these two specific surface condition, the mean scattering coefficient can be introduced as:

$$\langle\rho\rho^*\rangle_\infty = \frac{\pi T_{corr}^2 F^2}{A\sigma^2 v_z^2} \cdot e^{-\frac{\left(v_x^2+v_y^2\right)T_{corr}^2}{4\sigma^2 v_z^2}} \qquad \text{for } (g \gg 1) \tag{2.41}$$

and

$$\langle\rho\rho^*\rangle_\infty = e^{-g} \cdot \left(\rho_0^2 + \frac{\pi T_{corr}^2 F^2}{A} \cdot e^{-\frac{\left(v_x^2+v_y^2\right)T_{corr}^2}{4}}\right) \qquad \text{for } (g \ll 1) \tag{2.42}$$

It is worth noting that the mean scattered coefficient does not only depend on σ, A and λ, but also on T_{corr}, θ_1, θ_2 and θ_3 (see equation (2.38)). In order to show the angular impact on the mean scattering coefficient for a rough surface, Fig. 2.12 shows $< \rho\rho^* >_\infty$ at $f = 300$ GHz as a function of θ_2, with $\theta_2 \in [0\,^\circ,\ 90\,^\circ]$ in steps of $0.01\,^\circ$, for an infinite conductive surface with realistic material parameters $T_{corr} = 0.18$ mm, $\sigma = 0.01mm$, $\sigma = 0.05mm$ and $\sigma = 0.1mm$, $\theta_1 = 30°$, $\theta_3 = 0$ and $l_x = l_y = 20 \cdot T_{corr}$. Figure 2.12 shows that the incident power is mainly reflected in the specular direction. By getting far from the specular direction, the mean scattering coefficient decreases rapidly, i.e. the scattered power can be neglected in the directions having large deviations from specular direction.

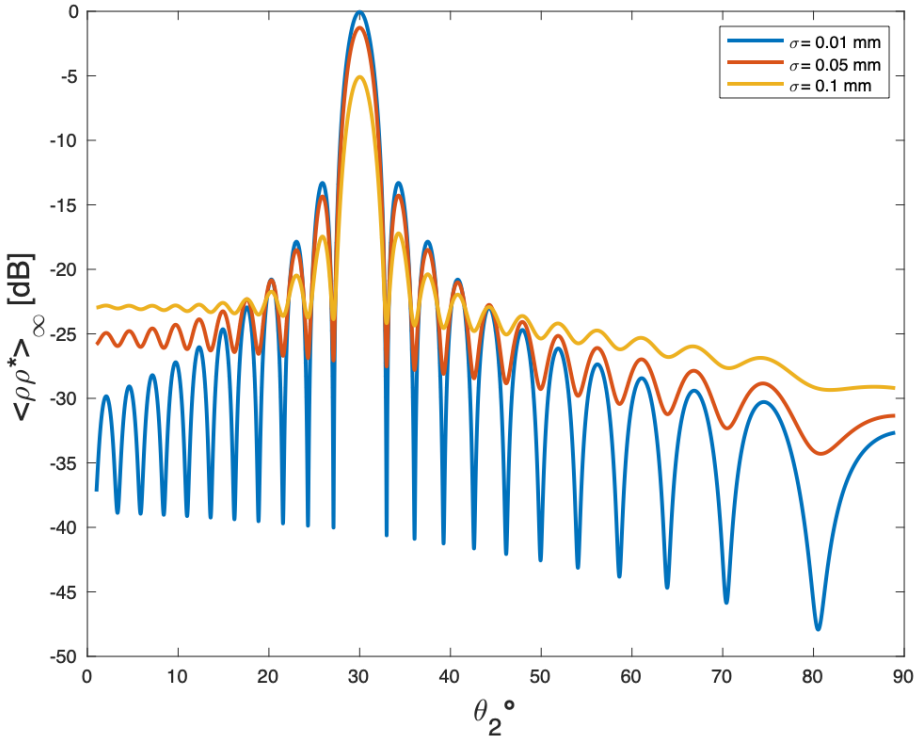

Figure 2.12. Mean scattering coefficient for a perfectly conductive surface at $f = 300$ GHz with $T_{corr} = 0.18$ mm and $\sigma = 0.01$ mm, $\sigma = 0.05mm$ and $\sigma = 0.1mm$, the incidence angle $\theta_1 = 30°$, θ_2 is varying from 0° to 90°, $\theta_3 = 0$ and $l_x = l_y = 20 \cdot T_{corr}$

2.2.5 Mean scattering power for a finite conductive surface

Until now, only an infinite (perfect) conductive surface was assumed so that this assumption leads to consider the Fresnel reflection coefficient $\gamma = 1$. This assumption was used to make the quantities a, b, c in equation (2.30) become constant, hence making it possible to evaluate the integral. However, in the

real world, one will not face infinite conductive surfaces, and it is required to find mean scattering power related to finite conductive surfaces. In order to find a valid equation for the mean scattering coefficient in a finite conductivity case, it is possible to approximate that equation by averaging the Fresnel reflection coefficient over the entire surface area and using it as a constant value $< \gamma >$ in the equation (2.30).
The Fresnel reflection coefficient depends on the angle of incidence, the electrical properties of the reflective material, and the incident wave's polarization. Note that, due to the lack of measured data related to material properties at high frequencies [3], the analysis of scattering from a rough surface in this study is limited to the frequencies up to 1 THz. Properties of the materials mostly used in indoor environments were measured for the frequencies between 0.1 and 1 THz in [27, 2, 4].
The Fresnel reflection coefficient for a smooth surface and a specific polarization can be found as [28]:

$$\gamma_{TE}(f) = \frac{\cos(\theta_1) - n_c\sqrt{1 - \left(\frac{1}{n_c}\sin(\theta_1)\right)^2}}{\cos(\theta_1) + n_c\sqrt{1 - \left(\frac{1}{n_c}\sin(\theta_1)\right)^2}}, \tag{2.43}$$

$$\gamma_{TM}(f) = \frac{-n_c\cos(\theta_1) + \sqrt{1 - \left(\frac{1}{n_c}\sin(\theta_1)\right)^2}}{n_c\cos(\theta_1) + \sqrt{1 - \left(\frac{1}{n_c}\sin(\theta_1)\right)^2}}, \tag{2.44}$$

where TE refers to transverse electric modes of propagation of the incident waves, TM refers to transverse magnetic modes of propagation, and $n_c = n - i\kappa_e$ is the frequency dependent complex refractive index in which κ_e denotes extinction coefficient. Moreover, suppose we refer to TM and TM polarization to the plane of incidence. We can easily find that horizontal polarization is equivalent to TE polarization and vertical polarization is equivalent to TM polarization. Moreover, it is possible to approximate equation (2.43) as:

$$\begin{aligned}
\gamma_{TE,approx}(f) &= \frac{cos(\theta_1) - n_c\sqrt{1 - \left(\frac{1}{n_c}sin(\theta_1)\right)^2}}{cos(\theta_1) + n_c\sqrt{1 - \left(\frac{1}{n_c}sin(\theta_1)\right)^2}} \\
&= -\left(1 + \frac{-2cos(\theta_1)}{cos(\theta_1) + \sqrt{n_c^2 - sin^2(\theta_1)}}\right) \\
&\approx -\left(1 + \frac{-2cos(\theta_1)}{\sqrt{n_c^2 - 1}}\right) \\
&\approx -exp\left(\frac{-2cos(\theta_1)}{\sqrt{n_c^2 - 1}}\right).
\end{aligned} \tag{2.45}$$

It is possible to approximate the Fresnel reflection coefficient, γ, by averaging it over the whole surface and use it as a constant $\langle\gamma\rangle$. In this way, the mean field, mean scattered power and mean scattering coefficient can be determined as [23]:

$$\langle E_2\rangle_f = \langle\gamma\rangle \cdot \langle E_2\rangle_\infty, \tag{2.46}$$

$$\langle E_2 E_2^*\rangle_f = \langle\gamma\gamma^*\rangle \cdot \langle E_2 E_2^*\rangle_\infty, \tag{2.47}$$

$$\langle\rho\rho^*\rangle_f = \langle\gamma\gamma^*\rangle \cdot \langle\rho\rho^*\rangle_\infty. \tag{2.48}$$

where subscript f indicates finite conductivity surface while subscript ∞ refers to a perfectly conductive surface.
In order to compare Beckmann-Kirchoff scattering coefficient for smooth and rough surfaces with the Rayleigh criterion, notice that the standard deviation of the height of the surface σ is equivalent to the height h in the Rayleigh criterion, and since $\sin\phi = \cos\theta_1$, from how we defined the two different reference systems, the Rayleigh criterion used for evaluating mean scattering power, can be found as [23]:

$$\langle\rho\rho^*\rangle_\infty \to 1, \tag{2.49}$$

for

$$\frac{\sigma\cos\theta_1}{\lambda} \to 0. \tag{2.50}$$

Finally, in order to use the Kirchhoff theory, it is essential to understand the required assumptions used during the derivation of the theory. Here, a summarization and discussion of these assumptions are proposed.

- In equations (2.37) and (2.38) a surface with normally distributed height is assumed. Note that in [23] for other surfaces with other height distribution or for periodic surfaces, the scattering model has been discussed.

- The radius of curvature of the surface irregularities must be much greater than the wavelength. This assumption is required to approximate the field at the surface.

- At the beginning a perfect conductive surface has been assumed in order to make a, b, c in equation (2.30) constant.

- Approximate the Fresnel reflection coefficient as a constant by averaging over the entire surface area and use it in equations (2.46), (2.47) and (2.48) to compute mean scattered field, mean scattered power, and mean scattering coefficient for finite conductive surfaces.

- It is assumed that the incident wave is not bouncing between surface points in order to reach the receiver point, i.e. only one reflection is assumed.

- In this thesis, TEM waves are assumed and the mean scattered power for perpendicular polarization is discussed. However for parallel polarization also it can be found.

- It is assumed that the incident wave is a plane wave. When the emitter is far enough from the surface relative to the size of the surface area, this assumption is good.

- The original geometrical factor $F(\theta_1, \theta_2, \theta_3)$ introduced by Beckmann and Spizzichino [23] is equation (2.35). However, Vernold and Harvey [29] and Nieto-Vesperinas [30] proposed two different Geometrical factors. Vernold and Harvey [29] replace the $F^2(\theta_1, \theta_2, \theta_3)$ in $\langle \rho \rho^* \rangle_\infty$ with $\cos\theta_2$ from the Lambert's cosine law. And, Nieto-Vesperinas and Garcia [30] replace the original Beckmann-Kirchoff geometrical factor F with F_{NV}. A short description of the geometrical factor introduced by Nieto-Vesperinas [30] and Vernold and Harvey [29] is proposed in the following.

Vernold and Harvey modified geometrical factor

Vernold and Harvey [29] replace the $F^2(\theta_1, \theta_2, \theta_3)$ in $\langle \rho \rho^* \rangle_\infty$ with $\cos\theta_2$ from the Lambert's cosine law. The validity of the Modified B-K Theory was demonstrated by its authors only for large negative values of θ_2, for large incidence angles θ_1 and for scattering from infinitely conductive surfaces. It is worth noting that replacing $F^2(\theta_1, \theta_2, \theta_3)$ with $\cos\theta_2$ in the case of perfectly conductive surfaces enforces the boundaries conditions. As a matter of fact, $\cos\theta_2$ is zero in $\theta_2 = \pm 90°$ and this forces the scattering coefficient $\langle \rho \rho^* \rangle_\infty$ to be zero in $\theta_2 = \pm 90°$, i.e. on the metallic surfaces. In the current literature [31] [3] there is some confusion on this modification of the B-K Theory. Han et al. and Ragheb et al. in their articles say that Vernold and Harvey proposed to replace $F^2(\theta_1, \theta_2, \theta_3)$ with $\cos\theta_1$, but this cannot be possible since in [29] the incidence angle θ_1 is considered as fixed and, therefore, $\cos\theta_1$ is a constant. Thus, replacing the original geometrical factor $F^2(\theta_1, \theta_2, \theta_3)$ with a constant cause the loss of all the geometrical information about the scenario we are analyzing.

Nieto-Vesperinas and Garcia modified geometrical factor

Nieto-Vesperinas and Garcia [30] propose to replace the original Beckmann-Kirchoff geometrical factor F with

$$F_{NV}(\theta_1, \theta_2, \theta_3) = \frac{1 + \cos\theta_1 \cos\theta_2 - \sin\theta_1 \sin\theta_2 \cos\theta_3}{\cos\theta_2 \left(\cos\theta_1 + \cos\theta_2\right)}. \tag{2.51}$$

They claim that F_{NV} is the exact derivation of the geometrical factor, since the original F does not conserve energy between the incident and the outgoing

radiation. Moreover, note that

$$F_{NV}(\theta_1, \theta_2, \theta_3) = \frac{\cos\theta_1}{\cos\theta_2} F(\theta_1, \theta_2, \theta_3). \tag{2.52}$$

From F_{NV} it is easy to conclude that $F_{NV} \to \infty$ as $\theta_2 \to 90°$. It is also noticeable that, while

$$F(\theta_1, \theta_2 = \pm\theta_1, 0°) = \frac{1 + \cos^2\theta_1 - \sin^2\theta_1}{2\cos^2\theta_1} = 1,$$

and

$$\max_{\theta_2,\theta_3} [F(\theta_1, \theta_2, \theta_3)] = F(\theta_1, 0°, 0°) = \frac{1 + \cos\theta_1}{\cos\theta_1(1 + \cos\theta_1)} = \frac{1}{\cos\theta_1},$$

while for F_{NV} we have

$$F_{NV}(\theta_1, \theta_2 = \pm\theta_1, 0°) = \frac{1 + \cos^2\theta_2 - \sin^2\theta_2}{2\cos^2\theta_2} = 1,$$

and

$$F_{NV}(\theta_1, 0°, 0°) = \frac{1 + \cos\theta_1}{1 + \cos\theta_1} = 1.$$

Furthermore, it is worth noting that for surfaces with T_{corr} such that $k^2 (\cos\theta_1 + \cos\theta_2) T_{corr}^2 \gg 4$, the envelope exponential term $exp\left(-\frac{\left(v_x^2+v_y^2\right)L^2}{4m}\right)$ in equation (2.42) slows down the divergence introduced by F_{NV} since it prevents scattered waves at large scattering angles [30]. The derivation of $F_{NV}(\theta_1, \theta_2, \theta_3)$ is purely theoretical and in [30] there is no practical demonstration of its validity.

Chapter 3

An indoor channel model for the THz band

3.1 Introduction

Due to the increased demand for higher data rates in wireless communications, there is a tendency to use THz frequencies, which offer higher bandwidth and higher capacity. Moreover, personal communication systems (PCS), wireless local area networks (WLANs), cellular telephones, paging services, and wireless sensing devices are being deployed in indoor areas on an increasing scale. Hence, indoor communication is a vital consideration for wireless communications that involve a broad range of scenarios from inside residential or office buildings, hospitals, factories, etc. In an indoor environment, the transmitted signal most often reaches the receiver from more than one path due to the reflection by structures inside a building. The successful implementation of a wireless network requires an exact understanding of the radio propagation characteristics. As mentioned in chapter 2, THz frequencies have specific properties that need to be considered. Moreover, indoor radio channels do not suffer from environmental effects as do outdoor radio channels, for instance, snow, rain, etc. But, because of the variation of building size, shape, structure, layout of rooms, and most importantly, the type of surface materials, a unified channel model is required, particularly for THz frequencies.
This chapter attempts to address the challenges of proposing such models. Due to the variety of geometric configurations, it is impossible to represent all the structures existing in the environment accurately. Accordingly, a mathematical explanation of the problem needs to be added, taking into account various potential situations, beginning with the characterization of a surface. In the following, we first present the statistical description of the most commonly used surfaces in indoor environments. Also, we discuss different methods for generating randomly rough surfaces often used in indoor environments. Then a multi ray propagation model is proposed, which includes THz band characteristics.

3.2 Surface model

In indoor propagation, surfaces do not generate only a reflected component but rather a distribution of the reflections into different directions. It is necessary to remind that this mechanism not only depends on the frequency of an incident wave and polarization and angle of incidence but also surface characteristics. As mentioned in chapter 2 the surfaces consider rough at high frequencies, i.e., THz frequencies, compared to lower frequencies.
In general, all possible surface models can be divided into two classes: surfaces with given profiles and surfaces with random irregularities. In the first class, the detailed profile can be determined by measuring the surface's height at each point. As already mentioned, due to the variety of geometric configurations, it is impossible to describe all media and structures present in the environment accurately. Therefore, it is necessary to introduce a statistical description of rough surfaces, covering a wide range of possible scenarios. It is shown that [4, 2] most indoor communication surfaces have a height distribution that looks like a Gaussian distribution. Hence, the rough surfaces are modeled and generated by a Gaussian random process. Rough surfaces can be characterized by two parameters σ and T_{corr}, in which σ is the standard deviation of the height distribution of the surface and T_{corr} is the correlation between the heights of adjacent points. The shape of the surface is then determined by the probability distribution of heights, which is assumed to be a zero-mean Gaussian, and by the correlation length T_{corr}, which provides information about the density of the surface irregularities.

3.2.1 Standard deviation σ

The standard deviation σ is the most commonly used statistical height descriptor that shows the variations in the height of a surface, i.e. hills and valleys, relative to a reference plane. The reference plane is the mean level of the heights of the surface and is considered as zero height. Figure 3.1, shows two different surfaces with Gaussian height distribution in which each one has different $\sigma = 0.05mm$ and $\sigma = 0.25mm$. As expected, when the standard deviation of the height of a surface is small, the surface resembles a smooth surface (see Fig. 3.1a), while a larger σ leads to a rougher surface (see Fig. 3.1b). Figure 3.1c and 3.1d show the variation of the surfaces' height for two different $\sigma = 0.05mm$ and $\sigma = 0.25mm$. Note that parameter σ concerns the variation of the surface profile in the vertical direction only; it does not provide any useful information about the distance between hills and valleys of the surface, i.e., about the density of irregularities, that is described by the correlation length parameter T_{corr}, as described in the next paragraph.

3.2.2 Correlation length T_{corr}

The correlation length T_{corr} is the length over which the auto-correlation function drops a small fraction of its value at the origin. To determine T_{corr},

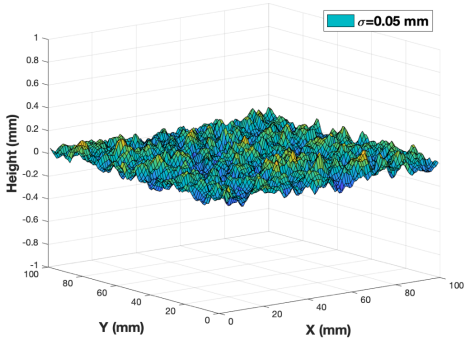

(a) Surface characterized by a Gaussian random height distribution $G(0, \sigma)$ with $\sigma = 0.05mm$.

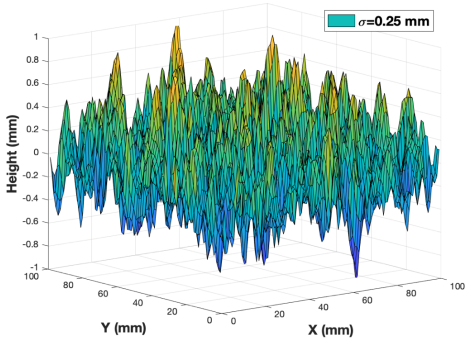

(b) Surface characterized by a Gaussian random height distribution $G(0, \sigma)$ with $\sigma = 0.25mm$

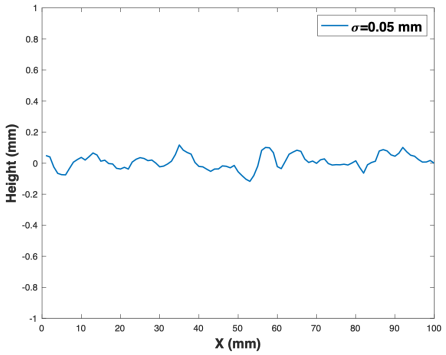

(c) Projection of a surface characterized by a Gaussian random height distribution $G(0, \sigma)$ with $\sigma = 0.05mm$.

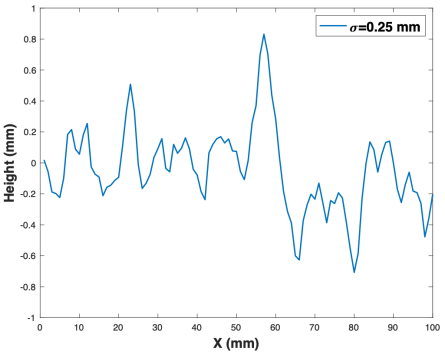

(d) Projection of a surface characterized by a Gaussian random height distribution $G(0, \sigma)$ with $\sigma = 0.25mm$.

Figure 3.1. Comparison between two surfaces with Gaussian height distributions. (a) Surface with a small $\sigma = 0.05mm$ resembles a smooth surface. (b) Surface with a large $\sigma = 0.25mm$ resembles a rough surface. (c,d) show the surfaces' projection characterized by Gaussian height distribution for $\sigma = 0.05mm$ and $\sigma = 0.25mm$, respectively. Notice that the generated random rough surfaces have the same Tcorr=2.3 mm.

the auto-correlation function coefficient $C(r)$ has to be computed first. Let the height of the rough surface be a random function of x, i.e. one dimension only $h(x)$. Two different distributions $h_1 = h(x)$ and $h_2 = h(x + r)$ are independent if they are far enough from each other with a large value of separation parameter defined by $r = |x_1 - x_2|$. Equation 2.36 defines the auto-correlation function coefficient for random surfaces. It is noteworthy to mention that the surfaces are assumed to be purely random. Therefore, $C(r)$ decreases monotonously from its maximum $C(0) = 1$, to its minimum $C(\infty) = 0$. The correlation length is defined as the value of r at which auto-correlation coefficient becomes $C(r) = e^{-1}$. Figure 3.2 shows the auto-correlation functions of two popular surfaces (plaster and wallpaper) used in indoor environments. The correlation length of 0.18 mm (see Fig. 3.2a) and 0.29 mm (see Fig. 3.2b) are found for plaster and wallpaper samples [4], respectively. Figure 3.3 shows two surfaces

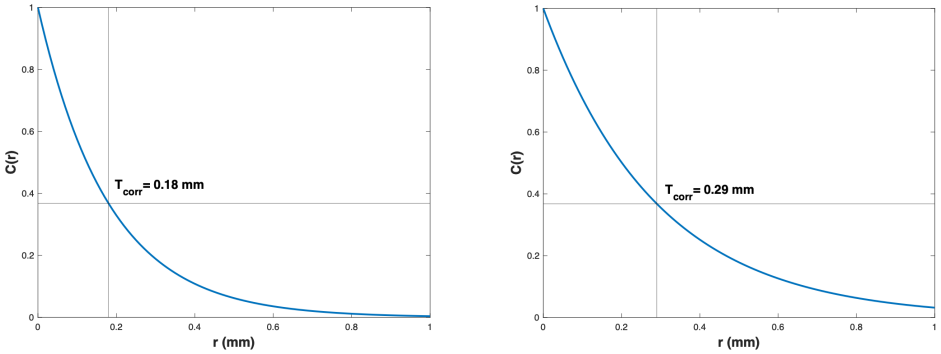

(a) **(b)**

Figure 3.2. Auto-correlation function $C(r)$ for (a) plaster and (b) wallpaper. Correaltion length T_{corr} is defined as the value of r when $C(r) = e^{-1}$, as shown on figure.

with the same height probability density function, i.e., same σ. However, the two surfaces differ. The surface in 3.3a has a small $T_{corr} = 1mm$, while $T_{corr} = 5mm$ is large for the one shown in Fig. 3.3b. If the value of T_{corr} is large, the surface does not contain many irregularities (wallpaper). In contrast, for small correlation distance, the irregularities of the surface are many and closely packed (plaster). When the correlation distance is large enough, the surface sections between irregularities can be considered smooth even if the standard deviation σ of the heights is large.

It is worth mentioning that to assume that a surface is purely random is critical. In particular, if the surface is periodic, the auto-correlation function at each period is 1, i.e. the auto-correlation function does not decrease from its maximum when $r \to 0$, to its minimum, when $r \to \infty$. Moreover, it is required to exclude the surfaces with white noise height distributions. A white noise surface as follows from its correlation function, is discontinuous everywhere and then its auto-correlation is zero at any value of separation parameter, i.e. $C(r) = 0$ for $r \neq 0$, except zero $(r = 0)$ where $C(0) = 1$.

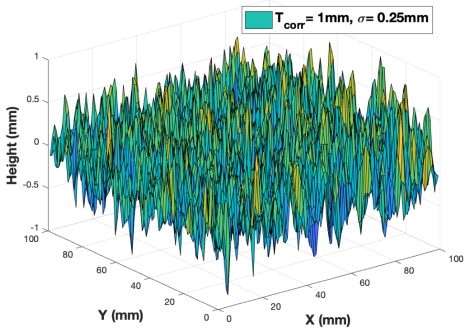

(a) Surface characterized by a Gaussian random height distribution $G(0, \sigma)$ with $\sigma = 0.25mm$ and $T_{corr} = 1mm$.

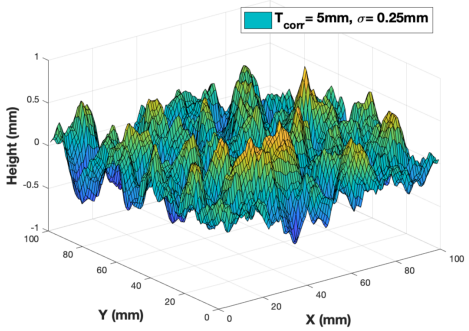

(b) Surface characterized by a Gaussian random height distribution $G(0, \sigma)$ with $\sigma = 0.25mm$ and $T_{corr} = 5mm$.

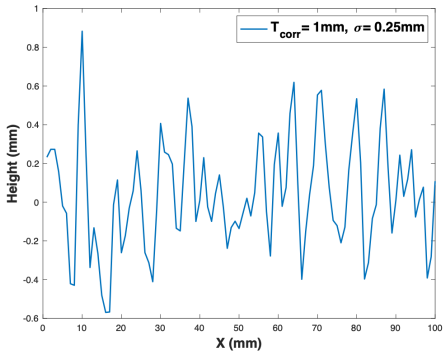

(c) Projection of a surface characterized by a Gaussian random height distribution $G(0, \sigma)$ with $\sigma = 0.25mm$ and $T_{corr} = 1mm$

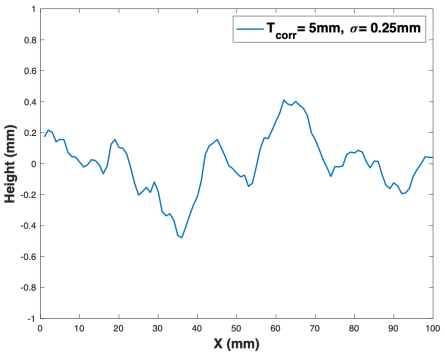

(d) Projection of a surface characterized by a Gaussian random height distribution $G(0, \sigma)$ with $\sigma = 0.25mm$ and $T_{corr} = 5mm$

Figure 3.3. Comparison between two surfaces with Gaussian height distributions. For both surfaces, $\sigma = 0.25mm$. The density of irregularities is high for a surface with small (a) $T_{corr} = 1mm$ and is low for a surface with large (b) $T_{corr} = 5mm$. (c,d) show the projection of the surfaces generated in (a,b), respectively.

3.3 Random rough surface (RRS) generator

For indoor propagation, most surfaces are considered Gaussian height distribution. In [32], it is shown that the Kirchhoff theory is a suitable approximation to find the scattering power of an RRS. To consolidate Kirchhoff's theory's results, here we generate an RRS according to the given σ and T_{corr}. Then we find the scattering power from the generated surface using the tangent plane at each generated point. This method fully describes in detail in chapter 4. This section only covers the methods of generating RRS. Note that different methods are proposed in the literature to generate numerical random rough surfaces such as the Newland method and the Hu and Tonder method, and Wu method. Newland method [33] uses FFT, Hu and Tonder [34] use finite impulse response (FIR) filters, convolution and FFT, and a modified FFT method proposed by Wu [1] to generate a RRS. Although these methods cannot guarantee that each profile of the generated surface has a correct auto-correlation function (ACF), the generated surface's average profile is very close to the given ACF. It is shown in [1] that the Wu method leads to a better result for smaller T_{corr} compare to Hu and Tander and Newlands methods.
To better understand the mentioned methods, a short description of the Hu and Tonder method and Wu method that can be used in this study is introduced in the following. It is worth to recap that in this study for one-dimension surfaces the height distribution is defined as a function of x, $h(x)$, and for two-dimension the height distribution of the surface is defined as a function of x and y, $h(x, y)$. The correlation distance T_{corr} is defined as the length at which ACF $C(r)$ falls to $exp(-1)$. The auto-correlation function of a surface height distribution for one dimension is defined as:

$$C(r_{i,j}) = exp\left(\frac{-r_{i,j}^2}{T_{corr}^2}\right), \tag{3.1}$$

where $r_{i,j}$ is defined as

$$r_{i,j} = \sqrt{x_i^2 + y_j^2},$$

in which x_i and y_j are the coordinate of the point $p_{i,j} = [x_i, y_j]$ on the surface.

3.3.1 Hu and Tonder's method

In this method, two-dimensional (2-D) Finite Impulse Response (FIR) filters are applied to an input sequence of random numbers so that the output sequence has a specific form of ACF. In other words, based on the given ACF, filter coefficients corresponding to the specific ACF are applied to achieve the expected correlation function [34]. FIR filters are an essential class of linear systems used to transform the input sequence $\{\eta(I)\}$ into an output sequence $\{z(I)\}$. For two-dimensional systems, FIR filters are defined as:

$$z(I, J) = \sum_{k=0}^{n-1} \sum_{l=0}^{m-1} \xi(k, l)\eta(I - k, J - l), \tag{3.2}$$

where $\xi(k,l)$ is the coefficient of the FIR filters. Designing digital filter means determining these coefficients. By taking the Fourier Transforms(FT) of both sides of equation (3.2) one obtains

$$Z(\omega_x,\omega_y) = H(\omega_x,\omega_y)\Xi(\omega_x,\omega_y), \tag{3.3}$$

where $\Xi(\omega_x,\omega_y)$ and $Z(\omega_x,\omega_y)$ are FT of the input sequence $\{\eta(I,J)\}$ and output sequence $\{z(I,J)\}$. $H(\omega_x,\omega_y)$ is frequency response or transfer function of the system that is

$$H(\omega_x,\omega_y) = \sum_{k=0}^{n-1}\sum_{l=0}^{m-1} \xi(k,l)e^{-jk\omega_x}e^{-jl\omega_y}. \tag{3.4}$$

Note that the coefficients $\xi(k,l)$ for the general form of digital filters can be obtained by calculating the inverse Fourier transform of a given $H(\omega_x,\omega_y)$. Once the filter coefficients are obtained, it is possible to generate a Gaussian RRS using direct convolution equation (3.2) or using FFT equation (3.3). The FFT method is more efficient than the convolution method in terms of processing speed. Therefore, this study uses the FFT method, which is briefly explained below. For more information about the convolution method and the generation of non-Gaussian RRS, see [34].
Taking into account a random number generator to generate an input sequence $\{\eta(I,J)\}$, the output sequence $\{z(I,J)\}$ corresponding to the heights of the random surface can be obtained by equation (3.2), which returns a surface with specific ACF. If the input sequence is now Gaussian distributed, the output of the system will have the same distribution, since the linear system does not change its distribution.
The purpose of this study is to generate RRS based on the given ACF given by equation (3.1). The Power Spectral Density (PSD) can be obtained by taking two-dimensional (2-D) Fast Fourier Transform (FFT) of ACF. In other words, based on the given correlation distance of the surface, one can generate the corresponding ACF and then generate the corresponding random rough surface. Suppose that $\{\eta(I,J)\}$ is an input series of Gaussian random numbers with $I = 0,...,N-1$ and $J = 0,...,M-1$ that has to be filtered by a FIR filter to generate an output sequence $\{z(I,J)\}$ with an ACF of $R_{zz}(k,l)$ with $k = 0,...,n/2-1, l = 0,...,m/2-1$. L_x and L_y are the minimum powers of 2 greater than N+n-1, M+m-1, respectively. So, it is possible to generate RRS in the frequency domain using the following procedure [34]:

- generate a new sequence $\{\eta_f(I,J)\}$, $I = 0,...,L_x-1, J = 0,...,L_y-1$, where

$$\begin{aligned} &\{\eta_f(I,J)\} = \{\eta(I,J)\}, && I = 0,...,N-1, J = 0,...,M-1 \\ &\{\eta_f(I,J)\} = 0, && I = N,...,L_x-1, J = M,...,L_y-1 \end{aligned} \tag{3.5}$$

- generate a new ACF sequence $\{R_f(I,J)\}, I = 0,...,L_x-1, J = 0,...,L_y-1$

where

$$\begin{cases} \{R_f(I,J)\} = \{R_{zz}(I,J)\}, \\ I = 0, ..., n/2-1, J = 0, ..., m/2-1 \\ \\ \{R_f(L_x - I + 1, J)\} = \{R_{zz}(I,J)\} \\ \\ \{R_f(I, L_y - J + 1)\} = \{R_{zz}(I,J)\} \\ \\ \{R_f(L_x - I + 1, L_y - J + 1)\} = \{R_{zz}(I,J)\} \\ I = 1, ..., n/2-1, J = 1, ..., m/2-1 \\ \\ \{R_f(I,J)\} = 0 \quad \text{otherwise} \end{cases} \tag{3.6}$$

- compute the two-dimensional FFT $\{\eta_f(I,J)\}$ to obtain the sequence $\{\Xi(\omega_x, \omega_y)\}, \omega_x = 0, ..., L_x - 1, \omega_y = 0, ..., L_y - 1$

- calculate the two-dimensional FFT of the new ACF, $R_f(I,J)$ to obtain a real sequence $S_{zz}(\omega_x, \omega_y), \omega_x = 0, ..., L_x - 1, \omega_y = 0, ..., L_y - 1$. Note that $S_{\eta\eta}(\omega_x, \omega_y)$ is PSD of input sequence and due to fact that the input sequence is a random series of numbers, its spectral density is constant $S_{\eta\eta}(\omega_x, \omega_y) = C$ [34, 1]. Furthermore, the relationship between $S_{\eta\eta}$ and S_{zz} for a linear system has the form of

$$S_{zz}(\omega_x, \omega_y) = |H(\omega_x, \omega_y)|^2 S_{\eta\eta}(\omega_x, \omega_y), \tag{3.7}$$

  and to generate a random surface, one should define a filter with real frequency response. Therefore to generate a real random surface, the filter coefficient must satisfy

$$\xi(k,l) = \xi(-k,l) = \xi(-k,-l) = \xi(k,-l) \tag{3.8}$$

  finally the equation (3.7) change to

$$H(\omega_x, \omega_y) = \left[\frac{S_{zz}(\omega_x, \omega_y)}{C}\right]^{1/2} \tag{3.9}$$

- compute the transfer function or frequency response of the filter $\{H(\omega_x, \omega_y)\}$ by applying equation (3.9), $\omega_x = 0, ..., L_x - 1, \omega_y = 0, ..., L_y - 1$

- compute new sequence $\{Z(\omega_x, \omega_y)\}$ with $\omega_x = 0, ..., L_x - 1, \omega_y = 0, ..., L_y - 1$ through complex product of $\{H_f(\omega_x, \omega_y)\}$ and $\{\Xi_f(\omega_x, \omega_y)\}$

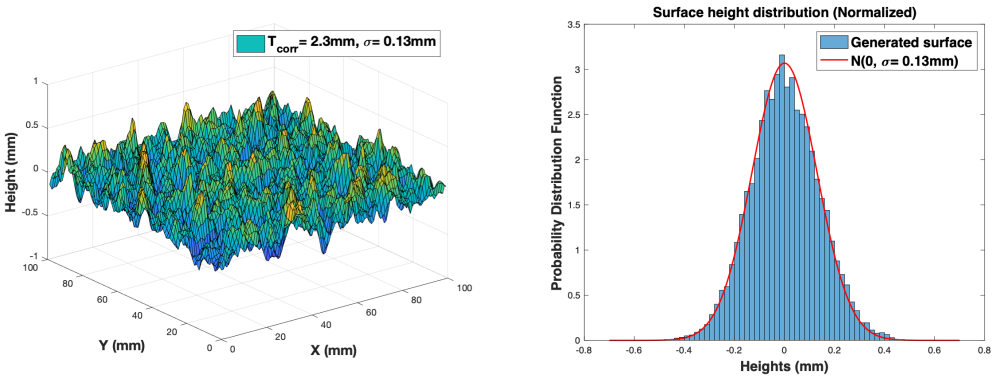

(a) (b)

Figure 3.4. An example of a surface generated by the Hu and Tonder method for $T_{corr} = 2.3mm$ and $\sigma = 0.13mm$. (a) The generated surface with Gaussian height distribution. (b) Comparing the normalized height distribution of the generated surface with N(0, $\sigma = 0.13mm$).

- calculate the two-dimensional IFFT of the new generated sequence $\{Z(\omega_x, \omega_y)\}$ to obtain the output sequence $\{z(I, J)\}, I = 0, ..., N-1, J = 0, ..., M-1$ that has the specific ACF, $R_{zz}(k, l)$.
  Figure 3.4a shows a generated surface with given $T_{corr} = 2.3mm$ and $\sigma = 0.13mm$ in which Figure 3.4b shows the normalized histogram of the height distribution of the generated surface which is well matched with the normal distributions. Note that, this figure

It is worth mentioning that in Wu method [1], a set of independent random phase angles uniformly distributed between 0 and 2π with some restriction is defined to generate real RRS with specific ACF. The difference between Wu and Newland method [33] is in defining spectral density and ACF in which in Newland method circular ACF instead of the ACF. In [1, 33], each method is fully described.

3.3.2 Wu's Method

In his article [1], Wu proposed generating random surface using the Discrete Fourier Transform (DFT) [1]. Starting from the given ACF, equation (3.1), with the dimension of $M \times N$ discrete points, we can obtain the power spectral density S by applying 2-D DFT to R. Therefore,

$$S_{k,l} = \frac{1}{MN} \sum_{r=0}^{M-1} \sum_{s=0}^{N-1} C_{r,s} e^{-j2\pi\left(\frac{kr}{M} + \frac{ls}{N}\right)}, \tag{3.10}$$

with $k = 0, 1, ..., M-1$ and $l = 0, 1, ..., N-1$. Then, we add a random phase ϕ to S. The random phases are uniformly distributed over the interval $\phi_{k,j} \in [0, 2\pi]$. In order to make the Fourier Discrete Inverse Transform real,

there is a constraint on ϕ

$$\phi_{k,l} = -\phi_{M-k,N-l}. \tag{3.11}$$

Finally, we get the random surface by inverse Fourier transforming S,

$$z_{p,q} = \sum_{k=0}^{M-1} \sum_{l=0}^{N-1} \sqrt{S_{k,l}} e^{j2\pi\left(\frac{kp}{M}+\frac{lq}{N}\right)+j\phi_{k,l}}. \tag{3.12}$$

for $p = 0, 1, ..., M-1$ and $q = 0, 1, ..., N-1$. The surfaces generated using this method have a height probability density function which is gaussian and they have the desired autocorrelation function.

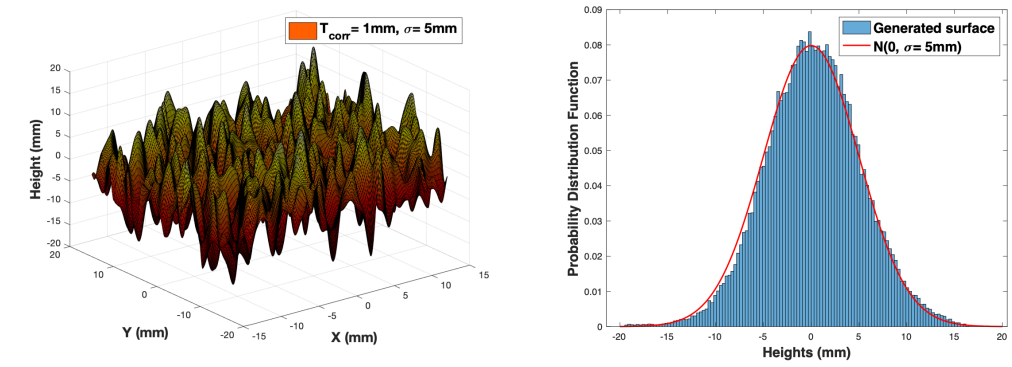

(a) **(b)**

Figure 3.5. An example of a surface generated by the Wu method [1] for $T_{corr} = 1mm$ and $\sigma = 5mm$. (a) The generated surface with Gaussian height distribution. (b) Comparing the normalized height distribution of the generated surface with N(0, $\sigma = 5mm$).

3.4 A multi-ray model for indoor THz propagation

To develop an optimal indoor wireless communication network for the THz band, a unified channel model that precisely characterizes the THz frequencies in an indoor environment is required. This section develops a multi-ray channel model for indoor THz propagation by utilizing the ray-tracing technique. In this model, the impact of free space attenuation beside the attenuation caused by molecular absorption and scattering in THz frequencies is analyzed.
Notice that the THz band is highly frequency-selective due to high propagation loss mainly because of transmission distance and the mixture of molecules along the path (see chapter 2). In the ray-tracing technique, regarding the analysis frequency, all the attenuation is computed. Since THz frequencies have strong frequency dependence and high bandwidth; hence, the frequency response can not be assumed to be constant within the entire bandwidth. One possible approach to overcome this problem is using ray-tracing at different frequencies and then combine the results [35]. This approach of dividing

frequency range has been used firstly for Ultra Wide Band (UWB) systems [36]. Before developing a multi-ray propagation model in the THz Band Here, the same approach of dividing the band into several sub-bands in the frequency domain has been applied for the THz band, as described in the next paragraph.

3.4.1 Sub-band method

The subband divided method's main goal is the combination of many individual sub-bands, which are considered narrow enough to allow us to assume flat frequency response. Then, we apply the standard ray-tracing method to find each subband's delay profile with the analysis frequency considered as the center frequency of each sub-band.
The sub-band divided method can be briefly described in the following steps [36]:

- divide the whole bandwidth into several sub-bands. Each sub-band is considered narrow enough to have constant frequency characteristics (i.e., flat frequency response).
- obtain a channel impulse response at each sub-band center frequency.
- calculate sub-band frequency response by using a Fourier Transform. Then, combine all of the frequency responses for all the sub-bands to reach complete frequency responses over THz bandwidth.
- at the end, the channel impulse response (CIR) over the entire THz bandwidth can be obtained by taking an Inverse Fourier Transform.

3.4.2 Multipath channel model

Based on the statements above, a multi-ray propagation model in THz frequencies is proposed by combining many subbands. Each sub-band has been chosen narrow enough to have a flat frequency response. In the i^{th} center frequency, the narrow-band channel impulse response can be expressed as the superposition of N_i delayed rays coming from all the walls in which the p^{th} ray experience attenuation as $a_{i,p}$. By assuming t as the time of observing of the impulse response and τ the delay of propagated ray, the CIR of the multi-ray model is given by [37]:

$$h_i(\tau, t) = \sum_{p=1}^{N_i} a_{i,p}(t)\delta(\tau - \tau_p(t)), \tag{3.13}$$

where $\tau_p(t) = \frac{d_p}{c}$ is the delay related to the p^{th} path at time t. d_p the traveling distance and c is the speed of light.
In the special case, when the location of Tx and Rx are fixed and stationary environments, i.e. when the channel is time-invariant, the time parameter can be dropped. Then, the attenuation, $a_{i,p}$, and propagation delay, $\tau_p(t)$, are

independent of time t. Therefore, by considering the fixed position of Tx and Rx and stationary environment, the linear time-invariant channel model is [37]:

$$h_i(\tau) = \sum_{p=1}^{N_i} a_{i,p}\delta(\tau - \tau_p). \tag{3.14}$$

Note that the multi-ray indoor propagation includes LOS, reflected, scattered, and diffracted paths [3]. In this study, we assume the LOS and scattered ones. The channel model can be expressed as:

$$h_i(\tau) = a_{LOS}^{(i)}\delta(\tau - \tau_{LOS})\mathbb{I}_{LOS} + \sum_{p=1}^{N_{sca}^i} a_{sca}^{i,p}\delta(\tau - \tau_p), \tag{3.15}$$

where $\mathbb{I}_{LOS}$ is an indicator function and is defined as:

$$\mathbb{I}_{LOS} = \begin{cases} 1 & \text{if there is a LOS propagation path.} \\ 0 & \text{otherwise.} \end{cases}$$

Additionally, a reasonable approach to finding an impulse response adds linear phase information to the transmittance [3]. Then the impulse response can be obtained by taking the Inverse Fourier Transform (IFT) [38]. The multipath channel frequency response that is the transfer function of eq. (3.15), is the summation of the channel transfer function of LOS path, $H_{LOS}(f)$, and the transfer function for scattering, $H_{sca}(f)$. Notice that in the i^{th} frequency sub-band, the center frequency is denoted by f_i.

LOS propagation

The LOS channel transfer function, $H_{LOS}(f)$, is made up of molecular absorption loss function H_M, and free space attenuation loss function H_{FS}, as mentioned in eq. (2.13). $H_{LOS}(f)$ can be computed as:

$$H_{LOS}(f,d) = |H_{LOS}(f,d)|\, e^{-j2\pi f \tau_{LOS}}, \tag{3.16}$$

where

$$\begin{aligned} |H_{LOS}(f,d)| &= |H_{FS}(f,d) \cdot H_M(f,d)| \\ &= [A_{FS}(f,d) \cdot A_M(f,d)]^{-\frac{1}{2}}. \end{aligned} \tag{3.17}$$

The free space transfer function can be obtained from equation (2.1) as:

$$H_{FS}(f,d) = \frac{c}{4\pi \cdot f \cdot d}, \tag{3.18}$$

and the molecular transfer function computed from equation (2.12) as:

$$H_M(f,d_l) = e^{-\frac{1}{2}\kappa(f)d}, \tag{3.19}$$

where d is the LOS distance between Tx and Rx.

NLOS propagation

In the case of NLOS propagation, the channel transfer function can be computed from Eq. equation (2.18) as:

$$H_{tot}(f,d) = \sum_{p=1}^{N} \left| H_{FS}^{p}(f,d) H_{M}^{p}(f,d) H_{sca}^{p}(f) \right| e^{-j2\pi f \tau_{NLOS}^{p}}, \tag{3.20}$$

where $d = d_1 + d_2$ is the distance between Tx and the hit point on the surface, d_1, plus the distance between Rx and the hit point, d_2. The scattering transfer function H_{sca}, can be expressed as

$$H_{sca}(f) = \gamma_{TM/TE} \cdot \rho(f) \tag{3.21}$$

where γ_{TE} and γ_{TM} are the Fresnel reflection coefficients for TE and TM waves, defined in equations (2.43) and (2.44), respectively. ρ is the Kirchhoff scattering coefficient, defined in equation (2.42). Finally, by inserting H_{FS}, H_M and H_{sca} in equation (3.20)), the total channel transfer function can be express as:

$$H_{tot}(f,d) = \sum_{p=1}^{N} H_{sca}^{p}(f) \cdot \left(\frac{c}{4\pi \cdot f \cdot d} \right) e^{-j2\pi f \tau_{sca}^{p} - \frac{1}{2}k(f)(d^{p})}, \tag{3.22}$$

where τ_{sca}^{p} is related to the delay of p^{th} received ray with respect to the LOS propagation time.
Moreover, the channel impulse response can be obtained from equation (3.14) by combining equations (2.1), (2.12) and (2.48) or IFT of equation (3.22) as:

$$\begin{aligned} h_i(\tau) = & \left| \frac{c}{4\pi \cdot f_i \cdot d} e^{-\frac{1}{2}\kappa(f_i)d} \right| \cdot \delta(\tau - \tau_{LOS}) \mathbb{I}_{LOS} + \\ & + \sum_{p=1}^{N_{sca}^{(i)}} \left| \left(\frac{c}{4\pi \cdot f_i \cdot d} e^{-\kappa(f_i)d} \right) \cdot H_{sca}^{p}(f_i) \right|_{p} \cdot \delta(\tau - \tau_{sca}^{p}). \end{aligned} \tag{3.23}$$

Figure 3.6a shows the variation of the molecular transfer function (equation (3.19)) as a function of frequency and traveling distance in an indoor environment with RH= 70 %, temperature $T = 298.55$ °K, air pressure $p = 1$ atm and $p_0 = 1$ atm, $T_0 = 273.15$ °K. Meanwhile, Fig. 3.6b shows the FS transfer function's variation as a function of traveling distance and frequency in dB. It is clear from Fig. 3.6b that for longer traveling distance, there is more attenuation, more considerable transfer function; however, it is also shown that at a higher frequency, there is more attenuation. Moreover, there are some peaks in the path loss made by molecular absorption that made three spectral windows in the range of 1 GHz and 10 THz, as depicted in Fig .3.6a. Finally, to show the impact of traveling distance, including the molecular attenuation in the different frequencies, Fig. 3.7 depicts the transfer function, path gain, in the LOS case for different distances. It is shown that there are some peaks in the path loss made by molecular absorption that made three spectral windows in the range of 1 GHz and 1 THz, as depicted in Fig .3.7.

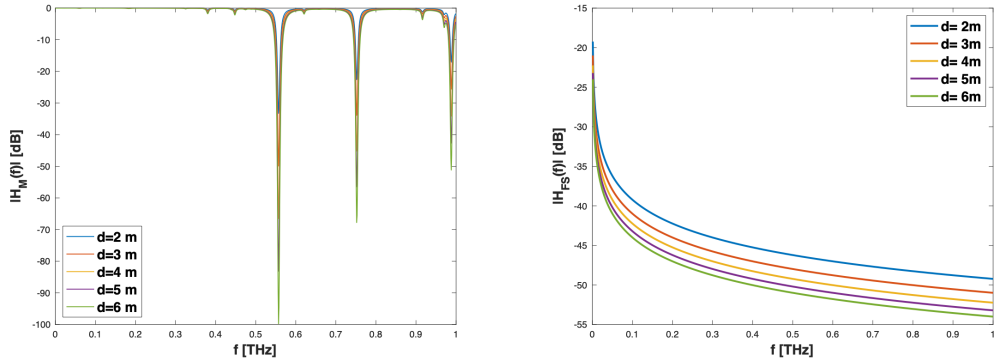

(a) (b)

Figure 3.6. (a) Molecular loss transfer function at frequency range between 1 GHz and 1 THz, with respect to the lab environment parameters, RH= 70 %, temperature $T = 298.55$ °K, air pressure $p = 1$ atm and $p_0 = 1$ atm, $T_0 = 273.15$ °K for different traveling distances. (b) FS transfer function or path gain as function of frequency and traveling distance.

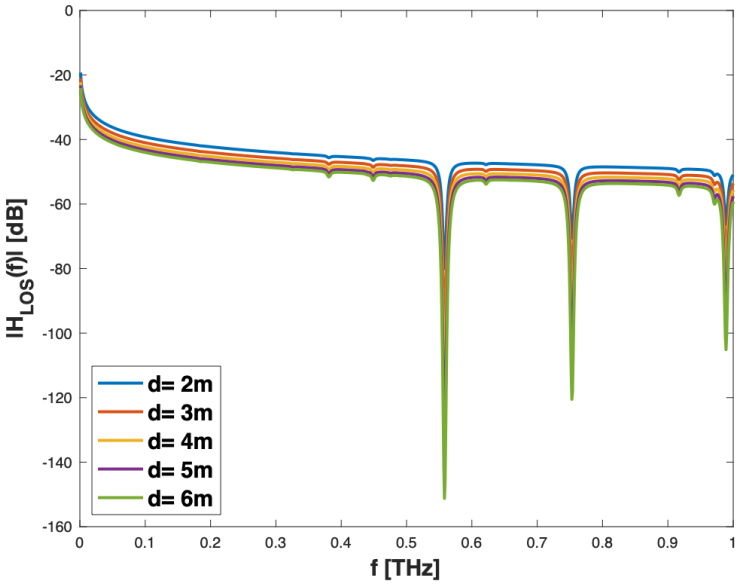

Figure 3.7. Total transfer function at frequency range between 1 GHz and 1 THz, with respect to the lab environment parameters, RH= 70 %, temperature $T = 298.55$ °K, air pressure $p = 1$ atm and $p_0 = 1$ atm, $T_0 = 273.15$ °K for different traveling distances.

Chapter 4

A Home-made ray-tracer for evaluating the propagation of THz EM waves

4.1 Introduction

The use of ray-tracing (RT) to model the propagation of radio waves in indoor environments has been of great interest in recent years [39, 40, 41, 42, 4]. Several specific propagation characteristics such as scattering and molecular absorption must be taken into account at THz frequencies. Using the ray-tracing principle, one can predict the temporal and spatial characteristics of the multipath channel with remarkable accuracy and model the effect of reflectors and scatterers with precision. Distant-dependent path loss, atmospheric models, and reflection models, such as those given in Sections 2.2.1, 2.2.2, and scattering models, such as those mentioned in Sections 2.2.4, are also easily implemented by ray-tracers.
A homemade ray-tracing simulator is proposed. The process of launching a ray from Tx at a given angle and tracing its path in a particular direction, whether or not it crosses an obstacle before the ray reaches Rx, is implemented in this simulator. Of course, due to geometry, certain rays that are launched in particular directions can not hit Rx.
As discussed in chapter 2, two parameters, i.e., g and Rayleigh criterion (equation (2.17)), can be used as a roughness factor to show the degree of roughness of the surface. Rayleigh criterion can also be written as:

$$\sigma < \frac{\lambda}{8\cos(\theta_1)}. \tag{4.1}$$

According to the surface degree of roughness, the scattering of an EM wave can be divided into two categories. When the roughness is smaller than the wavelength, the surface can be considered smooth, and the scattering phenomenon is equivalent to specular reflection from a smooth surface. In this case, the reflected wave follows Snell's law, and the magnitude of the

reflected wave can be computed by using the Fresnel reflection coefficients. However, if the surface roughness increases diffuse components appear. Hence, the reflected energy is distributed in other directions around specular direction. One popular technique used in RT models is to modify the Fresnel reflection coefficient with an attenuation factor only in the specular direction [38, 23]. This attenuation factor is based on the surface's roughness level and can be computed according to Kirchhoff's theory, by which the reflection coefficient for a rough surface for both TE and TM polarization becomes:

$$\Gamma_{TM/TE} = \gamma_{TM/TE} \cdot \rho_s, \tag{4.2}$$

where $\rho_s = e^{-g/2} \cdot \rho_0$ is the coefficient related to the specular reflection which can be written as:

$$\rho_s = exp\left[-8\left(\frac{\pi \cdot \sigma \cdot \cos\theta_1}{\lambda}\right)^2\right]. \tag{4.3}$$

The main drawback of using this modified Fresnel reflection coefficient is that it only gives the scattered field in a specular direction.
This thesis tries to present an RT-based method that takes into account scattering from rough surfaces overcoming the previous drawback. Briefly, after computing the paths of EM waves traveling between Tx and Rx, the scattering field in all possible directions after each interaction between EM waves and the environments is computed according to the Kirchhoff theory [23]. The steps involved in developing the ray-tracer framework are:

- A detailed geometrical explanation of the construction is taken into account.
- Define the building details, including the size of the room and size of obstacles in order to find different surface planes. Each surface must have its physical characteristics, such as height distribution and correlation distance. Furthermore, each surface's electromagnetic properties, such as real and complex permittivity, conductivity, and dielectric constant, are used to measure the reflection and transmission coefficients.
- Locate the position of Tx and Rx
- Compute the distance of the LOS path if it exists. In an indoor environment, signal rays coming to the receiver may be line of sight (LOS) signals and non line of sight (NLOS) signals reflected from walls, partitions, ceilings, floors, and tables, etc.
- Use image method ray tracing to compute the virtual sources. (images of Tx) and finding the reflection coefficient by applying Kirchhoff theory for NLOS rays.
- Calculate the individual contribution of each ray received at Rx.

- Calculate total E-field, received power and path loss, etc.
- Display results.

This chapter is structured as follows. First, ray-tracing methods, and more specifically, image-based ray tracing are introduced in Section 4.2. A full description of the indoor environment, including obstacles (walls), is proposed in Section 4.2.1. Furthermore, in Section 4.2.2, the way of applying the Kirchhoff theory in the ray-tracing simulator is introduced. Finally, the procedure for computing the scattered power from a rough surface using generated RRS is described in Section 4.2.3.

4.2 Ray-tracing method

A ray-tracing model uses the theory of Geometrical Optics (GO) based on the Fermat principle to deal with reflection and transmission on a surface so that signals are treated as ray propagation. The Fermat principle, also known as the shortest path principle, asserts that a ray travels between two points along the path that requires the least time than any other curve joining these two points [43]. To determine possible ray propagation between Tx and Rx, it is necessary to evaluate all the possible angles of launching rays from Tx and the angles of arriving rays at Rx. Two types of ray tracing methods are presented in the literature [44]: the brute force and the image method. The brute force method is described as follows. Tx shoots a large number of rays that are separated from each other by a small but constant angle in the 3D space. Then, by assuming an imaginary sphere of small radius around the Rx point, any ray that intersects this sphere is considered as a received ray. The brute force method requires considerable computer resources to be implemented. By the image method: it is assumed that every plane in an indoor environment to be a mirror [44]. In image-based ray tracing, the computational time is reduced, especially in simple environments, because only specular reflection paths between the Tx and Rx are considered. In this thesis, in order to analyze the indoor communications at THz frequencies, the image method is adopted. Image methods calculate specular reflection paths by considering virtual sources generated by mirroring the transmitter's location over each environment's surface. The central concept is that a direct path from each virtual source has the same condition and length as a specular reflection path. The recursive generation of virtual sources can thus model specular reflection paths up to any order. The model presented is based on the approximation that walls, floors, and ceilings are assumed to be perfectly flat surfaces along with one of the Cartesian coordinate axes. Furthermore, the rays can be ordered in terms of the number of reflections. In this thesis, the number of reflections is considered up to one reflection to help reduce the computational burden. Signal rays approaching the receiver may be line of sight (LOS) signals and reflected signals from walls, partitions, roofs, floors, tables, etc., i.e., NLOS signals in an indoor environment. For LOS propagation, it is easy to find the

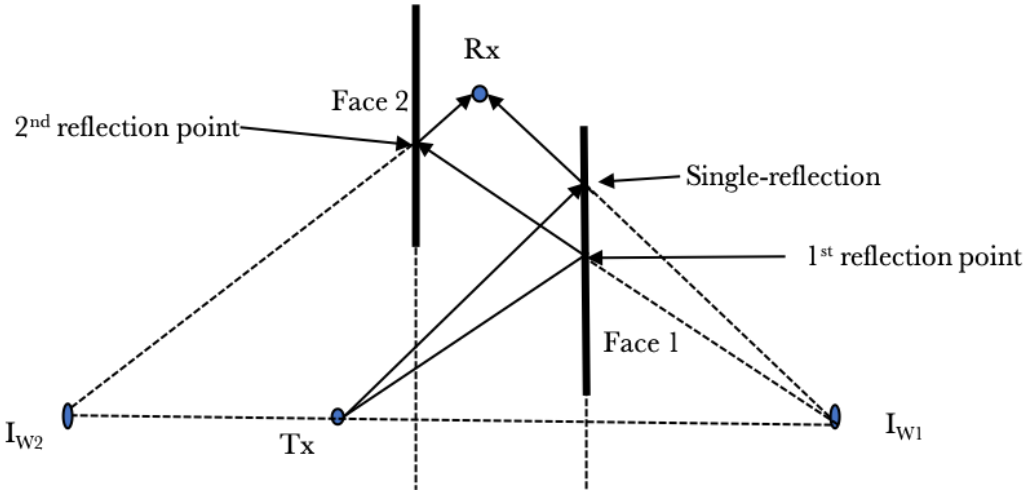

Figure 4.1. Geometrical illustration of the image method for NLOS propagation with Single-reflection and second-order reflection paths between Tx and Rx. I_{w_1} is the image of Tx with respect to Face 1, I_{w_2} is the image of I_{w_1} with respect to Face 2.

ray path by connecting the Tx and Rx positions. However, for rays reflected on the surfaces (walls) or obstacles, it is feasible to reach the Rx location from Tx by considering more than one reflection from different walls and obstacles. Figure 4.1 shows single and second-order reflections, in which a transmitted ray arrives at Rx after reflecting once or twice on different walls. Consider the single-reflection on face 1; in order to find the location of the reflection point on the wall, i.e., the specular reflection point, one can use the image method. In this method, the location of the specular reflection point is found as the intersection between face 1 and the line passing through the Tx mirrored image (I_{w_1} in Fig. 4.1) and Rx. In the case of two reflections, one first computes I_{w_1}, then in order to find the second reflection point, the mirrored image of I_{w_1} with respect to face 2 (I_{w_2} on Fig. 4.1) is computed. For multiple reflections, the same procedure is applied until reaching Rx. Note that it is also possible to find the position of the specular points by doing the reverse procedure, i.e., by moving from Rx to Tx to find the multiple-reflection path.

Figure 4.2 shows that by connecting source point (Tx), reflection (specular) point, and receiver point (Rx), the single-reflection propagation path can be obtained. The position of a specular point on the surface is defined by the source point's image regarding the surface plane, namely the Tx image. In this figure, the surface is assumed to be located on the plane z=4, hence, the Tx image can be only computed by changing the z coordinate of Tx. Moreover, the intersection of the surface plane and the vector from the Tx image to Rx shows the position of the specular point on the surface. For the rest of the scatter points, their reflection in their specular direction will not reach Rx. Furthermore, Fig. 4.2 clearly shows that the process of finding a specular reflection point on each face is reversible. It can be found by moving from Rx positions since the position of Tx, Rx, and their images are symmetric

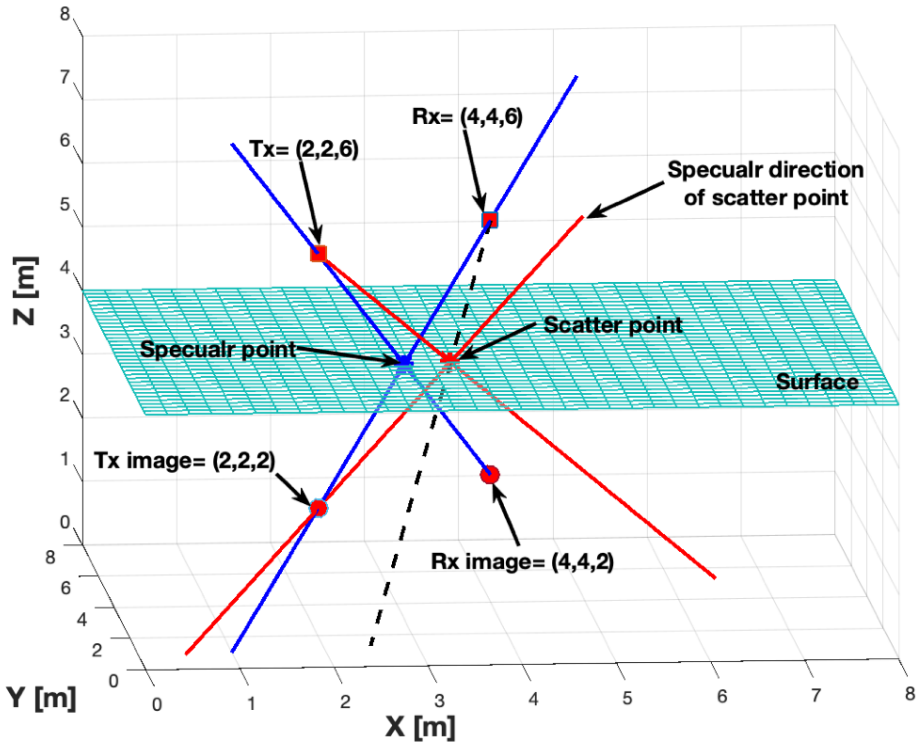

Figure 4.2. Tx image and Rx image are the transmitter Tx and receiver Rx image with respect to the surface plane z=4, respectively. Any other point on the surface, like scatter point, can not reach Rx specularly. Blue lines show the specular point on the surface. Red lines show that the reflected ray from the scatter point will not reach Rx and the dashed line indicates the line along the scattered ray deviated from its specular direction to reach Rx from the scattering point.

(located on blue lines in Fig. 4.3). Note that in the case of specular reflection, Tx, reflection point, and Rx are in the same plane, i.e., the plane of incidence and $\theta_1 = \theta_2$ as shown in Fig. 4.3. However, for the other points on the surface (scatter points), the scattered ray may reach Rx when $\theta_1 \neq \theta_2$, and there could also exist a deviation angle θ_3. This procedure of finding Tx images should be done for all walls, floor, ceiling, tables, and other considered obstacles inside a room in order to find all the reflections.

4.2.1 Environment description

Consider an isotropic transmitter in a room which is assumed to be an empty cube. The positions of Tx and Rx are fixed. As such, one ray may reach Rx directly, following the LOS path, while others may reach Rx after multiple reflections, following NLOS paths. Based on the image method, there is only one specular point on each face at which the angle of incident θ_1 and angle of reflection θ_2 are equal, and the deviation angle θ_3 is zero. Therefore, there are six specular points corresponding to the six faces of the room. Note that

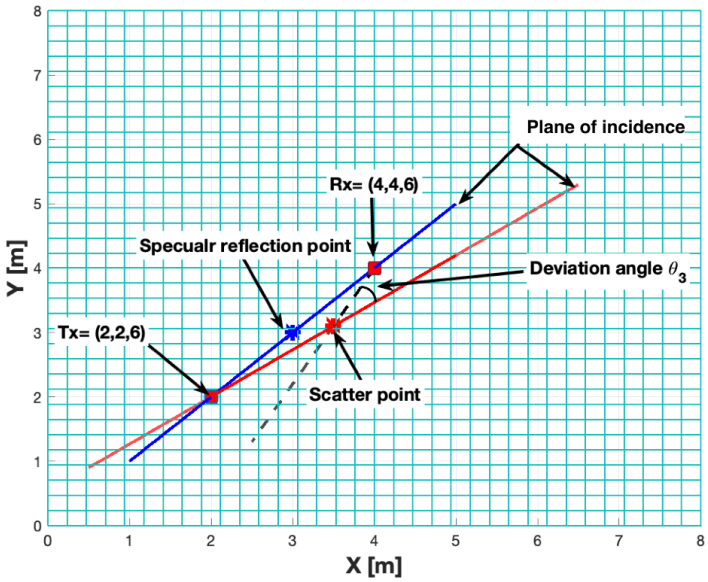

Figure 4.3. The blue line shows that the plane of incidence coincides with the plane of reflection. The red line shows the plane of incidence at the scatters point, which is not reaching Rx. The dashed line indicates the scattered plane in Rx's direction deviated from the incident plane on a scatter point by θ_3.

all of the room faces are considered to have the same properties, although it may be possible to consider different materials for each face. As a matter of fact, because of the strong attenuation due to scattering, only single-reflection paths are considered.
Figure 4.4 shows the Cartesian coordinates of Tx and Rx positions and the corresponding six specular points on the six faces. The running example room has a size of [x=8 m, y=8 m, z=8 m]. Tx's position is [x=2 m, y=3 m, z=5 m], and the position of Rx is [x=4 m, y=4 m, z=6 m]. Faces are numbered from 1 to 6 as shown in Fig. 4.5.

In the previous section, only specularly reflected rays have been determined. For ray tracing leading to reasonable results, an appropriate scattering model must be applied. The proposed ray-tracing tool implements a method based on the Kirchhoff theory for THz frequencies [23, 4].

4.2.2 Implementation method based on Kirchhoff theory

Regarding the rough surface characteristics such as its statistical parameters σ and T_{corr}, its dimensions and its dielectric parameters, eq. (2.48) provides the mean scattered power for arbitrary Tx and Rx positions. As mentioned before, in the Kirchhoff theory, the incident electric field at the rough surface is considered as a plane wave from the source. With respect to the position of Tx and Rx and their short distances from the respective surface in an indoor environment, the assumption of an incident plane wave in the Kirchhoff theory

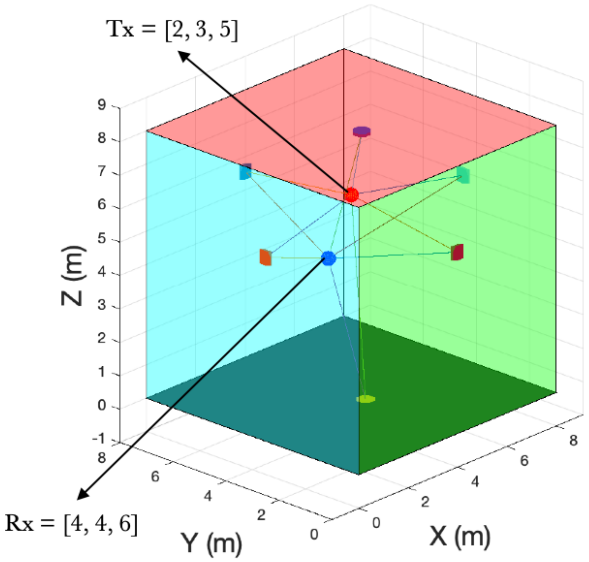

Figure 4.4. Geometry of the cubic room accompany with the position of Tx and Rx that are shown with blue and red circles respectively. The six specular points on each face are shown in different colored squares.

is only valid for a small surface area. Applying the computation only for a single scattering point on the entire surface area, e.g., one of the faces would lead to unreasonable results [45]. Therefore, instead of considering the surface area's whole, the surface is divided into $N \times M$ smaller tiles, square tiles for simplicity, as shown in Fig. 4.6 [4]. Note that separating the area into, for instance, $N \times M$ square tiles do not change the overall scattering power from the entire surface, since a single tile has a power of $\frac{1}{N \times M}$ of the overall power. Let us consider the mean scattered power in the case of $g \approx 1$, defined by equation (2.37), which is the case of most indoor building material at THz frequency. This equation can be divided into two parts:

$$S = \frac{A^2 \cos^2 \theta_1}{\lambda^2 R_0^2} \cdot e^{-g} \rho_0^2,$$

describing the specular reflection component and

$$D = \frac{\cos^2 \theta_1}{\lambda^2 R_0^2} \cdot e^{-g} \left(A \pi T_{corr}^2 F^2 \sum_{m=1}^{\infty} \frac{g^m}{m! m} e^{-\frac{\left(v_x^2 + v_y^2\right) T_{corr}^2}{4m}}, \right)$$

that is, the part related to the non-specular scattering. Note that the specular component has a quadratic dependence on the area A. Therefore, the magnitude of the specular reflection can be varied arbitrarily with the tile size. Consequently, user-defined tile sizes could potentially lead to physically unreasonable results, especially in the case of l_x and l_y large enough to make $\langle |E_2|^2 \rangle > 1$, which corresponds to a scattering gain. Note that as the illuminated surface increases, the width of the specular reflection main lobe decreases.

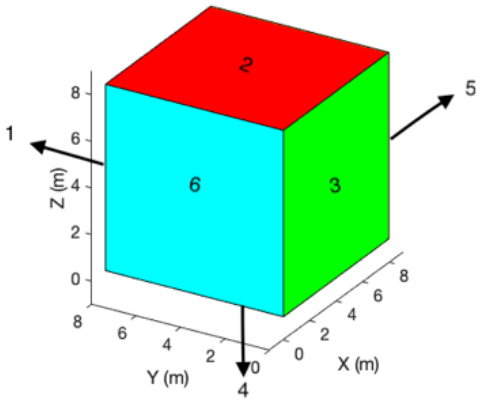

Figure 4.5. Each face of the room has been numbered from 1-6.

As an example, for $l_x = l_y = 100 \times T_{corr}$ the half power beamwidth of ρ_0^2 is 0.6°, while for $l_x = l_y = 200 \times T_{corr}$ half power beamwidth is 0.25°. This behaviour can be expected in real environments, where the illuminated areas are usually way larger than T_{corr}. Therefore, we can neglect the specular reflection component for every scattered angle θ_2 except for $\theta_1 = \theta_2$, where the amplitude of the reflected ray needs to be corrected by the Rayleigh roughness factor e^{-g}, since in $\theta_1 = \theta_2$ we have $\rho_0^2 = 1$. Furthermore, the non-specular scattering component D, is linearly dependent on the illuminated area A. Therefore, separating the whole area in j separate tiles reduces the power scattered from a single tile by a factor j, while the overall power remains constant since j separate rays of power proportional to $1/j$ are received. At THz frequencies for a typical indoor building material such as plaster, wallpaper, and gypsum, a significant amount of power is scattered around the specular point of reflection [23, 45, 4]. As mentioned in Chapter 2, when getting far from the specular direction on a rough surface, the scattered power strongly reduces [23, 45, 4]. Hence, only the relevant scatter points near the specular point are considered to minimize the computational time. Additionally, remind that only single-reflection paths are considered. Note that the scattered area around the last specular reflected point should be considered in the case of second-reflections or more.
In synthesis, only the surface area around the specular reflection point is considered and is divided into $N \times M$ smaller square tiles, as shown in Fig. 4.6. As shown in [45], increasing the size of the scattered area does not improve the accuracy due to the high attenuation of scattering from tiles that are far from specular reflection. In this thesis, due to the above effect, the values of N and M are $M = N = 11$, i.e., 121 tiles around the specularly reflected point are considered. The specular reflection point is located in the center tile.

In order to apply the Kirchhoff theory, the size of tiles l_x and l_y must be large compared to the wavelength of the incident ray. It is shown in [45] that a sufficient size for each tile is $l_x = l_y = 10 \times T_{corr}$. Figure 4.6 shows the geometry of the implemented method. Only the area around the specular

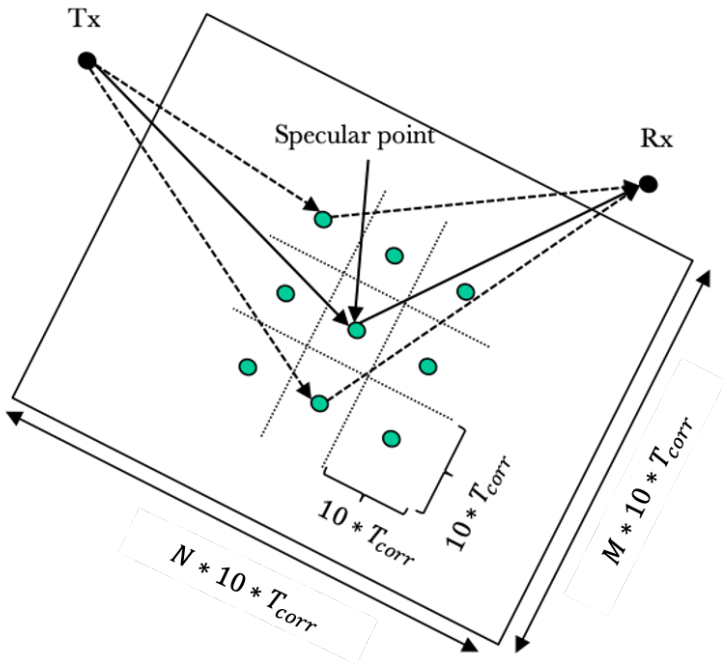

Figure 4.6. Representation of the scattering area by $M \times N$ square tiles where $M = N = 11$. All the tiles have the size with side length of $10 \times T_{corr}$ and are located around the center tile, that is the tile of the specular reflection point.

reflection point is considered. The area is divided into $M \times N$ tiles in which each tile has the side length of $10 \times T_{corr}$. The procedure is repeated for all 6 faces of the room. Totally, there are therefore 6×121 scattered rays, including 6 specularly reflected ones, that are arriving at Rx. Consider face 1, with no loss of generality, Fig. 4.7 shows the tiling of the surface related to face 1. Based on each tile's size, the distance between two center points of each tile is $10 \times T_{corr}$. Note that each tile's center point is considered for spatial calculations such as finding θ_1, θ_2 and θ_3, Time of Arrival (ToA), delay, and path length of the scattered ray.

Figure 4.8a shows all the center points of the tiles around the specularly reflecting point on face 1. Figure 4.8a also shows the intersection line between face 1 and the plane made by the three points of Tx, Rx, and the specularly reflect point on the surface. By zooming into the considered area, as shown in Fig. 4.8b, it can be seen that there are 5 points where $\theta_3 = 0$, i.e., the scattered ray lies in the plane of incidence. Remind that only one of these 5 points is related to the specular reflection point, which is the center tile where $\theta_1 = \theta_2$. A good example of this condition is depicted in Fig. 2.12, where it is shown that most of the reflected power focuses in the specular direction, while the incident and reflected waves are in the plane of incidence (see Fig. 2.8a). For the rest of the tiles, the scattered rays must be deviated out of the plane of incidence by the deviation angle θ_3 in order to reach Rx. Note that the deviation angle might be positive or negative. As shown in Fig. 4.8b, if

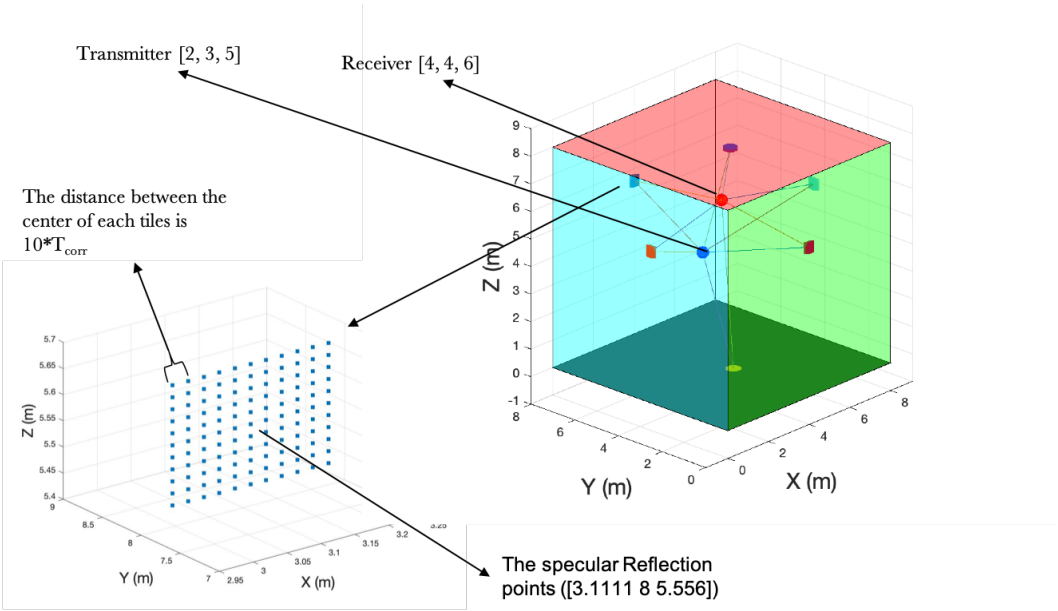

Figure 4.7. On the right side, the cubic room's geometry, TX position, RX position (with blue and red circles, respectively), and all tiles around the specular point related to the 6 faces are shown. Moreover, each square tiles' center point related to face 1 is shown on the left side of this figure. In this scenario, $M = 11$, and therefore, there are $M \times M$ tiles on each face.

the scattered ray deviates to the left side of the intersection line made by the plane of incidence to that tile and face 1, then, $\theta_3 > 0$. If it deviates to the right side, then $\theta_3 < 0$, and if a scattered ray from a tile coincides with the incidence plane, then there is no deviation and $\theta_3 = 0$.
In summary, to determine the scattered rays from surfaces, the following procedure needs to be followed. Firstly, one needs to determine the specular reflection points on each face by using the image method. Secondly, place $M \times N$ square tiles, with the same side length $10 \times T_{corr}$, around the center tile of the specular point. Thirdly, calculate related parameters such as θ_1, θ_2, θ_3, ToA, delay, and so forth. Lastly, calculate the contribution of each tile to the overall mean power reflection coefficient $\langle |E_2|^2 \rangle$.

4.2.3 Implementation method using RRS generator

This section introduces a RT-based method that computes the scattering field in the direction of Rx from the generated RRS. In this method, it is assumed that the rough surface is composed of very small smooth planes tangent to the roughness. The planes are made by three points on the surface generated by the RRS generator algorithm. The local incident angle to each plane is then computed regarding the local normal vector to that plane. Figure 4.9 shows the normal vectors of a small part of the generated surface using the Hu and Tonder algorithm mentioned in Section 3.3.1. Based on this assumption, the field reflected off each local plane can be expressed as $E_2 = \gamma E_1$. Hence

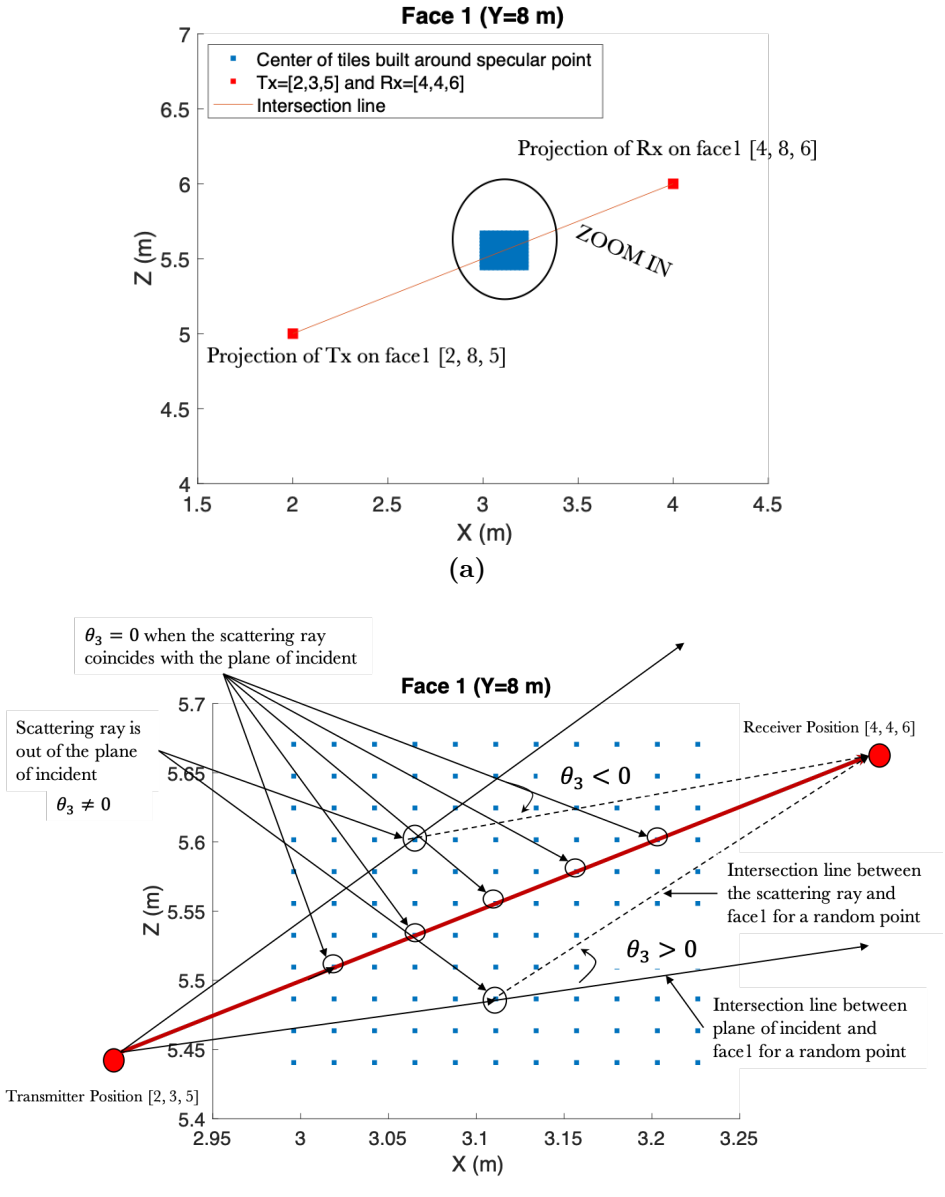

Figure 4.8. The intersection line between face 1 and the plane is made by Tx point, Rx point, and scatter point. (b) If the scattered ray's projection coincides with the projection of the incident plane on the face 1, then $\theta_3 = 0$. If the scattered ray deviates to the left side of the projection of the plane of incidence, then $\theta_3 > 0$, and if the scattered ray deviates to the right side, then $\theta_3 < 0$. There are 5 points that $\theta_3 = 0$ and for the rest, there exist a deviation angle $\theta_3 \neq 0$.

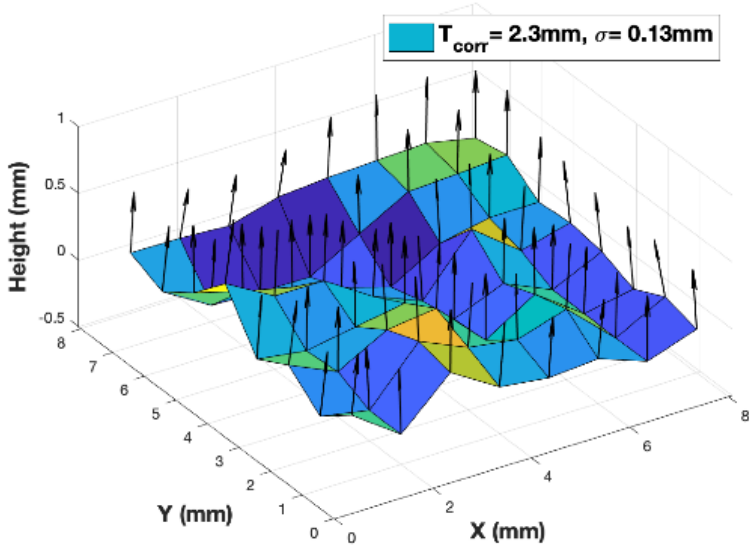

Figure 4.9. Normal vectors at each point on the surface regarding the plane at that point.

the generated surface is divided into N number of planes. It is then required to make a coherent sum of all the scattered fields' contributions with a small solid deviated angle $\Delta\theta$ from a specific direction reaching Rx. If, n out of N number of small planes direct the scattered field to Rx, then:

$$\overrightarrow{E}_2 = \sum_{i=1}^{n} \overrightarrow{E}_{2i} \tag{4.4}$$

where $\overrightarrow{E}_2$ is sum of all contributions reached Rx. Note that, the scattered field around the specific direction related to the i^{th} small plane of N total planes is

$$\overrightarrow{E}_{2i} = \frac{1}{N}\gamma\overrightarrow{E_1}. \tag{4.5}$$

In order to apply the proposed method in the considered environment, the first step is to find the specular reflection point for each faces with a given Tx and an Rx position. In the second step, the RRS needs to be centered on the specular point related to each face. Then, for each point of the generated RRS, the tangent plane at that point is computed. Consider two-dimensions scattering as shown in Fig. 4.10, θ_{1l} depicts local incidence angle respecting to the local normal vector to the local plane. Based on law of reflection $\theta_{2l} = \theta_{1l}$. In this figure, the angle between the incident ray and scattered ray reaching Rx from the point on the local surface is θ_s. Hence, if the difference between θ_s and $\theta_{2l} + \theta_{1l}$ is bigger than the defined threshold, the reflected ray is not considered as a received ray at Rx. Note that in 3-D, another angle θ_3 needs to be considered since for specular reflection, the incident ray and the scattered ray must be in the same plane.

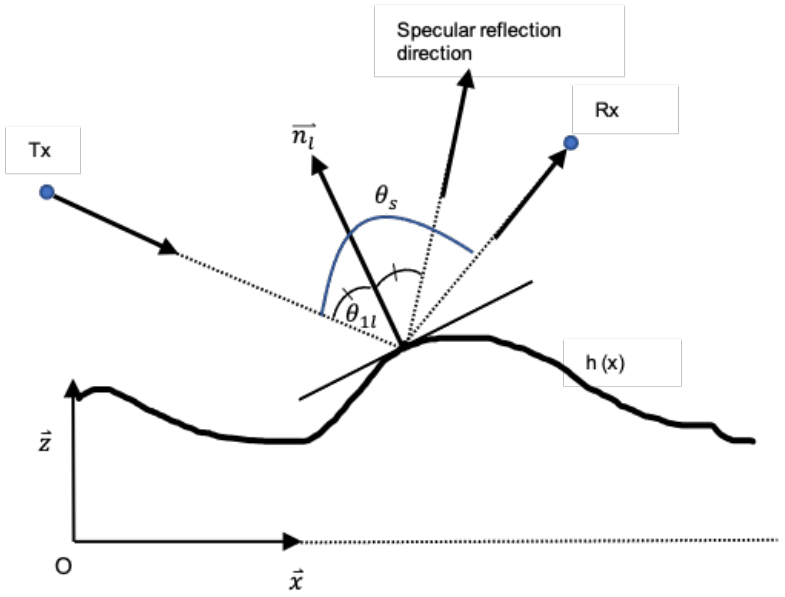

Figure 4.10. Reflection from a tangent plane at a point of the surface. θ_{1l} is local incidence angle with respect to the normal vector to the local plane $\overrightarrow{n_l}$. θ_s is the angle between incoming ray and scattered reaching Rx position.

Considering only the Fresnel reflection coefficient to compute scattered field in the specular direction from each plane E_2, could not lead to appropriate results. Therefore, to find E_2, the Fresnel reflection coefficients need to be multiplied by the Rayleigh roughness factor ρ_s, as discussed in Section 5.2. Regarding this point of view, in [46, 47], the micro-facet based model, which inherits all the assumptions and limits of the Kirchhoff theory, has been proposed. In this model, the overall scattered field is obtained by the coherent sum of all the contributions of the reflected fields encapsulated in a small solid angle $\Delta\theta$ around a specific scattered direction, which considers the interference of the possible various heights of the corresponding micro-facets [46]. However, in this thesis, we will not use this method, and one refers to [46, 47] for more information.

Chapter 5

Performance analysis

5.1 Introduction

This chapter covers the simulation results obtained by using the proposed ray tracing tool. We start by showing a comparison between the measured reflection coefficient in the specular direction (available in [2]) and the theory, for a considered material, plaster (plaster s2), that is commonly used in indoor environments in Section 5.2. Then, the influence of specific parameters such as θ_1, θ_2, θ_3, σ, T_{corr}, g, size of the room and frequency on the received power are discussed in Section 5.3. Finally, Section 5.4 analyses the power delay profile and the frequency-dependent channel impulse response (CIR) at each center frequency.

5.2 Comparison between measurements and analysis

5.2.1 Specular reflection coefficient

The measured absorption coefficient α and refractive index n of the considered material that is for example plaster, can be used to compute the specular reflection coefficient. Hence, in order to verify the validity of the computed specular reflection coefficient, one may compare these results with THz time-domain measurements performed in [2].
Figure 5.1 shows the measured refractive index n (Fig. 5.1a) and absorption coefficient α (Fig. 5.1b) of plaster (plaster s2), that is most commonly used in indoor environments [2]. Note that one can compute the Fresnel reflection coefficient for either TE or TM polarization using these measured data. Consider TE polarization, the Fresnel reflection coefficient based on either the theory γ_{TE} or approximation $\gamma_{TE,approx}$ can be computed by equation (2.43) and equation (2.45), respectively. The extinction coefficient κ_e used to compute frequency dependent complex refractive index n_c, can be expressed in terms of the absorption coefficient α as:

$$\kappa_e = \frac{\alpha \cdot c}{4 \cdot \pi \cdot f}. \tag{5.1}$$

In order to compute the reflection losses of a surface in the specular direction, the use of Fresnel reflection coefficient alone will not lead to reasonable results. The Fresnel reflection coefficients need to be multiplied in fact by the Rayleigh roughness factor $\rho_s = e^{-g/2} \cdot \rho_0$, that can also be written as $\rho_s = e^{-g/2}$ since in the specular direction $\rho_0 = 1$ (see Section 2.2.3). Therefore, the specular reflection coefficient $\Gamma^{TE/TM}$ can be computed from equation (4.2), and the approximated specular reflection coefficient for TE polarized waves can be computed as:

$$\Gamma^{TE}_{approx} = \rho_s \cdot \gamma_{TE,approx}. \tag{5.2}$$

The computed magnitude of the Fresnel reflection coefficient for TE polariza-

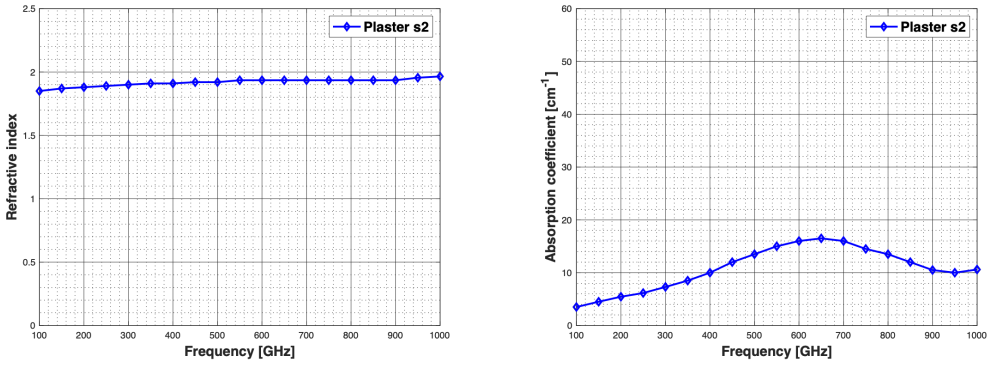

(a) **(b)**

Figure 5.1. Measurement of (a) refractive index n and (b) absorption coefficient α of plaster [2]

tion γ^{TE}, the specular reflection coefficient Γ^{TE}, as well as a direct measurement of the specular reflection coefficient for plaster [2] are shown in Fig. 5.2 for two different angles of incidence 25° (Fig. 5.2a) and 60° (Fig. 5.2b) and in frequency range between 100 GHz and 1 THz. The directly measured data are shown for the comparison between the theory and measurements. Figure 5.2 shows that the reflection coefficient computed by considering only the Fresnel reflection coefficient strongly deviates from the measured reflection coefficient in the specular direction as frequencies increase. However, there is a good agreement between the computed specular reflection coefficient based on the theory $\Gamma^{TM/TE}$ and the measured specular coefficient for plaster.

The approximated specular reflection coefficient (equation (5.2)), that is based on applying Taylor's approximation, shows good accuracy in the THz band in the case of large angles of incidence θ_1; however, for small θ_1, the accuracy decrease as shown in Fig. 5.3.

Figure 5.4 shows a comparison between the amplitude of specular reflection coefficient power computed with the approximation $(\Gamma_{approx} \cdot \Gamma^*_{approx})^{TE}$ or the theory $(\Gamma \cdot \Gamma^*)^{TE}$ (in dB). Additionally, the directly measured values for the frequency range between 100 GHz and 1 THz and two different angles of incidence 25° and 60° are also shown in this figure. Note that since we could

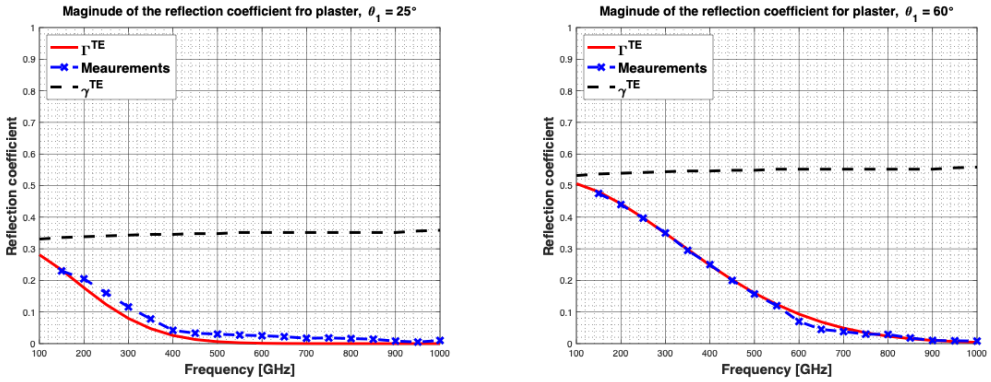

(a) (b)

Figure 5.2. The red curve shows the magnitude of the specular reflection coefficient Γ^{TE}. The dotted curve is the computed Fresnel reflection coefficient γ^{TE}, and the blue curve is the direct measurement of plaster for a frequency range between 100 GHz and 1 THz. The comparison is made for two different angles of incidence (a) $\theta_1 = 25°$ and (b) $\theta_1 = 60°$. The measured data are from [2]. Computing the reflection coefficient by considering only the Fresnel reflection coefficient strongly deviates from the measured reflection coefficient in the specular direction as frequencies increase. While the specular reflection coefficient Γ^{TE} almost fits the measurements.

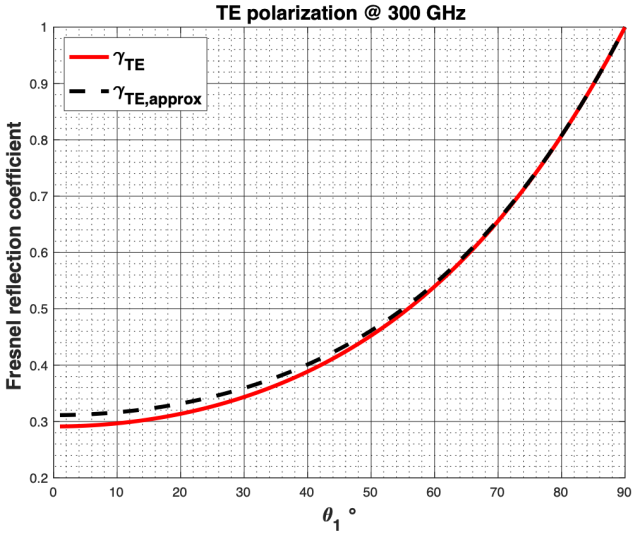

Figure 5.3. Computed Fresnel reflection coefficient for plaster at 300 GHz for TE polarization. The red curve shows the Fresnel reflection coefficient computed based on the theory γ^{TE} (equation (2.43)), and the dotted curve shows the computed Fresnel reflection coefficient regarding the approximation $\gamma^{TE,approx}$ (equation (2.45)). The curve of $\gamma^{TE,approx}$ almost fits γ^{TE} except in lower θ_1 that slightly reduce its accuracy.

not take the measured data from the authors of [2, 3], the measurement shown in this figure is obtained visually from the figures given in [2]. Especially for $\theta_1 = 25°$, the measured data for the frequencies over 500 GHz is interpolated

from [3] since it was impossible to take out the measured values from [2]. Figure 5.4 shows that the approximation and the theory are well matched. In particular, there is a good agreement between the approximation, the theory and the measured data. Furthermore, for a given angle of incidence the specular reflection coefficient power decrease by increasing frequencies. This is expected because by increasing frequency, the roughness of the material (shown by roughness factor g) increases and then scattering losses in specular direction will increase too.

Figure 5.5a shows the calculated magnitude of specular reflection coefficient

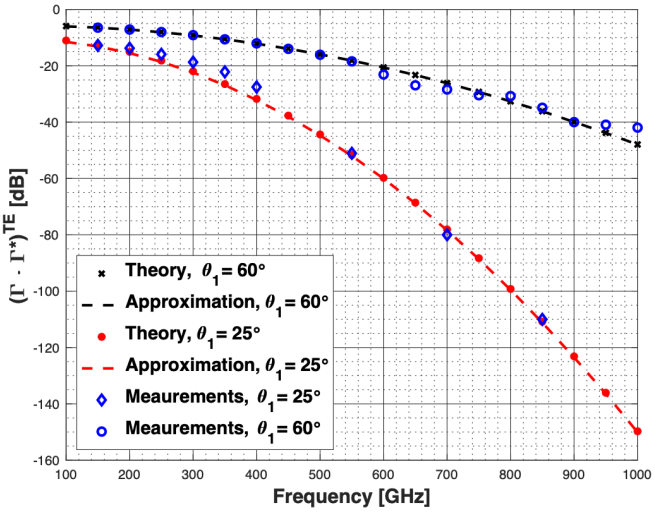

Figure 5.4. Specular reflection power coefficient for plaster based on the approximation and theory as a function of frequency for two different angles of incidence 25° and 60° in dB, measured data is from [2]

from theory and approximation as well as the directly measured values for plaster as a function of incident angle for TE polarization at the frequency of 350 GHz. A good agreement between the theory, approximation and measurements is witnessed. Moreover, the amplitude of specular reflection coefficient of power based on the approximation and theory together with the directly measured values [2] are shown in Fig. 5.5b in dB. This figure shows that the approximation and theory are well matched, and they almost coincide with the measurement. The same comparison has tried to be done in [3], but it seems to be not precise because the calculated values related to the 300 GHz are compared with the measurement at 350 GHz. Figure 5.6a depicts the comparison made by [3]. It seems that a mistake has happened since the measured data at 350 GHz is compared with the theory and approximation at the frequency of 300 GHz. Figure 5.6b shows the amplitude of the reflection coefficient regarding approximation and theory for the frequency of 300 GHz, including the measured data of 350 GHz. It can be seen from Fig. 5.6 that the proposed figure by [3] (Fig. 5.6a) is related to the frequency of 300 GHz while the measured values are for the frequency of 350 GHz. Moreover, considering

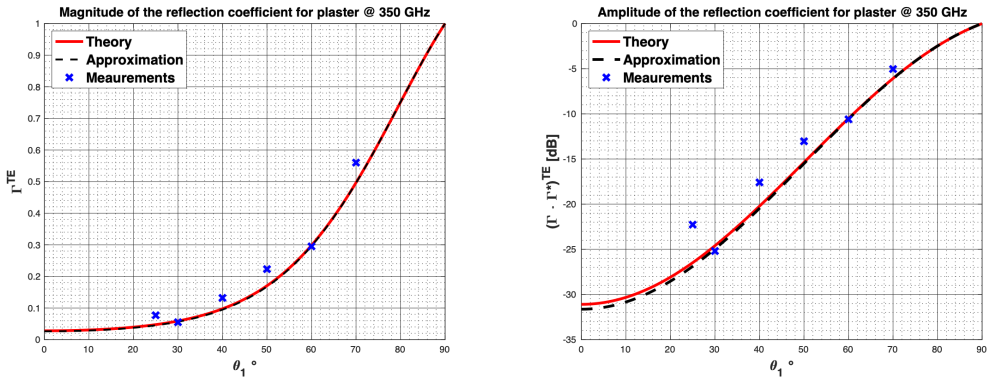

(a) **(b)**

Figure 5.5. (a) Magnitude of reflection coefficient of plaster as a function of incident angle. (b) Specular reflection coefficient power of plaster as a function of incident angle. The red curve shows the approximation, and the dotted curve is theory. The measured data is shown by 'x' and is from [2].

Fig. 5.6a and Fig. 5.6b, it seems that a mistake has happened in the measured data at $\theta_1 = 30°$ in Fig. 5.6a (proposed by [3]), regarding the measured data taken from [2] shown in Fig. 5.6b.

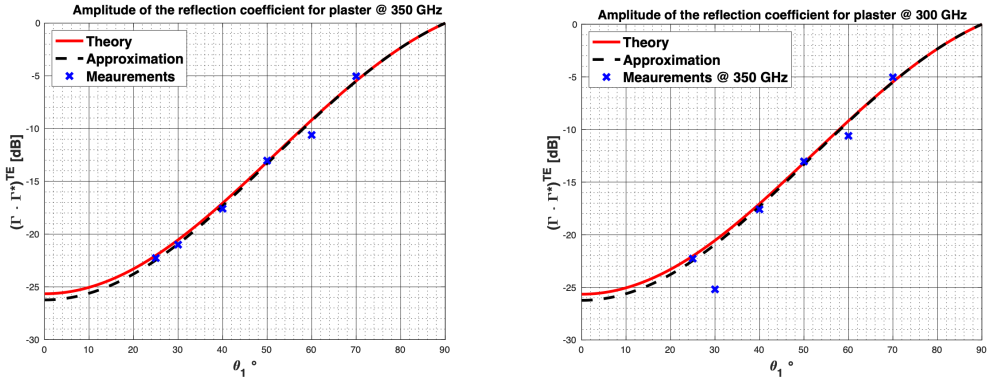

(a) **(b)**

Figure 5.6. Amplitude of the reflection coefficient of plaster as a function of incident angle. (a) The computation is performed in [3] at the frequency of 350 GHz. (b) The computation is based on the measured data taken from [2] and the proposed theory and approximation. The red curve is for theory, the dotted curve shows the approximation, and 'x' values are measured data [2]. It shows that the computation performed in [3] seems to be for the frequency of 300 GHz while the measured data are for 350 GHz. Moreover, the measured value at $\theta_1 = 30°$ seems not to be correct in (a) (the figure proposed by [3]).

Figure. 5.7 shows the specular reflection power coefficient as a function of θ_1 for different frequencies. It shows that the specular reflection loss grows either by increasing frequencies or when the incident wave tends to become

perpendicular to the surface, i.e., $\theta_1 \to 0$.

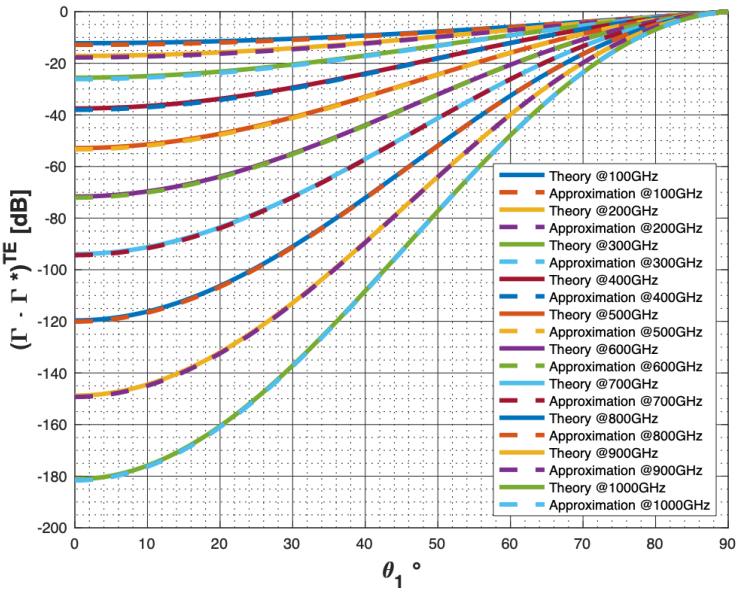

Figure 5.7. Specular reflection coefficient power of plaster as a function of incident angle for THz frequencies from 100 GHz to 1 THz.

5.2.2 Scattering coefficient

As mentioned in Section 2.2.5, the mean scattering power coefficient for a finite conductive surface $\langle \rho\rho^* \rangle_f$, can be computed by equation (2.48). Regarding Taylor's approximation, that is:

$$e^x = \sum_{n=0}^{\infty} \frac{x^n}{n!} = 1 + x + \frac{x^2}{2!} + \frac{x^3}{3!}, \tag{5.3}$$

one can approximate the e^{-g} used in computing $\langle \rho\rho^* \rangle_\infty$ (equation (2.38)) as:

$$e^{-g} = \frac{1}{1 + g + \frac{g^2}{2} + \frac{g^3}{6}}. \tag{5.4}$$

Moreover, in the case of $g \approx 1$, the series

$$\sum_{m=1}^{\infty} \frac{g^m}{m!m} e^{-\frac{\left(v_x^2 + v_y^2\right) T_{corr}^2}{4m}} \tag{5.5}$$

used to compute $\langle \rho\rho^* \rangle_\infty$, converges quickly since $1/m!m \to 0$. However, the convergence of the series depends on σ, i.e., for smaller σ it converges faster (after two terms) while for larger σ it converges after more terms as shown in Fig. 5.8. Moreover, regarding equation (2.38), the geometrical factor $F^2(\theta_1, \theta_2, \theta_3)$ has been used to represent the scattering geometrical aspect of the surface. As

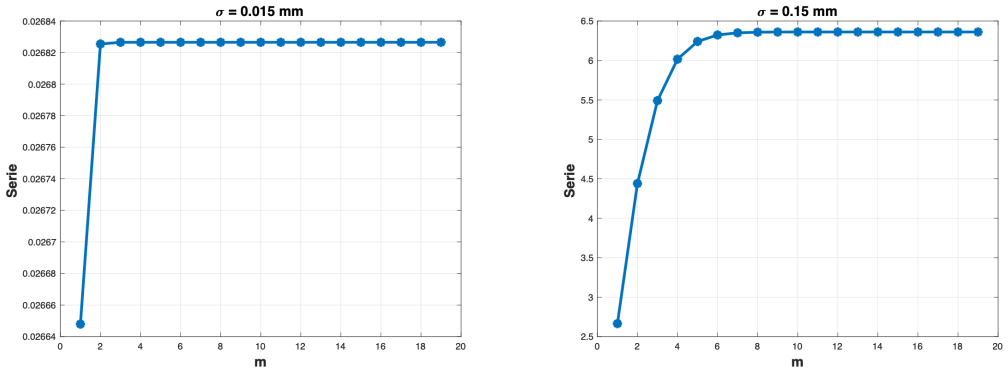

(a) (b)

Figure 5.8. Convergence of the series used computing $\langle \rho\rho^* \rangle_\infty$ when (a) $\sigma = 0.015mm$ and (b) $\sigma = 0.15mm$. For a small value of σ, the series converges fast, while for a large value of σ, the series converges after more terms.

mentioned in 2.2.5, two different geometrical factors have been proposed in the literature [29, 30] that can be replaced in equation (5.4). In [29], the F factor squared F^2 has been replaced with $cos(\theta_2)$.
Figure 5.9 shows diffuse scattering measurements carried out by [48] and compares the modified mean scattering coefficients proposed by [29] (Vernold modified theory) and the original Beckman scattering coefficient [23] (Beckman theory). Figure 5.9a compares the mean scattered power coefficient of the two models considering a small $\theta_1 = 20°$ and $\lambda = 0.633\mu m$, an area with a diameter of 20 mm, $\sigma = 2.27\mu m$, $T_{corr} = 20.9\mu m$. Results show good agreement with experimental scattering data of perfectly conductive rough surfaces, especially for large angles of incidence and scatter angles. It is shown that the measurements have a Gaussian-like distribution and are symmetric about the direction of the specular reflection. Moreover, the fit of the theories (Beckman theory and Vernold modified theory) and measurements is considerably good for small θ_1 as shown in Fig. 5.9a. Figure 5.9b shows the same comparison but for larger $\theta_1 = 70°$. It can be seen that the Vernold modified theory has better agreement with the measured data, especially for larger scattering angles where the original theory deviates more.
Note that because in our analysis only the limited region around the specular point of reflection has been considered, and following the above statements that both theories are well fitted for the measurements around the specular path, either of these theories could be applicable. Note that in these figures, the reflected angles have been shown with a negative sign.
In [3], the author applied the modified geometrical factor together with Taylor's approximation in defining the mean scattering power coefficient. Moreover, only up to the second term of the series (equation (5.5)) was considered. Furthermore, in order to find the mean scattering power coefficient for a finite conductive surface $\langle \rho\rho^* \rangle_f$, the approximated Fresnel reflection coefficient is

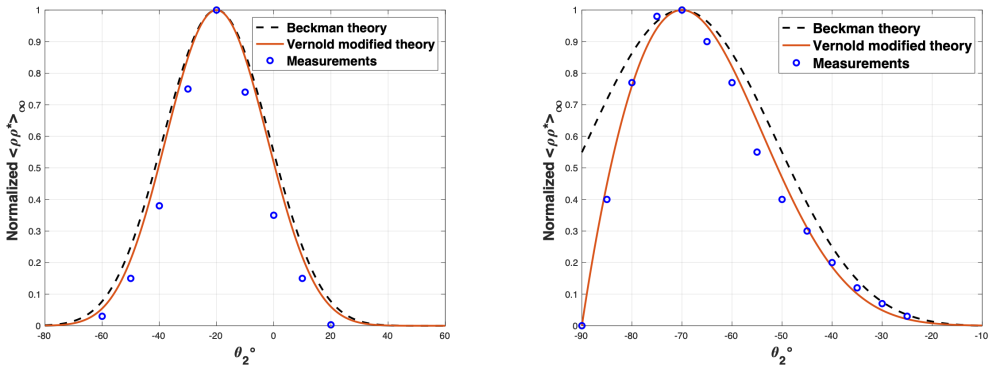

Figure 5.9. Comparison between mean scattering power coefficient considering original and modified geometrical factor for (a) small $\theta_1 = 20°$, and (b) large $\theta_1 = 70°$. In both cases $\lambda = 0.633\mu m$, scattered area's diameter is 20 mm, $\sigma = 2.27\mu m$, $T_{corr} = 20.9\mu m$.

multiplied by $\langle \rho\rho^* \rangle_\infty$. Hence, one can compute the mean scattering power coefficient as:

$$\langle \rho\rho^* \rangle_f = \left(-exp\left(\frac{-2cos(\theta_1)}{\sqrt{n_c^2 - 1}}\right) \cdot \sqrt{\frac{1}{1 + g + \frac{g^2}{2} + \frac{g^3}{6}}} \cdot \sqrt{\rho_0^2 + \frac{\pi T_{corr}^2 cos(\theta_1)}{l_x l_y}\left(ge^{-v_s} + \frac{g^2}{4}e^{-vs/2}\right)}\right)^2 \tag{5.6}$$

Figure 5.10 shows a comparison between the mean scattering power coefficient computed from the Kirchhoff (Beckman) theory and the modified one computed by equation (5.6). In this figure $< \rho\rho^* >_f$ as a function of $\theta_2 \in [0\,°,\ 90\,°]$, in steps of $0.01\,°$, for plaster s2 with a refractive index of $n_c = 2.24 - j0.025$, the correlation length of $T_{corr} = 0.18$ mm, and the height standard deviation $\sigma = 0.088mm$ is shown [4, 3]. The computation has been done at the frequency of $f = 300$ GHz over an area with a side length of $l_x = l_y = 20 \cdot T_{corr}$ when $\theta_1 = 30°$. Figure 5.10 shows a good agreement between theory and approximation around specular direction while this agreement breaks by moving far from specular reflection. The computed mean square error (MSE) for approximation is about $1.338[dB]$. Note that the MSE for the area around specular reflection, i.e. when $20° \leq \theta_2 \leq 40°$ is about $0.338[dB]$. Hence, the approximation is fitted with the theory around specular reflection.

Figure 5.11 indicates that the approximated model is acceptable since $MSE \approx 0.26[dB]$ in the THz frequency range. Moreover, by fixing the scattered angle θ_2, the scattering loss increases with the frequency non-monotonically up to 0.7 THz.

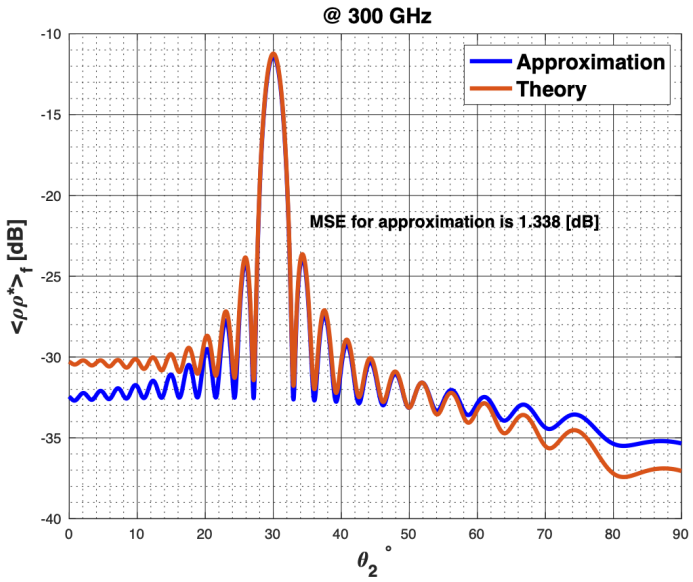

Figure 5.10. Comparing mean scattering power coefficient calculated from theory (equation (2.48)) and approximation equation (5.6) for plaster. The parameters used are [4]: refractive index $n_c = 2.24 - j0.025$, the correlation length $T_{corr} = 0.18$ mm, the height standard deviation $\sigma = 0.088mm$, $f = 300$ GHz, $\theta_1 = 30°$ and $\theta_2 \in [0\,°,\ 90\,°]$ in steps of $0.01\,°$, $l_x = l_y = 20 \cdot T_{corr}$.

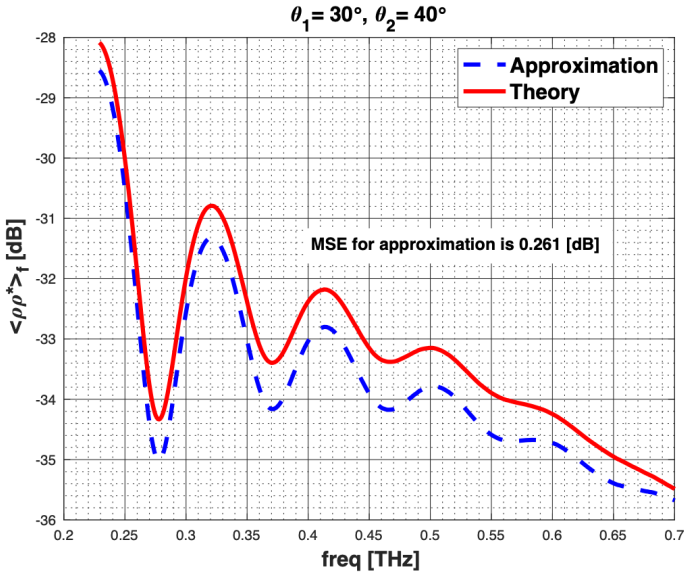

Figure 5.11. Comparing the mean scattering power coefficient calculated from theory (equation (2.48)) and approximation equation (5.6) for plaster as a function of frequency. The refractive index and absorption coefficient are from Fig. 5.1 [2], $T_{corr} = 0.18$ mm, $\sigma = 0.088mm$, $\theta_1 = 30°$ and $\theta_2 = 40°$, $l_x = l_y = 20 \cdot T_{corr}$.

5.3 Impacts of environmental parameters on diffuse scattering

The proposed ray-tracer typically considers 121 tiles around each specular reflection point on each face of the room (see chapter 4). The six faces of the room are numbered from 1-6, as illustrated in Fig. 4.5. All the faces have the same properties. The center point of each tile is considered for computing incident, scattered, and deviation angles. Remind that the Rayleigh roughness factor g was introduced as an indicator for relative surface roughness at a given frequency (see chapter 2). The Rayleigh roughness factor depends on σ, θ_1, and θ_2, as shown in equation (2.40).
Figure 5.12 shows the impact of σ on the mean scattering power coefficient for a finite conductive surface on face 1 with $T_{corr} = 2.3mm$, $n = 1.97$, $\alpha = 7.3cm^{-1}$. Two different value of $\sigma = 0.088mm$ (see Fig. 5.12a) and $\sigma = 0.25mm$ (see Fig. 5.12b) are compared. Note that we assumed an empty room with the size of [X=8 m, Y=8 m, Z=8 m] with the Tx and Rx located at Tx=[X=2 m, Y=3 m, Z=5 m] and Rx=[X=4 m, Y=4 m, Z=6 m]. Hence, all the angles $\theta_1, \theta_2, \theta_3$ are computed for each tile separately for face 1 with respect to the position of Tx and Rx. The incident angle for each tile changes around $\theta_1 \approx 13.9527°$ which is related to the center tile. It shows that when the surface is smooth, most of the reflected power is in the specular direction, center point (see Fig. 5.12a). Figure 5.12a shows that when one gets far from the specular point, the scattered power in the Rx direction from neighbor tiles reduces. However, Fig. 5.12b shows that there is no dominant reflection in the specular direction when the surface is rough. Note that in either Fig. 5.12a and Fig. 5.12b, there are five points for which $\theta_3 = 0$ ($\theta_3 = 0$ and θ_2 have 5 different values, crossed by the dashed line) but only the center tile, i.e., only the tile with $\theta_1 = \theta_2$ has the most amount of mean scattered power that is expected since for specular reflection not only $\theta_3 = 0$ but also $\theta_1 = \theta_2$.

In order to show the impact of Rayleigh roughness factor g, Fig. 5.13 shows the mean value of the relative roughness factor g for face 1 and face 2 for a given value of $\sigma = 0.088mm$. Due to the short distance between the tiles, the variation of g with face is small as shown in Fig. 5.13a and Fig. 5.13b for face 1 and face 2, respectively. However, the variation of g can be greater from one face to another with respect to Tx and Rx position since θ_1 and θ_2 change. Assuming all the faces with the same geometrical and material characteristics such as same T_{corr}, σ, and material, only Tx and Rx position impact g.
Note that in Fig. 5.12 and Fig. 5.13, the squares look distorted. This distortion is related to the position of Tx and Rx. Since the positions of Tx and Rx are not well aligned with the scattering surface in this scenario, as shown in Fig. 5.14a, moving through the tile leads to non-symmetric shapes.

Figure 5.15 compares the value of the g for all faces considering fixed position of Tx=[X=2 m, Y=3 m, Z=5 m] and two different positions of Rx=[X=4 m, Y=4 m, Z=6 m] shown in Fig. 5.15a and Rx=[X=7 m, Y=7 m, Z=1 m] shown in Fig.5.15b. Note that the dependence of scattering on g is mostly on σ and

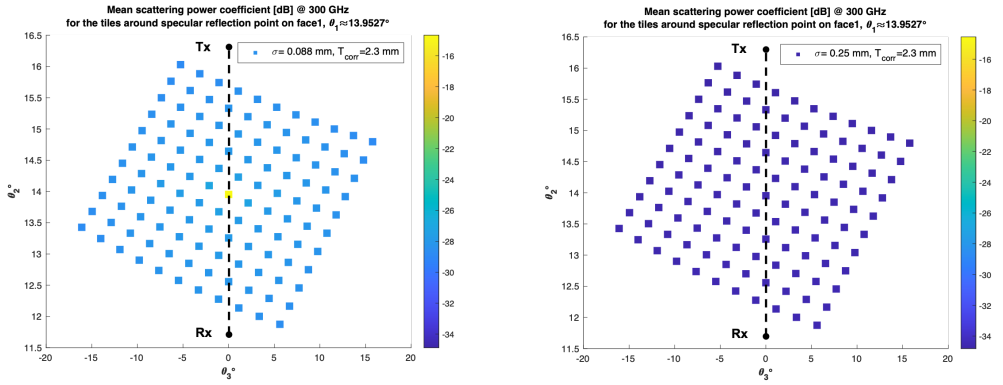

(a) **(b)**

Figure 5.12. Comparison between mean scattering power coefficient for (a) small $\sigma = 0.088mm$, and (b) large $\sigma = 0.25mm$. In both cases $T_{corr} = 2.3mm$, $n = 1.97$ and $\alpha = 7.3cm^{-1}$. All the angles $\theta_1, \theta_2, \theta_3$ are computed for each tile separately for face 1 regarding the position of Tx and Rx. For a smaller σ, i.e., smoother surface, most of the scattering power is related to the center tile. On the contrary, for larger σ, i.e., more rough surface, one faces diffuse scattering as shown in (b) specular reflection is not dominant anymore. The dashed line between shows the plane made by Tx and Rx and specualr point that is crossed with 5 tile in which $\theta_3 = 0°$.

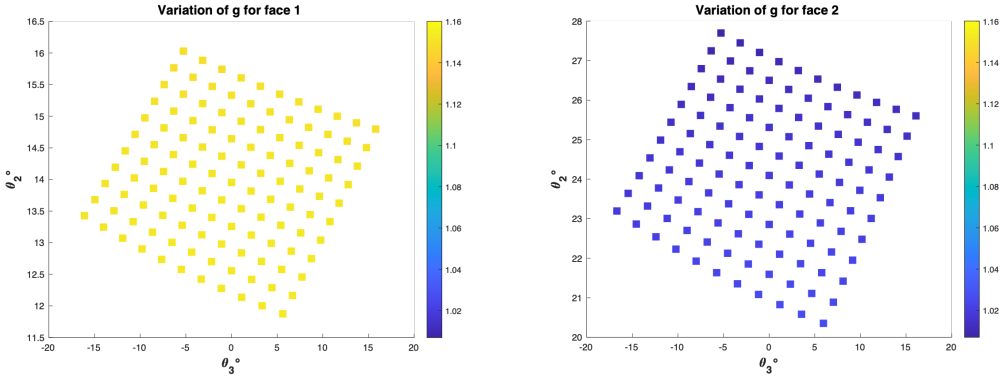

(a) **(b)**

Figure 5.13. Variation of g considering $\sigma = 0.088mm$ for (a) face 1, and (b) face 2. The variation of g is small for each face; however, this variation is larger by moving from one face to another depending on Tx and Rx's position. Moreover, the location of Tx and Rx can change the amount of g.

λ, as shown in Table 2.3. The variation of g is higher when σ has changed, as shown in Fig. 5.12, where one witnessed $g \approx 1.151$ for smaller $\sigma = 0.088mm$ and $g \approx 8.22$ for larger $\sigma = 0.25mm$.
To show the effect of the incidence angle on the scattering coefficient, all faces are shown in Fig. 5.16 (Fig. 5.16a-f are related to face 1-6, respectively). In Fig. 5.16, $\sigma = 0.088mm$ and the rest of the parameters are the same as the ones used in Fig. 5.12. Each face has a different angle of incidence with respect

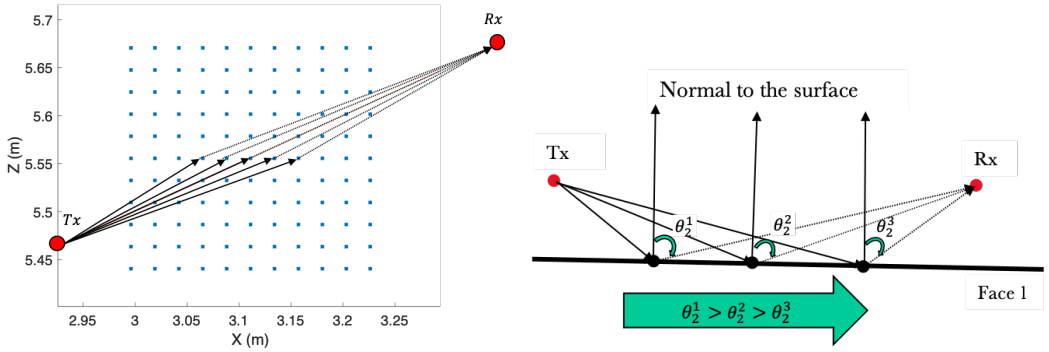

(a) (b)

Figure 5.14. The geometry of the position of Tx, Rx, and the tiles on face 1. a) Since the position of Tx and Rx are not well aligned with the scattering points on face 1 in this scenario, moving through the tile would not lead to having a symmetric shape in Fig. 5.12 and Fig. 5.13. b) Moving toward Rx, θ_2 becomes smaller.

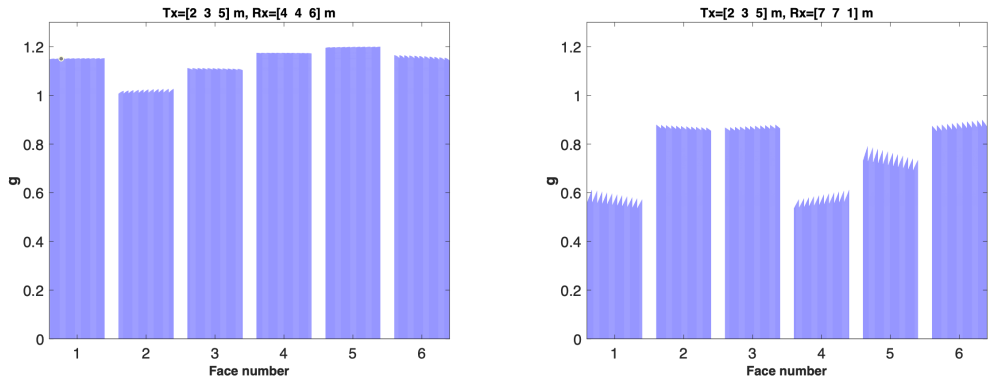

(a) (b)

Figure 5.15. Variation of g considering $\sigma = 0.088mm$ for all faces considering a fixed position of Tx and (a) Rx=[4m 4m 6m] and (b) Rx=[7m 7m 1m]. The variation of g is small for each face; however, this variation is larger when moving from one face to the other depending on the position of Tx and Rx

to the position of Tx=[X=2 m, Y=3 m, Z=5 m] and Rx=[X=4 m, Y=4 m, Z=6 m]. Most of the power is reflected in the specular direction of the center tile. Figure 5.16 shows the points located in the plane of incidence in red color. It shows that depending on the position of Tx and Rx, there could be more points that have $\theta_3 = 0$ but only specular reflection where $\theta_1 = \theta_2$ has most of the power in the case of smooth surfaces. Figure 5.16b shows that the mean scattered power reflection coefficient for the largest θ_1 is related to face 2 and Fig. 5.16e shows that the mean scattered power reflection coefficient for the smallest θ_1 is related to face 5. It is shown in Fig. 5.16 that in the case of larger θ_1, there is more attenuation due to increasing mean scattering power coefficient at the Rx.

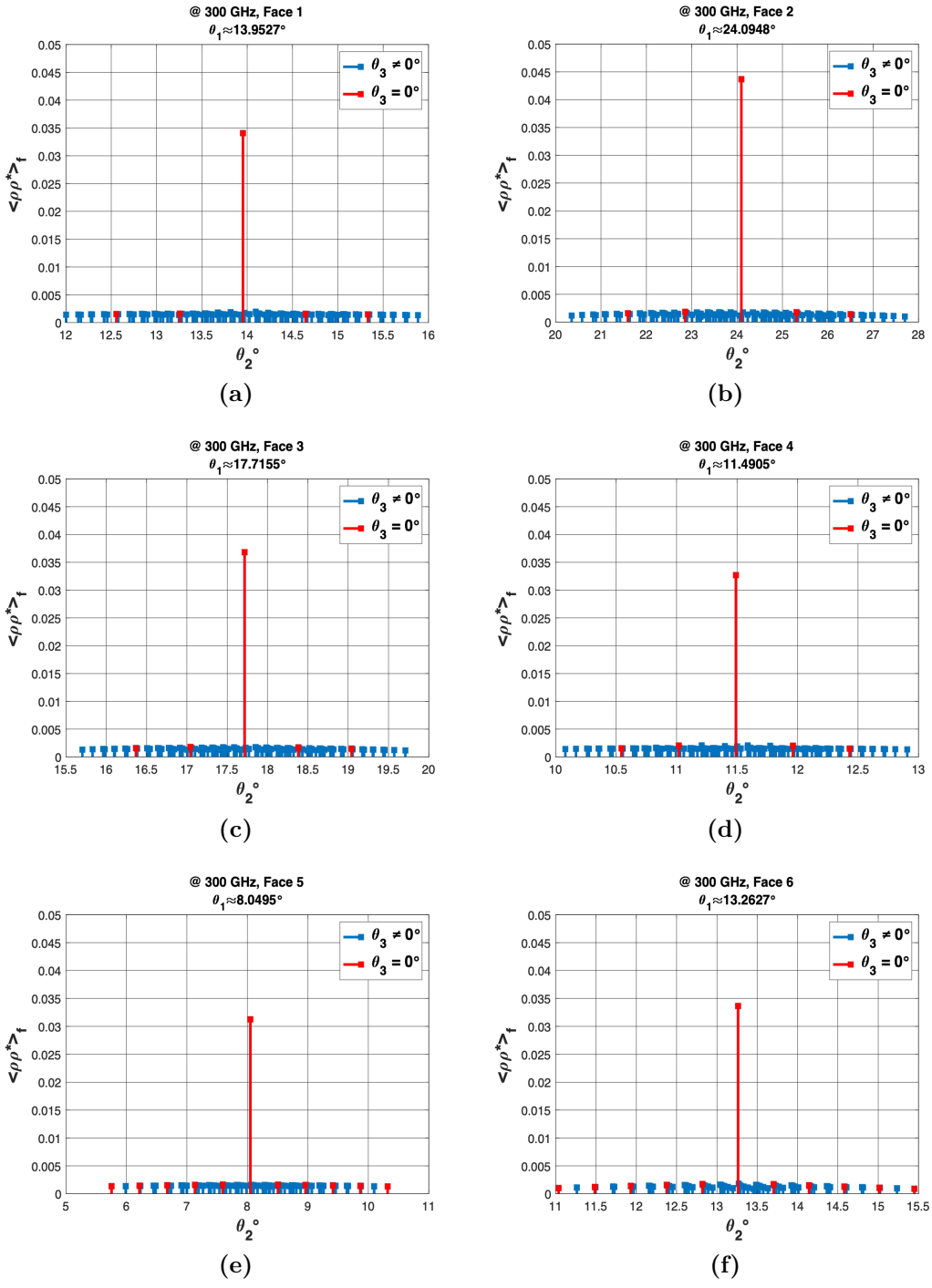

Figure 5.16. Comparison of mean scatter power coefficient for finite conductive surfaces all faces (a-f) at the frequency of 300 GHz and $\sigma = 0.088mm$, $T_{corr} = 2.3mm$. The larger θ_1, the more attenuation witnessed. The size of the room is assumed to be [8m 8m 8m] with Tx and Rx located at Tx=[2m 3m 5m] and Rx=[4m 4m 6m]. Note that θ_1 is computed for each tile separately and varies around the one related to the center tile.

5.4 Delay profile

Figure 5.17 shows how a transmitted ray (Dirac pulse)arrives at the receiver with different signal strengths as it travels through the different paths inside the room with different propagation delays. The delays are computed with respect to the LOS path. Remind that due to high scattering loss, only the first order of scattering is considered. The incoming rays can be clustered into 6 different groups related to each face; hence, regarding the assumed 121 number of tiles in each face, there are 6×121 attenuated delayed rays coming from all faces. All the incoming rays experience attenuation caused by molecular absorption and free space (discussed in chapters 2 and 3, respectively) and diffuse scattering (see equation (3.14)). Depending on the position of Tx and Rx, the incoming rays arrive in a different order. In this scenario, incoming rays from face 2 arrive first, and the rest arrive in the following order of face 6, face 3, face 1, face 5, and face 4, as shown in Fig. 5.17 The parameters used for the computation are: the room size of [X=8 m, Y=8 m, Z=8 m], Tx=[X=2 m, Y=3 m, Z=5 m], Rx=[X=4 m, Y=4 m, Z=6 m], frequency of 300 GHz, $\sigma = 0.088mm$, $T_{corr} = 2.3mm$, $n = 1.97$, $\alpha = 7.3cm^{-1}$, fixed for all faces, and humidity of $RH = 70\%$.

Figure 5.18 (a-f) shows the delay profile of each face separately. For 3ach

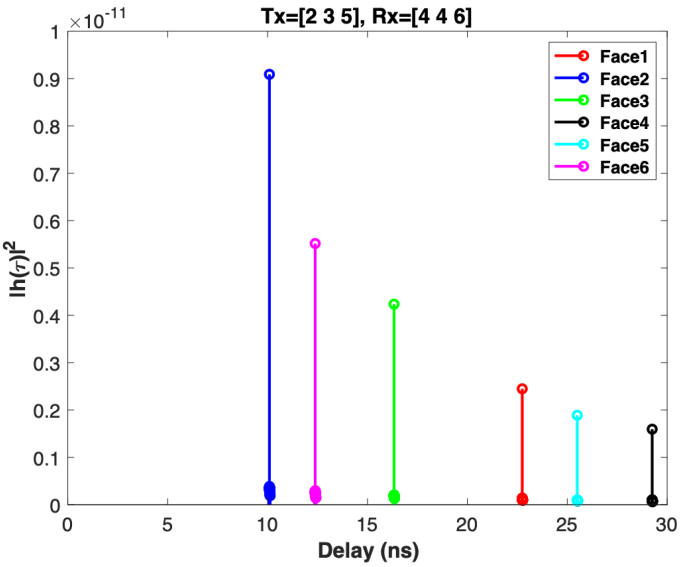

Figure 5.17. Delay profile of the attenuated received rays from all 6 considered faces. Each face is depicted in a different color. The rays arrive in 6 groups (6×121 rays) regarding each face. The first incoming ray from each face is related to the shortest path, the specular direction. The size of the room is [X=8 m, Y=8 m, Z=8 m] position of Tx=[X=2 m, Y=3 m, Z=6 m] and Rx=[X=4 m, Y=4 m, Z=6 m]. Concerning Tx and Rx's position, the incoming rays from face 2 arrive first and are followed by the rest of incoming rays from other faces with the order of face 6, face 3, face 1, face 5, and face 4.

face incoming rays arrive close to each other with a minimal delay since the distance between the tiles on each face is small. Moreover, based on the law of

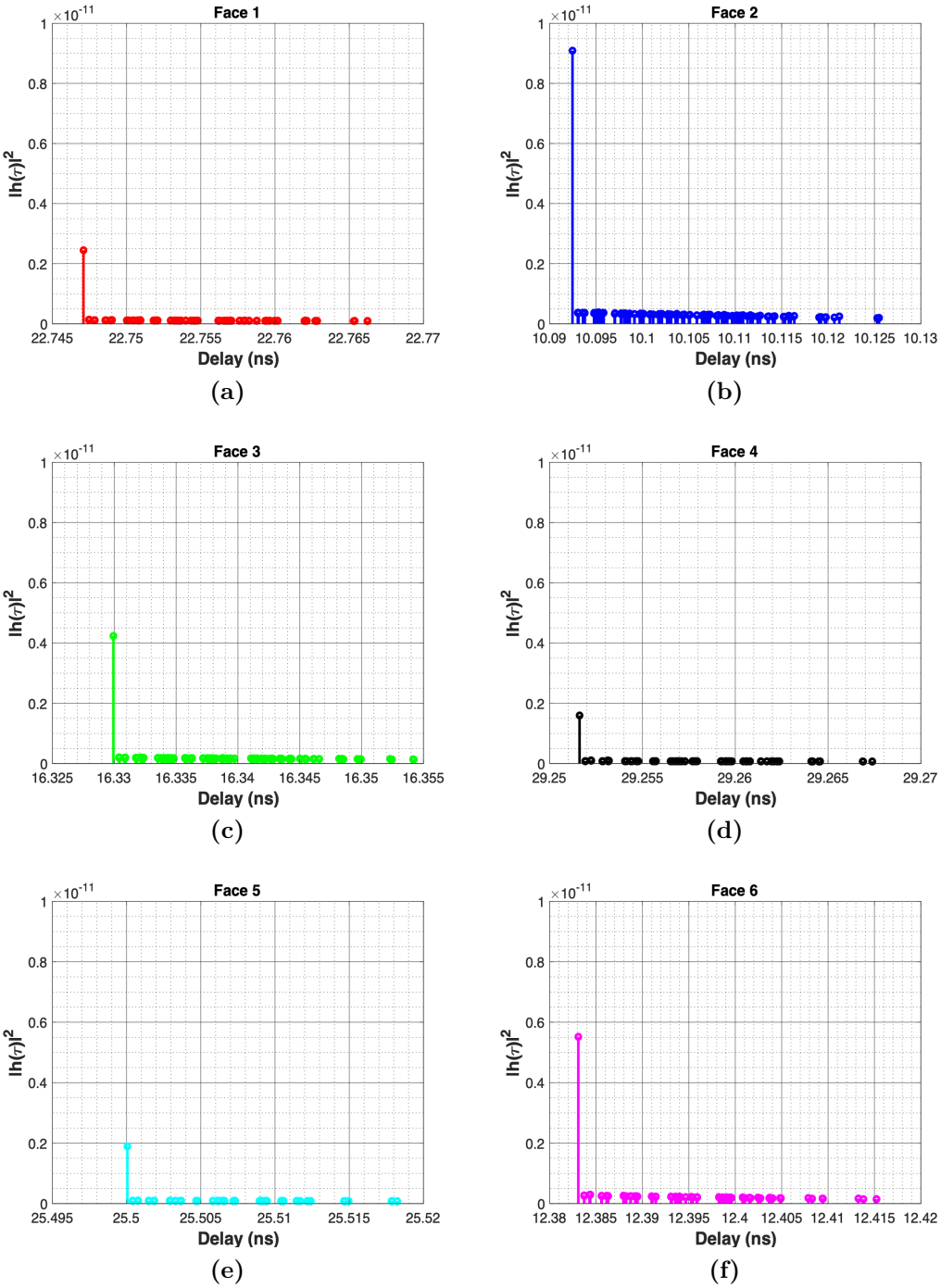

Figure 5.18. Delay profile of the attenuated rays from face 1-6 (a-f). Rays arrive in 6 groups (6×121 rays) in which rays from each face arrive in very short delays while there is a gap between rays in each face. The shortest path is related to the specular reflection in each face with the most strength in this scenario. Concerning Tx and Rx's position, the incoming rays from face 2 arrive first and are followed by the rest of incoming rays from other faces with the order of face 6, face 3, face 1, face 5, and face 4.

the reflection, the first incoming ray from each face is related to the shortest path, that is, the specular direction. In our scenario, due to the surface's characteristic, the specular direction has the most of the reflected power, as shown in Fig. 5.18 (a-f), where the first incoming ray in each face has the least delay and most power. Figure 5.18 shows that the signal attenuation highly dependent on the size of the room and the position of the Tx and Rx since the material of the faces and the humidity of the room is fixed. For instance, by changing the Rx position to the corner of the room, i.e., Rx=[7m 7m 7m], as shown in Fig. 5.19, the total received signal strength increases as traveling distance reduces, i.e., the delay reduces. Note that the incoming rays' order is also changed in which the incoming rays from face 2 arrive first and are followed by the rest of incoming rays from other faces with the order of face 1, face 5, face 6, face 3, and face 4. It shows that the lower traveling distance leads to higher signal strength at the receiver due to attenuation caused by molecular absorption and free space (discussed in section 3.4.2). However, in this scenario, since the material and geometrical characteristics of the faces are the same, scattering attenuation has less influence on the received signal than molecular absorption and free space attenuation. Figure

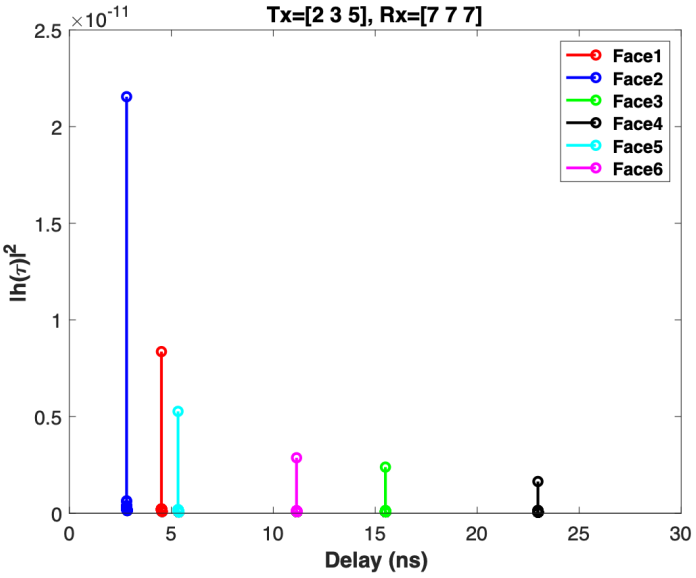

Figure 5.19. Delay profile of the attenuated received rays from all 6 considered faces. Each face is depicted in a different color. The rays arrive in 6 groups regarding each face. The first incoming ray from each face is related to the shortest path, the specular direction. The room's size and the position of Tx are the same as Fig. 5.17, but the position of Rx=[X=7 m, Y=7 m, Z=7 m]. Moving Rx's position from the center to the corner leads to shorter traveling distance (smaller delay) and lower attenuation. The order of incoming rays are also changed in which the incoming rays from face 2 arrive first and are followed by the rest of incoming rays from other faces with the order of face 1, face 5, face 6, face 3, and face 4.

5.20 compares the two computed Rx position delays as a function of scatter

points. It shows that, in this scenario, for the given Tx position moving Rx from the center to the corner of the room increases the received signal strength.

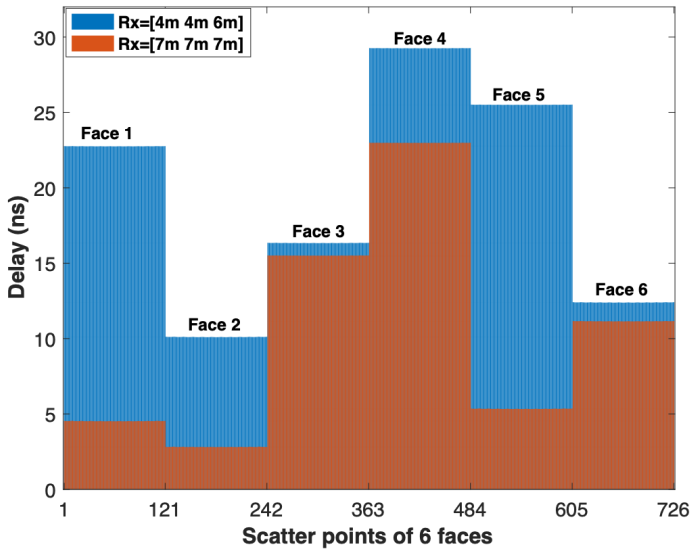

Figure 5.20. A comparison between two different positions of Rx; Rx almost in the center of the room, Rx=[X=4 m, Y=4 m, Z=6 m], the delays are larger while by moving Rx to the corner of the room Rx=[X=7 m, Y=7 m, Z=7 m] smaller delays are witnessed.

5.5 Transfer function

Remind that not only the mean scattering power coefficient but also molecular absorption and free space attenuation, i.e., path loss, are computed according to the frequency of the incident ray. The total attenuation has a strong dependency on frequency. Path loss peaks are produced because of the molecular absorption effect, and the spectral windows between these peaks are examined, as shown in Fig. 5.21. It is possible to identify three spectral windows between 0.001 THz and 1 THz, which are 0.001–0.54 THz, 0.57–0.74 THz, and 0.76–0.97 THz, respectively. The relation between the path gain and the center frequency shows that increased frequency leads to channel path gain drop. The relation between distance and path gain is strong, especially for short distances, as shown in Fig. 5.21. For example, for a traveling distance of 6m, only the frequency bands (0.06–0.54 THz) and (0.58–0.73 THz) have path loss values below 100 dB. I.e., longer traveling distances cause a reduction in the availability of spectrum for communication. Since THz frequencies have strong frequency dependence and high bandwidth, the frequency response cannot be assumed to be constant within the entire bandwidth. If a wireless system bandwidth is considered narrow enough, the frequency response depends of frequency can be disregarded. To overcome this problem, one can use ray-tracing at different frequencies and

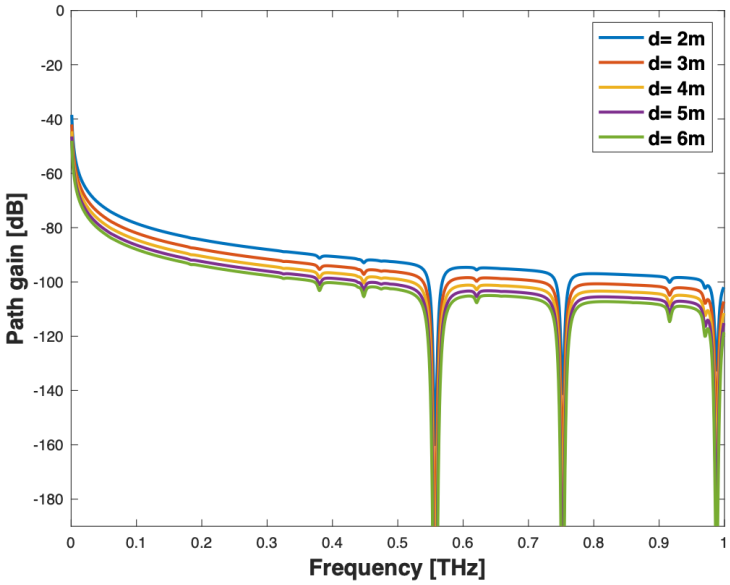

Figure 5.21. Path gain for frequency range between 1 GHz and 1 THz, with respect to the lab environment parameters, RH= 70 %, temperature $T = 298.55$ °K, air pressure $p = 1$ atm and $p_0 = 1$ atm, $T_0 = 273.15$ °K for different traveling distances.

then combine results (see section 3.4.2). To do so, first, one needs to break the bandwidth into many sub-bands, which are considered narrow enough to allow us to assume flat frequency response [36]. For each sub-band, one uses the ray-tracing approach to obtain the delay profiles considering each sub-band's center frequency. Note that each delay profile can be different even for the same propagation direction due to the frequency dependency of the materials. These delay profiles are then transformed into frequency responses (using FFT) that can only be accurate around each sub-bands center frequency. These accurate parts of each frequency response are extracted and then combined to obtain a new frequency response. Finally, to get a delay profile that is accurate over the entire THz band, the response is transformed into the time domain [36].
The complete frequency response can be expressed mathematically as:

$$H(f) = \sum_{i=1}^{I} \mathcal{F}\{h_i(\tau)\} \cdot R_i(f), \tag{5.7}$$

where i is the sub-band index, and I is the total number of sub-bands, $\mathcal{F}\{\cdot\}$ is the Fourier transform, and $h_i(\tau)$ is the CIR at the i^{th} sub-band (center frequency) that can compute by equation (3.14). $R_i(f)$ is the rectangular window function associated with the i^{th} frequency. Hence, the channel impulse responses (CIR) are generated at multiple center frequencies f_i instead of only at one frequency. Then, from each sub-band CIR, the channel transfer functions (CTF) are computed and concatenated in the frequency domain to

obtain the complete CTS, as shown in equation (5.7). Finally, the overall CIR $h(\tau)$ can then be obtained through the inverse Fourier transform (IFFT) as:

$$h(\tau) = \mathcal{F}^{-1}\left\{\sum_{i=1}^{I} \mathcal{F}\{h_i(\tau)\} \cdot R_i(f)\right\}. \tag{5.8}$$

Figure 5.22 shows the CIR considering only the incoming rays from face 1 (see Fig. 5.22a). The time axis is divided into small intervals called 'bins'. Each bin is assumed to contain either one multipath component or no multipath component. To be able to apply FFT, the delay values are rounded to $10^{-16}s$, i.e., the step size is $dt = 10^{-16}s$, as shown in Fig. 5.22b. Note that the parameters used for the computation for the rest of this section are: the room size of [X=8 m, Y=8 m, Z=8 m], Tx=[X=2 m, Y=3 m, Z=5 m], Rx=[X=4 m, Y=4 m, Z=6 m], $\sigma = 0.088mm$, $T_{corr} = 2.3mm$, humidity of $RH = 70\%$, and n and α are taken from [2] for different frequencies. Using this model, each

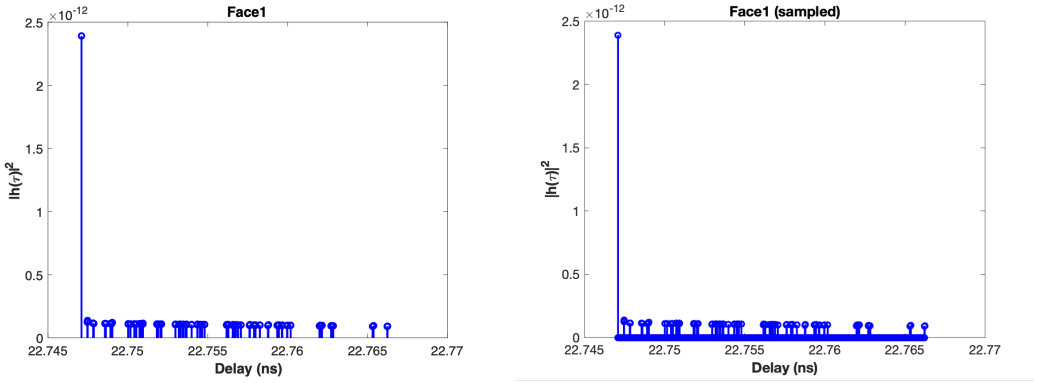

(a) **(b)**

Figure 5.22. a) The CIR of channel considering only incoming rays from face 1. b) Dividing the time axis into the bins, each bin contains either one multipath component or no multipath component. The center frequency is 300 GHz and $\sigma = 0.088mm$, $T_{corr} = 2.3mm$. The size of the room is assumed to be [8m 8m 8m] with Tx and Rx located at Tx=[2m 3m 5m] and Rx=[4m 4m 6m]. The sampling step is $10^{-16}s$.

impulse response can be described by a sequence of "0"s and "1"s. To each "1," an amplitude regarding $|h(\tau)|^2$ is associated (see Fig. 5.22b). In the next step, the FFT of the $h(\tau)$ at the given frequency is computed and is multiplied by the bandpass filter $R_f(f)$ with a bandwidth of 1 GHz. Figure 5.23a shows a digital bandpass filter at 300 GHz. The applied equiripple bandpass filter has a first stopband frequency 299 GHz, a first passband frequency 299.5 GHz, a second passband frequency 300.5 GHz, a second stopband frequency 301 GHz, and first and second stopband attenuation of 0.001. Figure 5.23b show this filter in more detail. It shows that only the frequencies between 299.5 GHz and 300.5 GHz remain almost constant, and the rest of the frequencies are attenuated. Figure 5.24a shows the convolution results between the bandpass filter and the input CIR in the time domain. One expects only the magnitude

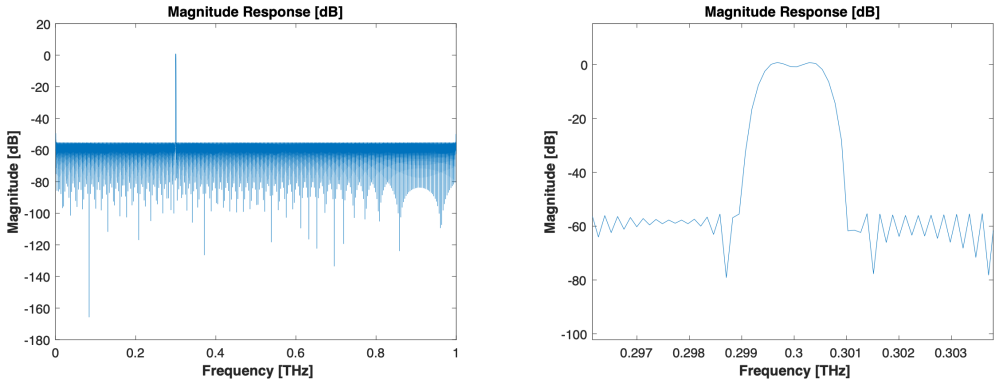

(a) (b)

Figure 5.23. A digital equiripple bandpass filter at 300 GHz with a passband of 1 GHz. a) Shows the filter for all frequencies while in (b) only the frequencies around the center frequency of 300 GHz is shown. The filter keeps the frequencies between 299.5 GHz and 300.5 GHz almost constant, and the rest of the frequencies are attenuated. However, there is a transition part between 299 GHz to 299.5 GHz and 300.5 GHz and 301 GHz, which depends on the utilized filter type. The filter has a first stopband frequency 299 GHz, a first passband frequency 299.5 GHz, a second passband frequency 300.5 GHz, a second stopband frequency 301 GHz, and first and second stopband attenuation of 0.001.

at the frequency band extracted in the considered frequency domain, as shown in Fig. 5.24b. In order to show better the filtering operation, Fig. 5.24c shows the passband frequencies around the considered center frequency. It shows that there is a small transition part from 299 to 299.5 GHz and from 300.5 GHz to 301 GHz that varies based on the type and order of the utilized filter. Note that, considering the frequency band of 1 GHz around the center frequency of 300 GHz, i.e., from 299.5 GHz to 300.5 GHz, concatenating other center frequencies could lead to having interference at the border of each frequency. However, an ideal rectangular filter is applied in Fig. 5.25a. The cutoff frequencies are exactly 299.5 GHz and 300.5 GHz, and the bandpass filtered time series and the magnitude response of the filtered time series are shown in Fig. 5.25b and Fig. 5.25c, respectively. Doing previous steps for different center frequencies and concatenating all the frequency responses lead to full frequency response. Finally, taking the IFFT of the full frequency response returns the CIR of the channel.

A different approach is to simulate the channel in the frequency domain. This is done by applying ray tracing for I_i different frequencies with equal frequency spacing of $^{Bandwidth}/_{I_i}$ over the bandwidth of the interest. The total CTF can br computed by equation (3.22), and the CIR of the channel can be calculated by IFT of $H_{tot}(f, d)$ as equation (3.23). Note that in equation (3.22), a linear phase component is determined by the time shift and the frequency, i.e., the phase component is set by $exp(-j2\pi f\tau)$. Figure 5.26 shows the CTF computed by equation (3.23).

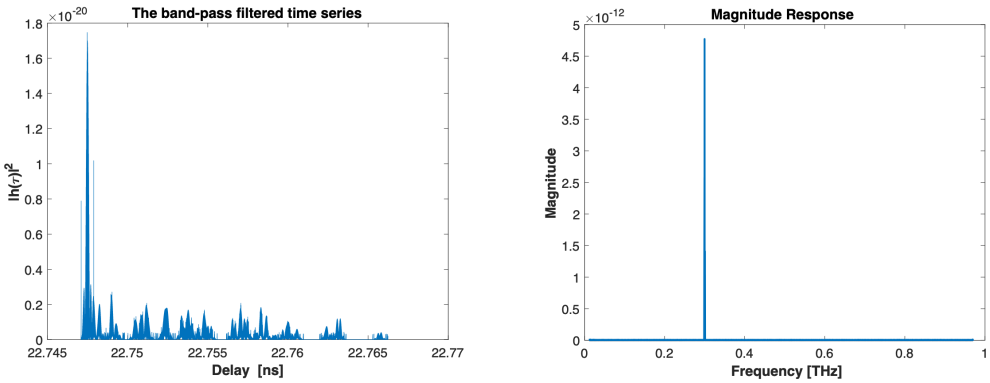

(a) (b)

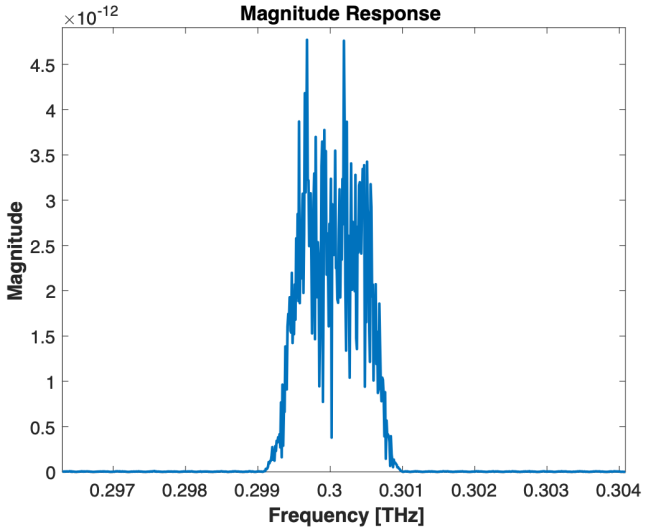

(c)

Figure 5.24. a) The convolution results between the bandpass filter and the input CIR in the time domain. b) The magnitude response in the frequency domain. As is expected, only the frequencies around 300 GHz are extracted by applying the filter. c) The magnitude response around the center frequency of 300 GHz is shown. Since the applied filter is not an ideal filter, the cut of frequencies are not 299.5 GHz and 300.5 GHz but 299 GHz and 301 GHz.

5.6 RMS Delay Spread and Coherence Bandwidth

The parameters that describe the multipath channel are the mean excess delay, rms delay spread, and excess delay spread that can be computed from the power delay profile. The time dispersion properties of wideband multipath channels are most commonly quantified by their mean excess delay $\bar{\tau}$, and rms delay spread o_i in the i^{th} sub-band. The mean excess delay is the first moment

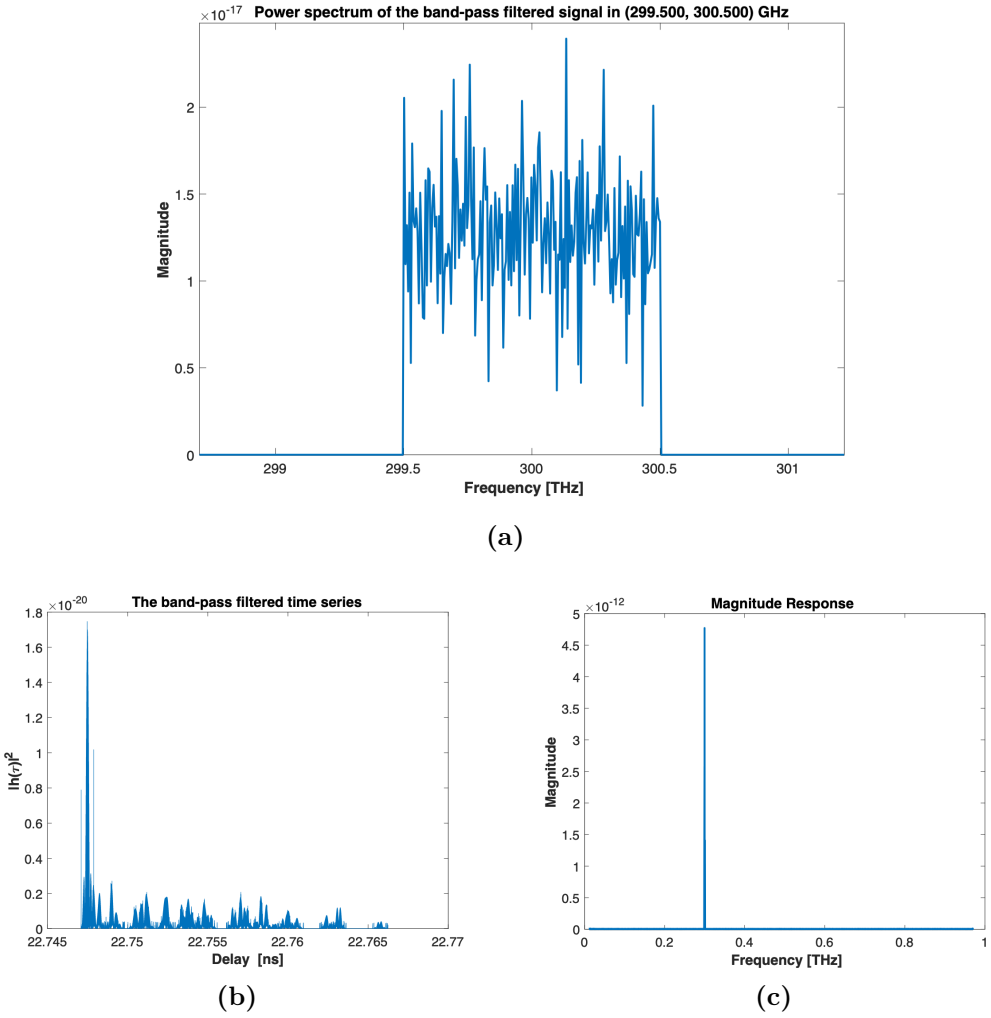

Figure 5.25. a) The magnitude response of an ideal bandpass filter around the center frequency of 300 GHz with the bandpass of 1 GHz. The cutoff frequencies are exactly 299.5 GHz and 300.5 GHz. The bandpass filtered time series, i.e., the convolution results between the ideal bandpass filter and the input CIR is shown in (b), and c) shows its magnitude response.

of the power delay profile and is defined as [49, 50, 51]:

$$\bar{\tau} = \frac{\sum_p a_{i,p}^2 \tau_p}{\sum_p a_{i,p}^2}. \tag{5.9}$$

The rms delay spread is the square root of the second moments of the instantaneous power delay profile and is:

$$o_i = \sqrt{\bar{\tau^2} - (\bar{\tau})^2}, \tag{5.10}$$

where

$$\bar{\tau^2} = \frac{\sum_p a_{i,p}^2 \tau_p^2}{\sum_p a_{i,p}^2}. \tag{5.11}$$

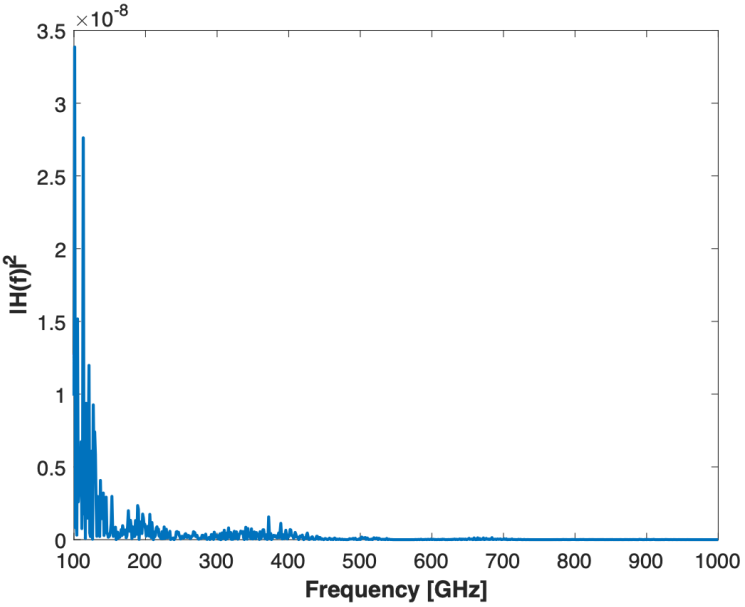

Figure 5.26. CTF of the channel computed by equation (3.22). The utilized parameters are: the room size of [X=8 m, Y=8 m, Z=8 m], Tx=[X=2 m, Y=3 m, Z=5 m], Rx=[X=4 m, Y=4 m, Z=6 m], $\sigma = 0.088\ mm$, $T_{corr} = 2.3\ mm$, humidity of $RH = 70\%$, n and α are taken from [2] for different frequencies and are the same for all faces.

where $a_{i,p}$ in the amplitude of the p^{th} path in the i^{th} sub-band as given in equation (3.14). Note that the maximum excess delay can be computed as $\tau_x - \tau_0$, where τ_0 and τ_x are the first signal arrival at Rx and the maximum excess delay, respectively. τ_x is the difference between the first and the last received multipath components. τ_x is also called excess delay spread of a power delay profile.
Considering only specular reflection of each face at the frequency of 300 GHz and the room size of [X=8 m, Y=8 m, Z=8 m], Tx=[X=2 m, Y=3 m, Z=5 m], Rx=[X=4 m, Y=4 m, Z=6 m], $\sigma = 0.088\ mm$, $T_{corr} = 2.3\ mm$, $n = 1.97$, $\alpha = 7.3\ cm^{-1}$, fixed for all faces, and humidity of $RH = 70\%$. Table 5.1 shows the simulation results of only specular reflection in which includes the delay and path gain. The rms delay spread is calculated as 6.16 ns for this

Table 5.1. The arrival of the specularly reflected rays at 300 GHz

Arrival path	Path gain [dB]	Delay [ns]
Specular reflection, face 1	−116.2457	22.7471
Specular reflection, face 2	−110.5426	10.0925
Specular reflection, face 3	−113.8627	16.3299
Specular reflection, face 4	−118.1072	29.2516
Specular reflection, face 5	−117.3717	25.5001
Specular reflection, face 6	−112.7164	12.3831

scenario. Note that through the Fourier transform, the power delay profile and

the magnitude of frequency response (the spectral response) of a mobile radio channel are related. Therefore one can obtain an equivalent description of the channel in the frequency domain using its frequency response characteristics. Coherence bandwidth is used, similar to the delay spread parameters in the time domain, to describe the channel in the frequency domain. Although their exact relationship is a function of the particular multipath structure, the rms delay spread and coherence bandwidth are inversely proportional to each other. Coherence bandwidth is a statistical measure of the range of frequencies over which the channel can be considered flat, i.e.; it is the range of frequencies over which two frequency components have a strong amplitude correlation. Suppose the coherence bandwidth is defined as the bandwidth over which

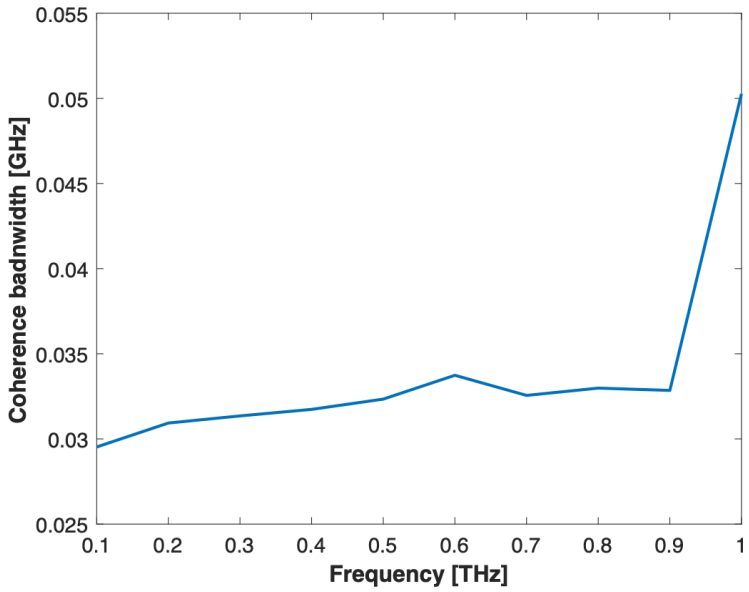

Figure 5.27. Coherence bandwidth as a function of frequency. Increasing frequency leads to a reduction in the multipath effect because of the high attenuation for the NLOS paths. Hence, a smaller rms delay spread is btained, i.e., larger coherence bandwidth.

the frequency correlation function is above 0.9. In that case, the coherence bandwidth is approximately $B_c = 1/50o_i$, or if the definition is relaxed so that the frequency correlation function is above 0.5, then the coherence bandwidth is approximately $B_c = 1/5o_i$ [51]. Hence, the coherence bandwidth, defined as the range of frequencies over which channel correlation exceeds 50%, is given by $1/5o_i = 32.462\ MHz$. Note that in the case of considering all the scattered incoming rays from all faces, the value of coherence bandwidth is the same, i.e., $0.2/o_i = 32.462\ MHz$. While the calculated rms delay spread considering only the scattered incoming rays from face 1 is about 4.986 ns, and hence the coherence bandwidth is 40.10 GHz. Note that increasing frequency would reduce in the multipath effect due to the very high loss for the NLoS paths. This results in a smaller rms delay spread and hence, larger coherence bandwidth, as shown in Fig. 5.27.

Chapter 6

Conclusion and future works

This thesis focused on developing a multi-ray channel model in the THz Band by using ray-tracing techniques. The entire work comprises the following parts: (1) we discussed wireless propagation characteristics and the LOS path loss in the THz Band. The results show that THz communication strongly depends on the molecular composition of the medium and the transmission distance. The main factor affecting the behavior of the THz Band is the absorption by water vapor molecules, which attenuates the transmitted signal (discussed in chapter 3). (2) A complete analysis of diffuse scattering from surfaces has been conducted. First, the definition of the roughness of a surface and its frequency dependence is discussed; subsequently, some theories, especially Kirchhoff's theory, are explained in state of art, including articles and studies already presented in the literature. Starting from this knowledge, we tried to find out how the surface roughness influences the overall received power. A ray-tracing simulator has been developed to analyze the scattering phenomenon and do accurate simulations of real handmade structures, i.e., different kinds of rough surfaces. We also proposed an RT-based method that computes the scattering field in Rx direction from the random rough surfaces (RRS) by considering only the specular reflection coefficient using Fresnel theory (discussed in chapter 5). Hence, we focused on realizing and generating RRS and how to use them in the simulator to get the required results (see chapter 3). Simulation results showed that in the case of rough surfaces, one faces diffuse scattering rather than specular reflection. Its dependence on the surface statistical parameter (standard deviation of height and correlation length) has also been observed as a function of frequency, showing a good agreement from what is expected. It is also shown that in the case of indoor propagation, the frequency dependence is strictly related to the room's internal geometry and the position of Tx and Rx. Moreover, the study of the received power led to the conclusion that not only the molecular composition of the medium and the transmission distance but also surface roughness affects the power loss at THz band proportionally to the degree of roughness. Results show how roughness affects the diffuse scattering and its different behavior as a function of frequency. (3) We analyzed the existing diffuse scattering models and realized that the method used to generate

scattering tiles on building surfaces directly influenced the number and energy of scattering components involved in the final calculation. Scattering tiles were generated on each surface and parameters such as the PDP, angles of incidence, reflection, and deviation of diffuse scattering components were analyzed as the metrics for the performance assessments.
(4) we proposed a multi-ray channel that incorporates the propagation models for the LOS, reflected, and scattered paths for the THz band. Based on the developed propagation model, we presented an analysis of the THz Band channel characteristics. It is shown that the spectral windows defined by the molecular absorption loss are distance-varying. Moreover, as the distance increases, the width of these spectral windows reduces. We also show that the rms delay spread is dependent on the distances and frequencies, and consequently, for longer distances and lower frequencies, the coherence bandwidth decreases. Regarding this work, the proposed multi-ray channel model can be used as a foundation to design an efficient communication system in THz frequencies. Our results will permit us to better focus the efforts for future works such as Tx and Rx's efficient positioning. This work can also improve to investigate a new MIMO system model for THz communications that include the effects of rough reflection surfaces.

Appendix A

Ray tracer functions

In this thesis, the proposed ray-tracer is implemented in MATLAB. The code includes several functions that are tried to describe in this section. The main tasks of the ray tracer are:

- Compute the environmental condition such as Tx and Rx's position, room size, and the reflection coefficient of surfaces. Figure A.1a and A.1b show the environmental condition for two different settings where the tiles and the paths related to the specular reflection from each face is drawn. Note that it is possible to add extra faces inside the room, but an empty room has been considered here in our assumption.

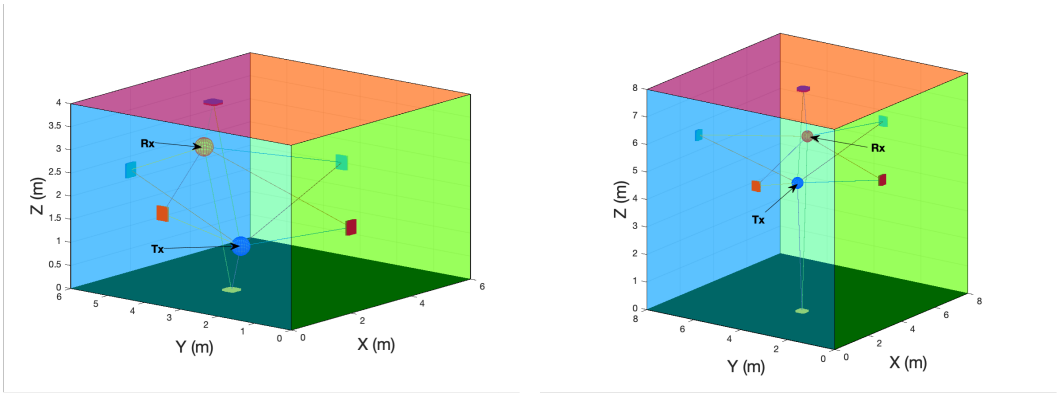

(a) **(b)**

Figure A.1. The RT find specular reflection and the tiles for two different room sizes and two different TX and Rx positions. a) Room size is [X=6 Y=6 Z=4] with the Tx=[X=2 Y=3 Z=1] and Rx=[X=2 Y=4 Z=3] position. b) Room size is [X=8 Y=8 Z=8] with the Tx=[X=2 Y=3 Z=5] and Rx=[X=4 Y=4 Z=6] position.

- Find specular reflection points for all the room faces and then scatter points around each one and their paths from Tx to Rx (small squares around specular points in Fig. A.1a and A.1b are related to the scatter points).

- Compute total attenuation caused by molecular absorption, free-space propagation, scattering (based on Kirchhoff theory).
- Compute geometrical parameters such as the angle of incidence, angle of reflection, deviation angle, delay with respect to firstly, LOS time, and secondly with respect to the shorts traveling time among all of the incoming rays and so forth.
- Compute Phase shift related to each point on each wall.
- Plot the results.

A.1 Ray tracer functions descriptions

The proposed ray tracer's main goal is to determine the possible rays propagating between Tx and Rx, including LOS and NLOS propagation in a 3D space. Therefore, it is necessary to evaluate all the possible angles of launching rays from Tx and the angles of arriving rays at Rx.
The proposed ray tracer has been divided into several functions. The main contribution of the proposed ray tracer functions is explained as follows:

A.1.1 Main.m

This is the main function of the code. This function calls all the other necessary functions for this project. The constants such as the size of the room, [X Y Z], speed of light, frequency, the position of Tx and Rx, correlation length of the surface *Tcorr*, and the like are defined. Note that the room is considered empty. The input parameters that need to be defined are listed in the table A.1.

Table A.1. List of variables

Variable name	Description
c = 3×10^8	Speed of light
frequency = 300 GHz	considered frequency
X=Y=Z= 8	size of the room =[X Y Z] (m)
pos_emitter = [2 3 5]	Tx position (m)
pos_receptor = [4 4 6]	Rx position (m)
Tcorr = 2.3 mm	correlation length
sigma = 0.088 mm	standard deviation of the height of the surface
sizeOfScatPtMatrix = 5	number of tiles around each specular point
pol = '-' or '+'	define horizontal or vertical polarization, respectively
n	refractive index of the surface
eps	permittivity of the surface
mu	permeability of the surface

A.1.2 point_Reflection.m

Regarding the given size of the room and the given position of the transmitter (Tx) and receiver (Rx), this function finds the specular point's position on each face. The way of calling this function is *[pt1, pt2, pt3, pt4, pt5, pt6] = point_Reflection(room, pos_emitter, pos_receptor);* where pt1 to pt6 are the coordinates of the specular points on each face. To find these points, other functions such as *compute_points.m*, *EqPlan3Pts_Vector.m*, *EqPlan3Pts.m*, *PlanLineIntersect.m*, and *EIntersectPlanes.m* need to call in order to firstly find the corner points of the room and then the mathematical plane equation of all the faces of the room.

A.1.3 compute_points.m

This function aims to find 8 different corner points of the room and find the relative plane functions (or coefficient [a b c d]) of each plane. Note that the room is built based on the multiplication of each vector of a unit cube to the room's size given as an input.
This function is defined as *[cube_points, cube_faceVect, eqFaces] = compute_points([0 0 0], room(1), room(2), room(3))* where [0 0 0] is the first point. *cube_faceVect* and *cube_faceEq* are outputs of the *EqPlan3Pts_Vector.m* and *EqPlan3Pts.m* functions.

A.1.4 EqPlan3Pts_Vector.m

This function finds the plane equation coefficient based on three points. It can be called as *M = EqPlan3Pts_Vector(A, B, C)* where A, B, and C are the coordinates of three points. The output is M = [a b c t] that are the coefficients of the plane equation passing through three points given as input, ax + by + cz + t = 0.

A.1.5 EqPlan3Pts.m

This function return the plane equation as a symbolic function based on three given points (ax + by + cz + t = 0). It can be called as *planefunction = EqPlan3Pts(p0, p1, p2)* where *p0, p1, p2* are the coordinates of three points.

A.1.6 PlanLineIntersect.m

It can be defined as *[eqLine, pt]= PlanLineIntersect(p1, p2, eqPlan)* where p1 and p2 are two given points and *eqPlan* is the equation of a plan. This function returns the equation of the line passing from two points *eqLine*, and the point of intersection *pt*, between the line and the given surface.

A.1.7 EIntersectPlanes.m

This function is useful to exclude the fact that the reflection point cannot be in an intersection of faces. It can be defined as *bool = EIntersectPlanes(plan1, plan2, point)* where take 2 planes and one point as input and return 1 if the point is in the intersection of the two plans.

A.1.8 scatter_points.m

The goal of this function is to return the center position of all the tiles around each specular point, which are located at the distance of multiplications of correlation distance, Tcorr, from the specular point. This function is called as *scatPtx = scatter_points(ptx, room, lx, sizeOfScatPtMatrix)*. The number of tiles has been given as an input *sizeOfScatPtMatrix*. ptx is the specular point of face x. Note that tiles are assumed to be square, and this function takes *lx* as the side length of a tile as an input. The output of this function is a matrix of scatter points (*scatPtx*) around the specular point of the face x. Two main function such as *compute_points.m* and *PinPlan.m* has been called inside this function.

A.1.9 PinPlan.m

This function checks if the input of the *scatter_points.m* function is related to which wall and has the form of *bool = PinPlan(planeq, P)* where *planeq* is the equation of the plan and P is the point. It returns 1 if P is in the plan; otherwise, return 0.

A.1.10 scatter_angles.m

Three different angles of incident, reflection and deviation related to each of the scatter points including specular ones has been computed through this function. This function has the form of *[theta1_R11, theta2_R11, theta31] = scatter_angles(pt1, pos_emitter, pos_receptor, room, lx, sizeOfScatPtMatrix)*. The output of this function is *theta1_R1x* that is a column matrix containing the incident angle between the ray coming from transmitter and face X, *theta2_R1x* is a column matrix containing the reflecting angle between the ray reflecting from the relevant scatter point on face X and Rx and *theta3x* is a column matrix of deviation angles from specular reflection of each tile.

A.1.11 Func_of_ppinf.m

This function aims to implement the value of mean scattered power for the infinite conductive surface of each wall for each point based on Kirchhoff theory. It returns the values in dB and the value of g, which is the surface's roughness factor. The function has the form of *[ppinf1, ppinfdb1, g1]=Func_of_ppinf(Tcorr, theta1_R11, theta2_R11, theta31, lx, ly, sigma, lambda)*. This function return $< \rho\rho* >_\infty$ named as *'ppinfx', 'ppinfdbx'* for infinite conductive surface where

x refers to face X for each tile as linear or dB besides the value of g for each tile of different faces.

A.1.12 Func_of_ppfinite.m

The function returns the value of mean scattered power for the finite conductive surface of each wall for each point based on Kirchhoff theory. This function calls *Func_of_ppinf.m* and *FresnelCoeff.m* to do the required calculations. It has the form of *[ppfinite, ppfinitedb, g, ppinf, R, RRconjug]=Func_of_ppfinite(Tcorr, theta1, theta2, theta3, lx, ly, sigma, lambda, mu, eps, pol, n)* where the outputs of the function are mean scattering coefficient for the finite conductive surface in linear and dB *ppfinite* and *ppfinitedb*, the roughness parameter g, mean scattering coefficient for infinite conductive surface ppinf, and Fresnel reflection coefficient R and its conjugate RRconjug.

A.1.13 FresnelCoeff.m

It has the form of *[R, RRconj]= FresnelCoeff(theta1, mu, alpha, lambda, eps, pol, n)* where it is able to find the Fresnel reflection coefficient for both vertical and horizontal polarization.

A.1.14 PowerRx.m

It has the form of *[power, powerdb] = PowerRx (theta1, A, pos_receptor, scatPt, lambda, ppfinite)* and calculate the mean power reflection coefficient of a surface area A at the receiver position. The outputs of this function are *power_rec_db* and *power_rec_db* that is the same as *power_rec* converted in dB.

A.1.15 Path_Loss.m

This function computes the propagation path loss that is the sum of free space and molecular absorption path loss in dB related to each path. It has the form of *[Ploss, PLoss_dB, Ploss_LOS] = Path_Loss(scatPt, pos_receptor, pos_emitter, k, lambda)* where k(f) is Molecular absorption coefficient at the given frequency. *Ploss* and *PLoss_dB* are path loss regarding the NLOS path in linear and dB, respectively and *Ploss_LOS* is path loss of LOS path. Note that total attenuation by considering the contribution of the scattering attenuation is saved in *totalAttenuation* variable.

A.1.16 Delay.m

This function returns a matrix of the delay related to all the points, including the specular and the scatter points of each face of the room. It has the form of *[Delay_vec]= delay (pos_emitter, pos_receptor, room, lx, sizeOfScatPtMatrix, boolNLOS, c)* where the delay is computed with respect to 1) the shortest time among the different propagation time of the 6 rays suffering a specular

reflection and 2) with respect to the time of LOS time. If *boolNLOS* is equal to one, the delay is computed with respect to the shortest time among the different; otherwise, it returns the delay matrix with respect to the LOS path. The output of this function is a matrix of delays *Delay_vec*, related to all the paths.

A.1.17 Distance.m

It has the form of *[DistVector] = Distance(PointVector, pt)* where this function finds the distance *DistVector*, between the points of an input vector, *PointVector*, and a destination point *pt* for each point separately.

Bibliography

[1] J.-J. Wu, "Simulation of rough surfaces with fft," *Tribology International*, vol. 33, no. 1, pp. 47–58, 2000.

[2] R. Piesiewicz, C. Jansen, D. Mittleman, T. Kleine-Ostmann, M. Koch, and T. Kurner, "Scattering analysis for the modeling of thz communication systems," *IEEE Transactions on Antennas and Propagation*, vol. 55, no. 11, pp. 3002–3009, 2007.

[3] C. Han, A. O. Bicen, and I. F. Akyildiz, "Multi-ray channel modeling and wideband characterization for wireless communications in the terahertz band," *IEEE Transactions on Wireless Communications*, vol. 14, no. 5, pp. 2402–2412, 2014.

[4] C. Jansen, S. Priebe, C. Moller, M. Jacob, H. Dierke, M. Koch, and T. Kurner, "Diffuse scattering from rough surfaces in thz communication channels," *IEEE Transactions on Terahertz Science and Technology*, vol. 1, no. 2, pp. 462–472, 2011.

[5] H.-J. Song and T. Nagatsuma, "Present and future of terahertz communications," *IEEE transactions on terahertz science and technology*, vol. 1, no. 1, pp. 256–263, 2011.

[6] T. S. Rappaport, R. W. Heath Jr, R. C. Daniels, and J. N. Murdock, *Millimeter wave wireless communications*. Pearson Education, 2014.

[7] J. M. Jornet and I. F. Akyildiz, "Channel modeling and capacity analysis for electromagnetic wireless nanonetworks in the terahertz band," *IEEE Transactions on Wireless Communications*, vol. 10, no. 10, pp. 3211–3221, 2011.

[8] Y. Wang, F. Zhang, Z. Dong, and H. Sun, "Effects of nonsphericity on attenuation characteristics of thz atmospheric propagation," in *2016 41st International Conference on Infrared, Millimeter, and Terahertz waves (IRMMW-THz)*, pp. 1–2, IEEE, 2016.

[9] F. Sheikh, D. Lessy, M. Alissa, and T. Kaiser, "A comparison study of non-specular diffuse scattering models at terahertz frequencies," in *2018 First International Workshop on Mobile Terahertz Systems (IWMTS)*, pp. 1–6, IEEE, 2018.

[10] V. Degli-Esposti, D. Guiducci, A. de'Marsi, P. Azzi, and F. Fuschini, "An advanced field prediction model including diffuse scattering," *IEEE Transactions on Antennas and Propagation*, vol. 52, no. 7, pp. 1717–1728, 2004.

[11] T. Schneider, A. Wiatrek, S. Preußler, M. Grigat, and R.-P. Braun, "Link budget analysis for terahertz fixed wireless links," *IEEE Transactions on Terahertz Science and Technology*, vol. 2, no. 2, pp. 250–256, 2012.

[12] K. Yang, A. Pellegrini, M. O. Munoz, A. Brizzi, A. Alomainy, and Y. Hao, "Numerical analysis and characterization of thz propagation channel for body-centric nano-communications," *IEEE Transactions on Terahertz Science and technology*, vol. 5, no. 3, pp. 419–426, 2015.

[13] Z. Xu, X. Dong, and J. Bornemann, "A statistical model for the mimo channel with rough reflection surfaces in the thz band," *Nano Communication Networks*, vol. 8, pp. 25–34, 2016.

[14] M. J. Fitch and R. Osiander, "Terahertz waves for communications and sensing," *Johns Hopkins APL technical digest*, vol. 25, no. 4, pp. 348–355, 2004.

[15] I. F. Akyildiz, J. M. Jornet, and C. Han, "Teranets: Ultra-broadband communication networks in the terahertz band," *IEEE Wireless Communications*, vol. 21, no. 4, pp. 130–135, 2014.

[16] H. T. Friis, "A note on a simple transmission formula," *Proceedings of the IRE*, vol. 34, no. 5, pp. 254–256, 1946.

[17] R. V. Kochanov, I. Gordon, L. Rothman, P. Wcisło, C. Hill, and J. Wilzewski, "Hitran application programming interface (hapi): A comprehensive approach to working with spectroscopic data," *Journal of Quantitative Spectroscopy and Radiative Transfer*, vol. 177, pp. 15–30, 2016.

[18] L. S. Rothman, I. E. Gordon, Y. Babikov, A. Barbe, D. C. Benner, P. F. Bernath, M. Birk, L. Bizzocchi, V. Boudon, L. R. Brown, *et al.*, "The hitran2012 molecular spectroscopic database," *Journal of Quantitative Spectroscopy and Radiative Transfer*, vol. 130, pp. 4–50, 2013.

[19] I. E. Gordon, L. S. Rothman, C. Hill, R. V. Kochanov, Y. Tan, P. F. Bernath, M. Birk, V. Boudon, A. Campargue, K. Chance, *et al.*, "The hitran2016 molecular spectroscopic database," *Journal of Quantitative Spectroscopy and Radiative Transfer*, vol. 203, pp. 3–69, 2017.

[20] S. Paine, "The am atmospheric model," sep 2019.

[21] N. V. TKACHENKO, "Chapter 1 - introduction," in *Optical Spectroscopy* (N. V. TKACHENKO, ed.), pp. 1 – 14, Amsterdam: Elsevier Science, 2006.

[22] P. Beckmann and A. Spizzichino, "The scattering of electromagnetic waves from rough surfaces," *Norwood, MA, Artech House, Inc., 1987, 511 p.*, 1987.

[23] A. Spizzichino, *The Scattering of Electromagnetic Waves from Rough Surfaces. By P. Beckmann... and André Spizzichino.* Pergamon Press, 1963.

[24] S. O. Rice, "Reflection of electromagnetic waves from slightly rough surfaces," *Communications on pure and applied mathematics*, vol. 4, no. 2-3, pp. 351–378, 1951.

[25] L. Tsang, J. A. Kong, and K.-H. Ding, *Scattering of electromagnetic waves: theories and applications*, vol. 27. John Wiley & Sons, 2004.

[26] E. I. Thorsos and D. R. Jackson, "The validity of the perturbation approximation for rough surface scattering using a gaussian roughness spectrum," *The journal of the acoustical society of America*, vol. 86, no. 1, pp. 261–277, 1989.

[27] R. Piesiewicz, T. Kleine-Ostmann, N. Krumbholz, D. Mittleman, M. Koch, and T. Kürner, "Terahertz characterisation of building materials," *Electronics Letters*, vol. 41, no. 18, pp. 1002–1004, 2005.

[28] J. A. Stratton, *Electromagnetic theory.* John Wiley & Sons, 2007.

[29] C. L. Vernold and J. E. Harvey, "Modified beckmann-kirchoff scattering theory for nonparaxial angles," in *Scattering and Surface Roughness II*, vol. 3426, pp. 51–56, International Society for Optics and Photonics, 1998.

[30] M. Nieto-Vesperinas and N. Garcia, "A detailed study of the scattering of scalar waves from random rough surfaces," *Optica Acta: International Journal of Optics*, vol. 28, no. 12, pp. 1651–1672, 1981.

[31] H. Ragheb and E. R. Hancock, "The modified beckmann–kirchhoff scattering theory for rough surface analysis," *Pattern Recognition*, vol. 40, no. 7, pp. 2004–2020, 2007.

[32] O. Franek, J. B. Andersen, and G. F. Pedersen, "Diffuse scattering model of indoor wideband propagation," *IEEE Transactions on Antennas and Propagation*, vol. 59, no. 8, pp. 3006–3012, 2011.

[33] D. Newland, *Random vibration and spectral analysis.* Longman, 1984.

[34] Y. Hu and K. Tonder, "Simulation of 3-d random rough surface by 2-d digital filter and fourier analysis," *International journal of machine tools and manufacture*, vol. 32, no. 1-2, pp. 83–90, 1992.

[35] A. F. Molisch, "Ultrawideband propagation channels-theory, measurement, and modeling," *IEEE transactions on vehicular technology*, vol. 54, no. 5, pp. 1528–1545, 2005.

[36] H. Sugahara, Y. Watanabe, T. Ono, K. Okanoue, and S. Yarnazaki, "Development and experimental evaluations of "rs-2000" - a propagation simulator for uwb systems," in *2004 International Workshop on Ultra Wideband Systems Joint with Conference on Ultra Wideband Systems and Technologies. Joint UWBST IWUWBS 2004 (IEEE Cat. No.04EX812)*, pp. 76–80, 2004.

[37] D. Tse and P. Viswanath, *Fundamentals of wireless communication*. Cambridge university press, 2005.

[38] K. Tsujimura, K. Umebayashi, J. Kokkoniemi, J. Lehtomäki, and Y. Suzuki, "A causal channel model for the terahertz band," *IEEE Transactions on Terahertz Science and Technology*, vol. 8, pp. 52–62, Jan 2018.

[39] S. S. Sidhu, A. Khosla, and A. Sharma, "Implementation of 3-d ray tracing propagation model for indoor wireless communication," *International Journal of Electronics Engineering*, vol. 4, no. 1, pp. 43–47, 2012.

[40] F. Sheikh, D. Lessy, and T. Kaiser, "A novel ray-tracing algorithm for non-specular diffuse scattered rays at terahertz frequencies," in *2018 First International Workshop on Mobile Terahertz Systems (IWMTS)*, pp. 1–6, IEEE, 2018.

[41] F. Sheikh, M. El-Hadidy, and T. Kaiser, "Terahertz band: Indoor ray-tracing channel model considering atmospheric attenuation," in *Antennas and Propagation & USNC/URSI National Radio Science Meeting, 2015 IEEE International Symposium on*, pp. 1782–1783, IEEE, 2015.

[42] A. Torabi, S. A. Zekavat, and A. Al-Rasheed, "Millimeter wave directional channel modeling," in *2015 IEEE International Conference on Wireless for Space and Extreme Environments (WiSEE)*, pp. 1–6, IEEE, 2015.

[43] M. Born and E. Wolf, *Principles of optics: electromagnetic theory of propagation, interference and diffraction of light*. Elsevier, 2013.

[44] W. Tam and V. Tran, "Propagation modelling for indoor wireless communication," *Electronics & Communication Engineering Journal*, vol. 7, no. 5, pp. 221–228, 1995.

[45] S. Priebe, M. Jacob, C. Jansen, and T. Kürner, "Non-specular scattering modeling for thz propagation simulations," in *Proceedings of the 5th European Conference on Antennas and Propagation (EUCAP)*, pp. 1–5, IEEE, 2011.

[46] D. Didascalou, M. Dottling, N. Geng, and W. Wiesbeck, "An approach to include stochastic rough surface scattering into deterministic ray-optical wave propagation modeling," *IEEE Transactions on Antennas and Propagation*, vol. 51, no. 7, pp. 1508–1515, 2003.

[47] Y. Cocheril and R. Vauzelle, "A new ray-tracing based wave propagation model including rough surfaces scattering," *Progress In Electromagnetics Research*, vol. 75, pp. 357–381, 2007.

[48] K. O'Donnell and E. Mendez, "Experimental study of scattering from characterized random surfaces," *JOSA A*, vol. 4, no. 7, pp. 1194–1205, 1987.

[49] A. Goldsmith, *Wireless communications*. Cambridge university press, 2005.

[50] B. Sklar *et al.*, *Digital communications: fundamentals and applications*. 2001.

[51] T. S. Rappaport *et al.*, *Wireless communications: principles and practice*, vol. 2. prentice hall PTR New Jersey, 1996.